**Université de Montréal**

# Development of Imaging Mass Spectrometry Analysis of Lipids in Biological and Clinically Relevant Applications

**Par**

**Nathan Heath Patterson**

**Département de Chimie**

**Faculté des Arts et des Sciences**

**Thèse présentée à la Faculté des études supérieures et postdoctorales en vue de l'obtention du grade de *philosophiae doctor* (Ph.D.) en chimie**

**Avril 2016**

## Resumé

La spectrométrie de masse mesure la masse des ions selon leur rapport masse sur charge. Cette technique est employée dans plusieurs domaines et peut analyser des mélanges complexes. L'imagerie par spectrométrie de masse (Imaging Mass Spectrometry en anglais, IMS), une branche de la spectrométrie de masse, permet l'analyse des ions sur une surface, tout en conservant l'organisation spatiale des ions détectés. Jusqu'à présent, les échantillons les plus étudiés en IMS sont des sections tissulaires végétales ou animales. Parmi les molécules couramment analysées par l'IMS, les lipides ont suscité beaucoup d'intérêt. Les lipides sont impliqués dans les maladies et le fonctionnement normal des cellules; ils forment la membrane cellulaire et ont plusieurs rôles, comme celui de réguler des événements cellulaires. Considérant l'implication des lipides dans la biologie et la capacité du MALDI IMS à les analyser, nous avons développé des stratégies analytiques pour la manipulation des échantillons et l'analyse de larges ensembles de données lipidiques.

La dégradation des lipides est très importante dans l'industrie alimentaire. De la même façon, les lipides des sections tissulaires risquent de se dégrader. Leurs produits de dégradation peuvent donc introduire des artefacts dans l'analyse IMS ainsi que la perte d'espèces lipidiques pouvant nuire à la précision des mesures d'abondance. Puisque les lipides oxydés sont aussi des médiateurs importants dans le développement de plusieurs maladies, leur réelle préservation devient donc critique. Dans les études multi-institutionnelles où les échantillons sont souvent transportés d'un emplacement à l'autre, des protocoles adaptés et validés, et des mesures de dégradation sont nécessaires. Nos principaux résultats sont les suivants : un accroissement en fonction du temps des phospholipides oxydés et des lysophospholipides dans des conditions ambiantes, une diminution de la présence des lipides ayant des acides gras insaturés et un effet inhibitoire sur ses phénomènes de la conservation des sections au froid sous $N_2$. A température et atmosphère ambiantes, les phospholipides sont oxydés sur une échelle de temps typique d'une préparation IMS normale (~30 minutes). Les phospholipides sont aussi décomposés en lysophospholipides sur une échelle de temps de plusieurs jours. La validation d'une méthode de manipulation d'échantillon est d'autant plus importante lorsqu'il s'agit d'analyser un plus grand nombre d'échantillons.

L'athérosclérose est une maladie cardiovasculaire induite par l'accumulation de matériel cellulaire sur la paroi artérielle. Puisque l'athérosclérose est un phénomène en trois dimension (3D), l'IMS 3D en série devient donc utile, d'une part, car elle a la capacité à localiser les molécules sur la longueur totale d'une plaque athéromateuse et, d'autre part, car elle peut identifier des mécanismes moléculaires du développement ou de la rupture des plaques. l'IMS 3D en série fait face à certains défis spécifiques, dont beaucoup se rapportent simplement à la reconstruction en 3D et à l'interprétation de la reconstruction moléculaire en temps réel. En tenant compte de ces objectifs et

en utilisant l'IMS des lipides pour l'étude des plaques d'athérosclérose d'une carotide humaine et d'un modèle murin d'athérosclérose, nous avons élaboré des méthodes «*open-source*» pour la reconstruction des données de l'IMS en 3D. Notre méthodologie fournit un moyen d'obtenir des visualisations de haute qualité et démontre une stratégie pour l'interprétation rapide des données de l'IMS 3D par la segmentation multivariée. L'analyse d'aortes d'un modèle murin a été le point de départ pour le développement des méthodes car ce sont des échantillons mieux contrôlés. En corrélant les données acquises en mode d'ionisation positive et négative, l'IMS en 3D a permis de démontrer une accumulation des phospholipides dans les sinus aortiques. De plus, l'IMS par AgLDI a mis en évidence une localisation différentielle des acides gras libres, du cholestérol, des esters du cholestérol et des triglycérides. La segmentation multivariée des signaux lipidiques suite à l'analyse par IMS d'une carotide humaine démontre une histologie moléculaire corrélée avec le degré de sténose de l'artère. Ces recherches aident à mieux comprendre la complexité biologique de l'athérosclérose et peuvent possiblement prédire le développement de certains cas cliniques.

La métastase au foie du cancer colorectal (Colorectal cancer liver metastasis en anglais, CRCLM) est la maladie métastatique du cancer colorectal primaire, un des cancers le plus fréquent au monde. L'évaluation et le pronostic des tumeurs CRCLM sont effectués avec l'histopathologie avec une marge d'erreur. Nous avons utilisé l'IMS des lipides pour identifier les compartiments histologiques du CRCLM et extraire leurs signatures lipidiques. En exploitant ces signatures moléculaires, nous avons pu déterminer un score histopathologique quantitatif et objectif et qui corrèle avec le pronostic. De plus, par la dissection des signatures lipidiques, nous avons identifié des espèces lipidiques individuelles qui sont discriminants des différentes histologies du CRCLM et qui peuvent potentiellement être utilisées comme des biomarqueurs pour la détermination de la réponse à la thérapie. Plus spécifiquement, nous avons trouvé une série de plasmalogènes et sphingolipides qui permettent de distinguer deux différents types de nécrose (infarct-like necrosis et usual necrosis en anglais, ILN et UN, respectivement). L'ILN est associé avec la réponse aux traitements chimiothérapiques, alors que l'UN est associé au fonctionnement normal de la tumeur.

**Mots clés :** imagerie par spectrométrie de masse, lipides, imagerie 3D, artériosclérose, cancer du colon, métastase, foie.

## Summary

Mass spectrometry is the measurement of the mass over charge ratio of ions. It is broadly applicable and capable of analyzing complex mixtures. Imaging mass spectrometry (IMS) is a branch of mass spectrometry that analyses ions across a surface while conserving their spatial organization on said surface. At this juncture, the most studied IMS samples are thin tissue sections from plants and animals. Among the molecules routinely imaged by IMS, lipids have generated significant interest. Lipids are important in disease and normal cell function as they form cell membranes and act as signaling molecules for cellular events among many other roles. Considering the potential of lipids in biological and clinical applications and the capability of MALDI to ionize lipids, we developed analytical strategies for the handling of samples and analysis of large lipid MALDI IMS datasets.

Lipid degradation is massively important in the food industry with oxidized products producing a bad smell and taste. Similarly, lipids in thin tissue sections cut from whole tissues are subject to degradation, and their degradation products can introduce IMS artifacts and the loss of normally occurring species to degradation can skew accuracy in IMS measures of abundance. Oxidized lipids are also known to be important mediators in the progression of several diseases and their accurate preservation is critical. As IMS studies become multi-institutional and collaborations lead to sample exchange, the need for validated protocols and measures of degradation are necessary. We observed the products of lipid degradation in tissue sections from multiple mouse organs and reported on the conditions promoting and inhibiting their presence as well as the timeline of degradation. Our key findings were the increase in oxidized phospholipids and lysophospholipids from degradation at ambient conditions, the decrease in the presence of lipids containing unsaturations on their fatty acyl chains, and the inhibition of degradation by matrix coating and cold storage of sections under $N_2$ atmosphere. At ambient atmospheric and temperature, lipids degraded into oxidized phospholipids on the time-scale of a normal IMS experiment sample preparation (within 30 min). Lipids then degraded into lysophospholipids' on a time scale on the order of several days. Validation of sample handling is especially important when a greater number of samples are to be analyzed either through a cohort of samples, or analysis of multiple sections from a single tissue as in serial 3D IMS.

Atherosclerosis is disease caused by accumulation of cellular material at the arterial wall. The accumulation implanted in the cell wall grows and eventually occludes the blood vessel, or causes a stroke. Atherosclerosis is a 3D phenomenon and serial 3D IMS is useful for its ability to localize molecules throughout the length of a plaque and help to define the molecular mechanisms of plaque development and rupture. Serial 3D IMS has many challenges, many of which are simply a matter of producing 3D reconstructions and interpreting them in a timely fashion. In this aim and using

analysis of lipids from atherosclerotic plaques from a human carotid and mouse aortic sinuses, we described 3D reconstruction methods using open-source software for reconstruction, visualization and data analysis. Our methodology provides means to obtain high quality visualizations and demonstrates strategies for rapid interpretation of 3D IMS datasets through multivariate segmentation. Mouse aorta from model animals provided a springboard for developing the methods on lower risk samples with less variation with interesting molecular results. 3D MALDI IMS showed localized phospholipid accumulation in the mouse aortic sinuses with correlation between separate positive and negative ionization datasets. Silver-assisted LDI imaging presented differential localization of free fatty acids, cholesterol / cholesterol esters, and triglycerides. The human carotid's 3D segmentation shows molecular histologies (spatial groupings of imaging pixels with similar spectral fingerprints) correlating to the degree of arterial stenosis. Our results outline the potential for 3D IMS in atherosclerotic research. Molecular histologies and their 3D spatial organization, obtained from the IMS techniques used herein, may predict high-risk features, and particularly identify areas of plaque that have higher-risk of rupture. These investigations would help further unravel the biological complexities of atherosclerosis, and predict clinical outcomes.

Colorectal cancer liver metastasis (CRCLM) is the metastatic disease of primary colorectal cancer, one of the most common cancers worldwide. CRC is a cancer of the endothelial lining of the colon or rectum. Prognosticating and assessment of CRC tumors is performed using classical histopathology with a margin of error due to the subjective nature of histopathology. We have used lipid IMS to identify the histological compartments and extract their signature and using these IMS signatures we obtained a quantitative and objective histopathological score that correlates with prognosis. Additionally, by dissecting out the lipid signatures we have identified single lipid moieties that are unique to different histologies that could potentially be used as new biomarkers for assessing response to therapy. Particularly, we found a series of plasmalogen and sphingolipid species that differentiate infarct-like and usual necrosis, typical of chemotherapeutic response and normal tumor function, respectively.

**Keywords:** Imaging mass spectrometry, lipids, 3D imaging, atherosclerosis, colorectal cancer liver metastasis, metastasis, liver

# Table of Contents

# List of tables

# List of figures

## List of abbreviations

| | |
|---|---|
| 2D | Two dimensional |
| 3D | Three dimensional |
| AB | Alcian blue |
| AgLDI | Silver-assisted LDI |
| ApoE | Apolipoprotein E |
| ApoF | Apolipoprotein F |
| auROC | Area under receiver operator characteristic curve |
| CE | Cholesteryl ester |
| Cer | Ceramide |
| CRC | Colorectal cancer |
| CRCLM | Colorectal cancer liver metastasis |
| CVD | Cardiovascular disease |
| Da | Dalton |
| DAN | 1,5-diaminonapthalene |
| DESI | Desorption electrospray ionization |
| DFS | Disease free survival |
| DHA | Docosahexaenoic acid |
| EGFR | Epidermal growth factor receptor |
| FA | Fatty acyls |
| FFA | Free fatty acid |
| FT-ICR | Fourier transform ion cyclotron resonance |
| GL | Glycerolipids |
| GP | Glycerophospholipids |
| H&E | Hematoxylin and eosin |
| Hz | Hertz |
| ILN | Infarct-like necrosis |
| IMS | Imaging mass spectrometry |

| | |
|---|---|
| ISH | In-situ hybridization |
| ITO | Indium tin oxide |
| KRAS | Kirsten rat sarcoma viral oncogene homolog |
| LDL | Low density lipoprotein |
| Li | Lithium |
| LPC | Lysophosphotidylcholine |
| LPL | Lysophospholipids |
| m/z | Mass-to-charge ratio |
| MALDI | Matrix assisted laser desorption/ionization |
| MRI | Magnetic resonance imaging |
| MS | Mass spectrometry |
| MS/MS | Tandem mass spectrometry |
| mTRG | Modified tumor regression grade |
| NaCl | Sodium chloride |
| NEG | Negative ionization mode |
| NL | Neutral loss |
| OCT | Optimal cutting temperature |
| ORO | OilRedO |
| OS | Overall survival |
| OxPC | Oxidized phosphatidylcholine |
| OxPL | Oxidized phospholipid |
| PA | Phosphatidic acid |
| PBS | Phosphate buffered saline |
| PC | Phosphatidylcholine |
| PCA | Principal components analysis |
| PE | Phosphoethanolamine |
| PI | Phosphoinositide |
| PK | Polyketides |
| PL | Phospholipid |

| | |
|---|---|
| PLS-DA | Partial least squares-discriminant analysis |
| PLTP | Phospholipid transfer protein |
| POS | positive ionization mode |
| PR | Prenol lipids |
| PS | Phosphoserine |
| reTOF | Reflectron TOF |
| ROC | Receiver Operator Characteristic |
| ROI | Region of interest |
| S/N | Signal to noise |
| SIMS | Secondary ion mass spectrometry |
| SL | Saccharolipids |
| SM | Sphingomyelin |
| SMC | Smooth muscle cell |
| SP | Spingolipids |
| ST | Sterol lipids |
| TAG | Triacylglycerol |
| TOF | Time-of-Flight |
| TOF/TOF-MS | Tandem TOF mass spectrometry |
| TRG | Tumor regression grade |
| UN | Usual necrosis |

## Acknowledgements

The undertaking of my Ph.D. studies at the Université of Montréal has been a great adventure. I knew in coming to Montreal that I would be taking a risk and challenging myself academically, socially, and linguistically. My time and experiences here have been informative and irreplaceable.

Many people have made this work possible: my parents who raised me to be the person I am and have supported me throughout my studies, my wife Rebeca, who has been my benefactor at every turn, and Pr. Pierre Chaurand, who took the initial risk when he accepting me as a graduate student and has guided and challenged me during my time in his lab. I also thank Aurélien Thomas for his guidance and initiative in many of the projects he began as a post-doc that I finished during my Ph.D. Our discussions and debates about the direction of the projects lead to their current state. Martin Dufresne is also on my list of thanks for his discussion, knowledge and ideas, we both started our Ph.D.s around the same time and I've benefited greatly from discussions with him and his developments in sample preparation which I used in my finished and ongoing projects. The other students in the lab, Nidia Lauzon, Erik Fournaise, Elizabeth Kranjec and Ethan Yang are also thanked for their support.

My collaborators have been especially helpful in the conducting the projects and I extend my gratitude to Dr. Peter Metrakos, Dr. Anthoula Lazaris and Balqis Abdulkarim for their collaboration on the colorectal cancer liver metastasis project. Dr. Martin Marcinkiewicz at Cytochem also collaborated on these projects and I thank him for his instruction in histology, and specially thank him for the advice and wisdom he shared about science in general. My collaborators on the atherosclerosis project, Dr. Stella Daskalopoulou and RJ. Doonan, were helpful in advancing the project, and their discussions helped a lot in writing the 3D manuscript

and contextualizing the results. R.J. Doonan should be thanked for his work in preparing the massive 3D carotid sample.

Finally I'd like to thank my daughter Lorelei whose life brings mine immense joy.

# Chapter 1: Introduction

# 1.1 Mass spectrometry: little scale with big applications

Mass spectrometry (MS) generates and measures ions by their mass-to-change ratio (*m/z*). The insights of MS analysis have made significant impact and have revolutionized several fields of scientific inquiry; studies of proteins, metabolites, or environmental contaminants among many others have benefited immensely from MS technology.[1] MS analysis provides molecular identification by matching theoretical masses or through structural elucidation by tandem MS (MS/MS) fragmentation. Alongside identification, MS is also widely used for quantitation of molecules. Perhaps most importantly, MS techniques are applicable to mixtures of molecules and are scalable to very complex samples. Altogether, the use of MS falls along both the axes of discovery and routine in scientific analysis.

## 1.1.2 Matrix assisted laser desorption/ionization mass spectrometry

Fundamentally, a mass spectrometry measurement can be split into two phases: generation of ions in an *ion source* and analysis of ions by a *mass analyser*. The generation of ions is the necessary first step of an MS analysis and the ion source selected is based on where the analytes are situated. Analyses of liquid samples will benefit from electrospray ionization, an ion source that ionizes analytes dissolved in liquids.[2] For analysis of dry samples on surfaces, matrix assisted laser desorption/ionization (MALDI) is often used as an ion source. In bioanalysis, MALDI MS analysis of a higher mass protein (> 30 kilodaltons (Da)) was first demonstrated by Koichi Tanaka in 1987[3], for which he was awarded a quarter of the 2002 Nobel Prize in Chemistry. However, the specific development of MALDI may be more justly credited to Michael Karas and Franz Hillenkamp, who proposed organic “matrices” to induce desorption/ionization.[4] Since the demonstration of protein analysis by MALDI MS, it has been used in the analysis of biomolecules including peptides[5], lipids[6], amino acids[7], and many more.

Alongside its analytical capabilities in fundamental biological studies, it is being routinely used in clinical microbiology to differentiate bacterial strains.[8,9]

MALDI MS's advantages are numerous: MALDI MS is a "soft" ionization technique, meaning that the ionization event does not significantly fragment the ionized analytes and allows detection of the intact molecular ions. MALDI MS analysis usually generates singly charged species eliminating the need for deconvolution of isotopic patterns of ions in multiply charged states. Sensitivity in a MALDI MS analysis can be down to the femtomole. MALDI MS is also relatively tolerant to salt in the sample mixture. Finally, the direct generation of ions from a surface at discrete positions allows imaging mass spectrometry (IMS).

#### 1.1.2.1 MALDI sample preparation and ionization mechanism

MALDI, as its name implies, requires a matrix. The matrix is usually a weak organic acid capable of absorbing at the wavelength of the laser incorporated in the MALDI source, and is present in excess of the analyte (~5000/1). The sample preparation of a classic MALDI experiment involves depositing small volumes (microliters) of the analyte in solution on a target plate, and then adding the MALDI matrix in solution on top of the semi-dried analyte spot. The matrix and analyte co-crystallize during mixing and enable MALDI.

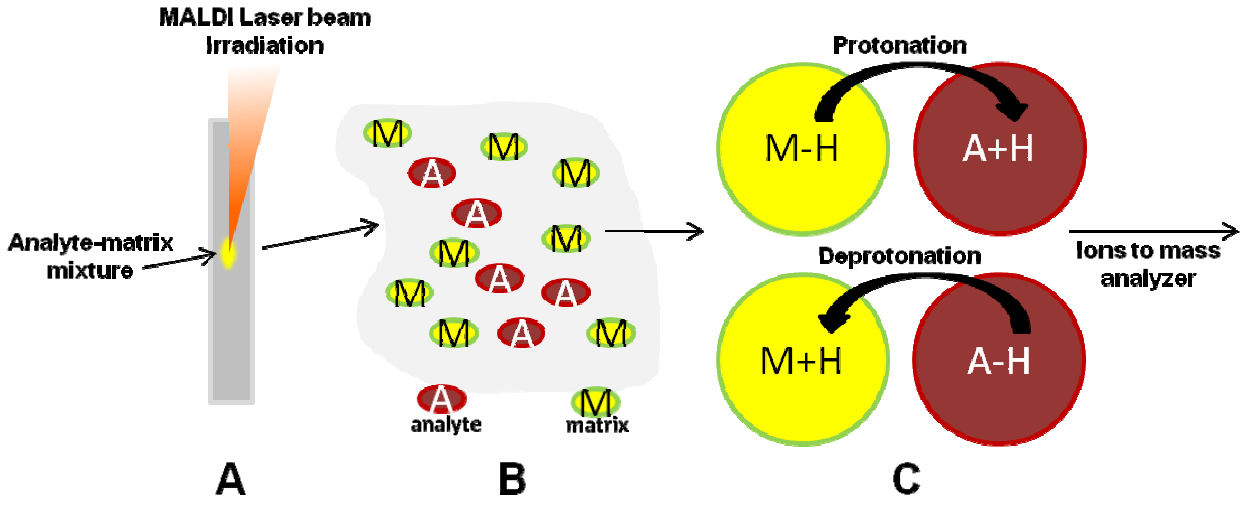


**Figure 1-1. MALDI ionization mechanism.** (A) The MALDI stage where the analyte-matrix mixture is located and fired upon by a brief laser pulse. (B) Ion plume where matrix and analyte interactions occur. (C) Proton transfer ionization in MALDI.

MALDI ionization is typically done under vacuum, but technical developments have enabled both intermediate and atmospheric pressure MALDI sources.[10] The mechanism of ionisation in a MALDI source is complex and is still studied and debated.[11] In theory ionisation can be described in three steps[12]: First, the laser pulse is fired at the analyte-matrix mixture where the matrix absorbs the MALDI laser and transfers energy to the surrounding material (**Figure 1-1** A). Secondly, the absorbed energy engenders desorption of portions of the analyte and matrix in the material from the surface into a gas phase plume (**Figure 1-1** B). Finally, the desorbed analytes and matrix interact in the gas phase plume, where analytes are ionised via protonation or deprotonation by the matrix (**Figure 1-1** C). Sample preparation and instrumental parameters also play important roles in the ionization mechanism: the matrix used, laser wavelength and dimension of the irradiated area will influence ion formation.[13,14] After ion generation, ions produced in the MALDI source are directed into a mass analyser.

### 1.1.2.2 Time of Flight (TOF) mass analyzer

Mass analyzers measure the *m/z* ratio of ions. In the case of Time-of-Flight (TOF) mass analysers, ion travel time over fixed dimension is measured. TOFs are the analysers most commonly coupled to MALDI sources and are notable for their simplicity, speed, and relatively low price[15]. Throughout this thesis work, MALDI-TOF was used.

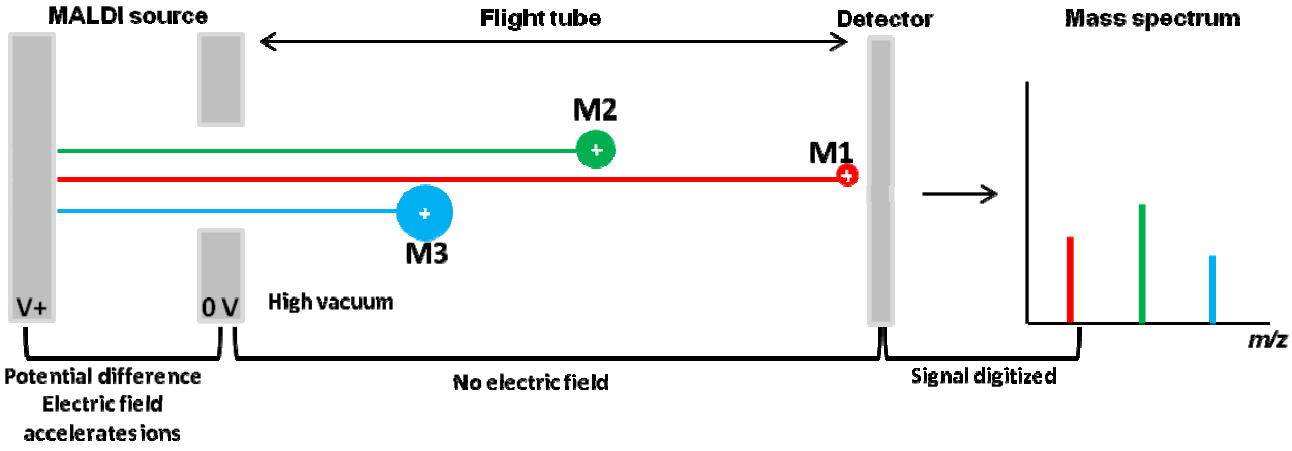


**Figure 1-2. Simplified schematic of MALDI-TOF MS.** The MALDI source depicts here the acceleration of ions towards the detector and not the MALDI event.

In its most simple form, TOF measurements can be represented as a hollow flight tube with the ion source at one end and an ion detector at the other. All ions are accelerated in an applied electric field and propelled to the detector after the ion creation event in the source (**Figure 1-2**). The time measurement starts from the ion creation event and ends as ions are detected. The flight time of the ion depends on the ion's kinetic energy, which depends on its mass. Rearrangement of the equations for potential and kinetic energy leads to a first order equation of the TOF process where mass over charge ratio can be derived from flight time (Equation 1):

$$t^2 = \frac{m}{z}\left(\frac{L^2}{2eV_x}\right)$$

**Equation 1. Relationship of time to mass-to-charge ratio in TOF-MS.** Where t is equal to time, m is equal the ion's mass, z is equal to the charge of the ion, L is length of the flight tube, and $2eV_x$ are instrumental acceleration parameters. Note: this equation does not consider time spent in the source, but is a general model of the relation between flight time and *m/z*.

Mass resolution is the measure of the mass spectrum's peak divided by its spread (full width at half mass) along the x-axis where higher mass resolution produces thinner peaks.

$$R = \frac{m}{\Delta m}$$

**Equation 2. Resolution in mass spectrometry.** m= measured mass of interested, Δm = the full width at half mass of the detected peak.

TOF resolution is proportional to the length of the flight tube; longer tubes give better resolution as the longer flight times allow better ion separation but ions cannot have an unlimited flight path. MALDI-TOF instruments can usually achieve at least 10,000 in mass resolution. Additionally, ion flight must necessarily be along as unobstructed of a path as possible in the flight tube. Any interference in space by collision with ambient gases will deflect the ion's path, and cause fragmentation of the ion, and arbitrarily increase its flight time and introducing fragment artifacts. This leads to less resolved peaks from shifted flight times and less sensitive analysis from the loss of ions. Thus, time of flight analysis is done under high vacuum (~$10^{-7}$ mbar).

#### *1.1.2.2.1 Advancing TOF technology: delayed extraction & reflectron TOF*

Key developments in TOF technology have improved mass resolution in TOF MS and made the technique much more powerful, namely the development of delayed extraction (also known as pulsed ion extraction) and reflectron-TOF (reTOF). Delayed extraction improves TOF mass resolution by centering the initial dispersion of ion velocity.

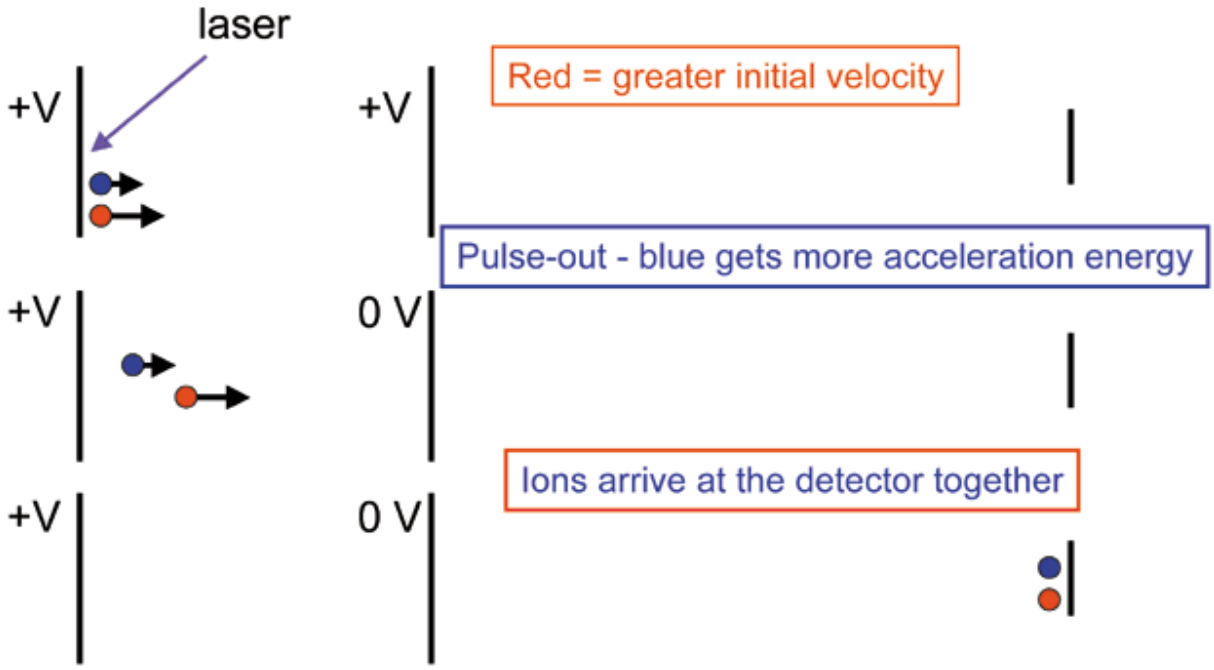


**Figure 1-3. Schematic of delayed extraction in TOF MS.** (top) The initial MALDI event generates ions of the same *m/z* with different initial kinetic energies, represented by arrows. (middle) The extraction pulse that accelerates the ions is delayed, allowing the ions with higher kinetic energy to travel further from the extraction plate. When the extracting potential is applied, ions with higher initial kinetic energy thus receive less energy, while the ions with low initial kinetic energy receive more (bottom). Ions finally arrive at the same time to the detector, decreasing peak bandwidth and thus increasing mass resolution.

Simply put, ions with higher initial velocity after the desorption event receive slightly less acceleration and vice versa (**Figure 1-3** A).[16] The ions of the same mass arrive at the detector at closer to the same time, improving resolution.

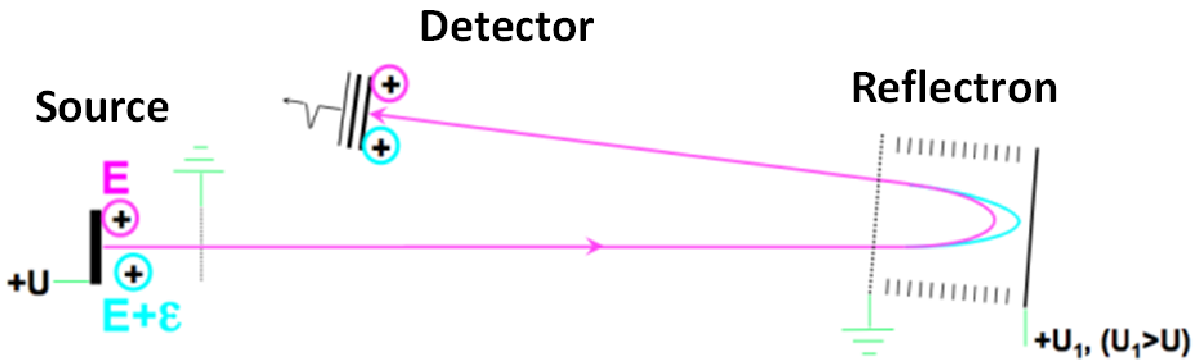


**Figure 1-4. Schematic of reflectron in TOF-MS.** Ions in blue and purple have the same mass to charge but slightly different kinetic energies. The ion with higher kinetic energy in blue penetrates further into the reflecton lengthening its flight time while the lower kinetic energy ion has a shallower penetration, with less extended flight time resulting in the quasi same arrival times for both ions on the detector. This correction improves mass resolution.

ReTOF is the use of electrostatic mirror (reflectron) to improve mass resolution. The reflectron deflects the ion beam along its flight path and lengthens flight time according to kinetic energy of the ion. Ions with higher kinetic energy penetrate more deeply into the reflectron's electrostatic field and vice versa (**Figure 1-4** B).[15] In a similar fashion to delayed extraction, reTOF improves resolution by centering detector arrival of ions at the same *m/z* but with different kinetic energies following the MALDI event. Early demonstration of the efficacy of the two improvements is shown in **Figure 1-5**.

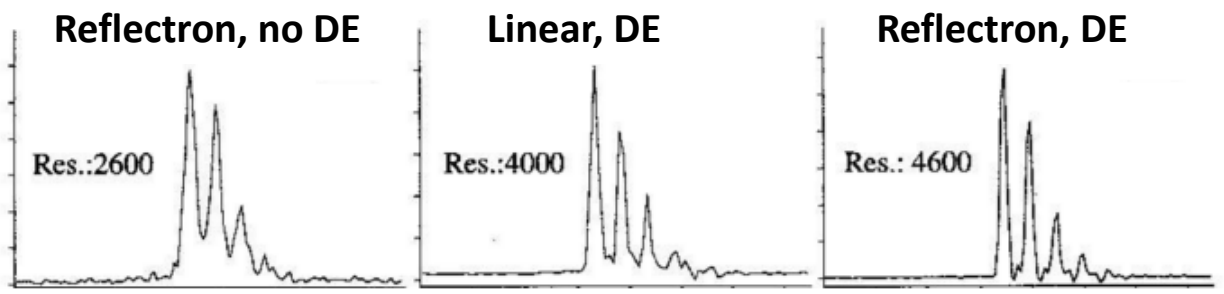


**Figure 1-5. Improvements in mass resolution combining delayed extraction and reflectron TOF.** DE=delayed extraction. Res. = mass resolution. Adapted from reference.[17]

#### *1.1.2.2.2 TOF/TOF tandem mass spectrometry*

Tandem mass spectrometry (MS/MS) can achieve structural identification of ions in the mass spectrometry experiment. MS/MS is isolation then fragmentation of a precursor ion followed by detection of the fragments. Ionized molecules fragment in ways characteristic to their chemical structure and to the fragmentation technique. For instance, certain chemical groups retain better a charge during fragmentation or are more likely to break during the fragmentation process. Accumulated knowledge of this chemistry has enabled structural identification. MS/MS is essential in almost every MS application. It can be used to compare experimental MS/MS results to MS/MS of standards, and databases of MS/MS fragmentation play a large role in identification of proteins[18] and other molecules[19]. In MALDI-TOF, MS/MS can be achieved with MALDI tandem TOF (TOF/TOF) through post-source decay analysis where a first analysis times the precursor ion out of source and a second uses excess laser energy at the MALDI event to create vibrational energy and induce fragmentation of the precursor ion during ion flight after previously timed mass filtering.[20] TOF/TOF MS is useful for peptide sequencing at higher masses but has limitations in the lower mass range where poor precursor selection (~4-6 Da windows) limits isolation of closely spaced *m/z*s in complex mixtures.

### 1.1.2.4 Other types of mass analyzers

MALDI can be coupled to other mass analyzers; notably, Fourier transform ion cyclotron resonance (FT-ICR) has been used. In FT-ICR, high field magnets are used to trap ions in a cyclical orbit. Excitation of the orbiting ions by use an electric field causes them to orbit at a frequency proportional to their *m/z*.[21] This type of mass analyzer is currently capable of achieving the highest mass resolution of all analyzers (R > 1,000,000)[22] but is among the most expensive MS instrumentation and is less robust than TOF. MALDI-FT-ICR is very useful in species identification as high resolution provides exact masses with very little error and detection of fine isotope patterns allow for easy hypothesizing of an ion's elemental composition.[23,24] FT-ICR works best in the mass range below 3,000 Da and thus very well suited to studies of small molecules. Besides increases in mass resolution, FT-ICR is also more sensitive than MALDI-TOF. In MS/MS studies, MALDI-FT-ICR systems are equipped with a quadropole prior to the mass analyzer that enables better precursor ion selection than TOF/TOF systems. The FT-ICR analyzer can implement integrate other technologies to perform novel fragmentation methods.[25]

## 1.2 MALDI Imaging MS (IMS): mapping molecules directly from a surface

MS of intact chemical species from surfaces has been demonstrated with MALDI, secondary ion MS (SIMS)[26] and desorption electrospray ionization (DESI)[27]. In practical terms, the leap from detection from surfaces to imaging is a matter of repeating the analysis at regular and known spatial intervals.[28] This type of analysis is called imaging mass spectrometry (IMS) and it allows label free spatial localization of molecules across surfaces. MALDI IMS holds the title as best performing IMS technology in sensitivity and application range as the "matrix" or sample preparation of MALDI MS analysis can be widely varied and largely determines the class of analytes that what will be analyzed.[29] The sample preparation is crucial in MALDI IMS, no matter the instrumentation or matrix used. MALDI IMS requires very homogenous matrix distribution across the surface with minimal analyte delocalization. In practice, MALDI IMS is achieved by rastering the MALDI laser across a surface, acquiring MS spectra at each coordinate according to a user defined shape and point-to-point resolution **(Figure 1-6)**.

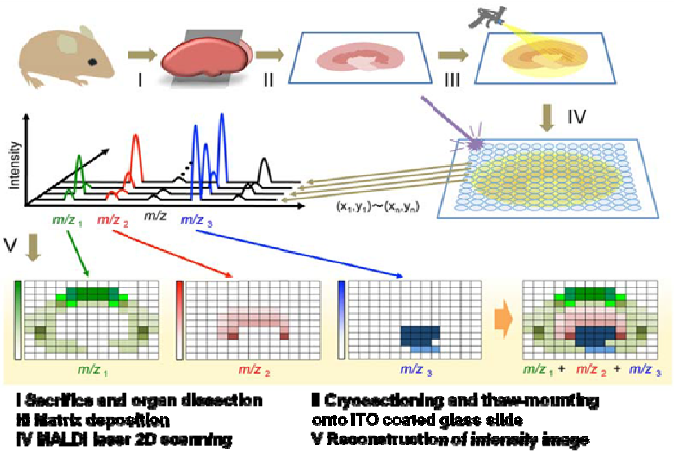


**Figure 1-6. MALDI IMS experimental workflow and image reconstruction.** Figure adapted from reference.[30]

SIMS achieves imaging through rastering similar to MALDI IMS but generates secondary ions through bombardment of the sample with a primary ion beam and does not require matrix. It can image at higher spatial resolution than MALDI but has limited mass range (typically < 1000 Da), sensitivity, and induces decomposition of organic species during bombardment.[31] DESI is another technique for IMS that uses a focused electrospray beam moved across a surface to desorb and ionize *in situ* molecules then captures ions into an analyser. DESI is promising for applications as it requires minimal sample preparation and can be achieved through modification of an inexpensive ESI source.[32] Other novel IMS technologies have also been demonstrated.[33]

The advantages of MALDI IMS in comparison to other molecular imaging technologies such as fluorescence, immunohistochemistry (IHC), or RAMAN imaging[34] are untargeted and label free analysis, low detection limits, and specificity to analytes simply by choice of sample preparation as well as identification of the exact chemical species imaged. IHC has been widely used to image anti-gens (usually proteins) in tissue sections through antibody reaction. In most applications, the antibodies are tagged with a fluorophore and can thus be imaged with fluorescence microscopy. IHC localizes one protein and has the added risk of non-specific binding of the anti-body and multiplexing can be complicated.[35] In contrast, MALDI IMS can detect many proteins in one analysis but has lower throughput. For validation of the detected species, structural determination also eliminates potential false positives.[36,37] Beyond proteins, imaging of many different small molecules was not possible before IMS. For example, there are few and limited complementary imaging techniques to validate IMS localization of individual lipids. IHC could detect a lipid with an attached oligosaccharide, but will not differentiate the lipophilic portion of the lipid.

Some apparent limitations in IMS are unknowns in ionization efficiency as all chemical species are ionized in one event and this may lead to ion suppression and the favorable ionization of

some molecules over others.[38] This presents a problem in comparing the relative abundance of ions in IMS data. Another current limitation is imaging resolution.[39] Fluorescent microscopy can image at the subcellular level[40], while the best commercial MALDI instrumentation tops out at 5 μm imaging resolution.[41] Beyond the necessity for better instrumentation, there is dramatic decrease in sensitivity at high spatial resolution. However, these problems are not inherit to the analysis and can be improved with better technology and sample preparation.[26]

### 1.2.1 Thin tissue sections in MALDI IMS

The most active area of MALDI IMS research is imaging of thin sections from mammalian tissue.[29] Here, endogenous and exogenous molecules can be detected from the tissue section with their localization giving clues about biological processes, disease processes, and/or pharmokinetics[42]. Although tissue sections of mammalian origin have garnered the most attention, recently plants[43-47] and insects[48-53] are being imaged with promising results.

Experimentally, IMS of thin tissue sections is most often performed with fresh frozen tissues rather than tissues embedded in media (such as paraffin[54] or PaxGENE[55,56]) used in many pathology applications. Fresh frozen here implies that after dissection of the tissue, it is “snap frozen” by plunging it into liquid nitrogen or isopenthane or by placing it on dry ice and then stored below freezing (-80°C) until use. Fresh frozen tissues preserve the molecular content of the tissue in its native state but the quality of the tissue architecture for microscopy after staining is poorer and the tissue itself must be freezer stored and may have a limited lifetime. Fresh frozen tissues also require cryo-sectioning (cut at temperatures typically < -10°C). Tissue work in pathology has focused heavily on formalin-fixed paraffin-embedded (FFPE) tissues. FFPE tissues use formalin as a fixative that preserves the tissue architecture and can preserve some RNA and DNA. The fixation works by cross-linking protein amino acids within the tissue with formaldehyde. This protein cross-linking can be undone by the use of heat during the anti-gen retrieval phase.[57] The paraffin embedding step allows the samples to be stored at room

temperature and archived for years with limited degradation. Indeed, many pathology labs have enormous banks of FFPE tissue. FFPE tissues can also be analyzed by MALDI IMS for protein and protein modifications, but only after an enzymatic digestion due to the aforementioned protein cross-linking. Typically, the digestion is done with trypsin for peptides but recent novel enzymatic digestions have been proposed such as N-glycosidase F for N-glycans attached to proteins.[58,59] The work presented in this thesis uses exclusively fresh frozen tissue as it is the only means to access lipids.

## 1.2.2 MALDI IMS of lipids

### 1.2.2.1 MS key in the field of lipidomics

In fresh frozen tissues, MALDI IMS can image major classes of endogenous biomolecules including proteins, peptides, lipids, and primary metabolites. Lipids are of particular interest because of their diverse functions. The importance of lipids has been highlighted in studies showing their dysfunction at the metabolic level being implicated in cancer[60], diabetes[61], and many other diseases and a more thorough discussion of this will be presented in the next section.[62] The burgeoning field of lipidomics attests to the biological importance of lipids and to the rapid technological developments in MS during the last 20 years.[63]

### 1.2.2.2 Brief introduction to lipids imaged by MALDI IMS

| Category | Abbreviation | Structures in Database | MALDI IMS |
|---|---|---|---|
| Fatty acyls | FA | 6954 | Y[64] |
| Glycerolipids | GL | 7542 | Y[65] |
| Glycerophospholipids | GP | 9387 | Y[66] |
| Sphingolipids | SP | 4352 | Y[67] |
| Sterol Lipids | ST | 2833 | Y[68] |
| Prenol Lipids | PR | 1257 | N |
| Saccharolipids | SL | 1293 | N |
| Polyketides | PK | 6742 | N |

**Table 1-1. Classes of lipids from LIPID MAPS and whether the class has been imaged by MALDI IMS**. Stuctures in database are the number of structures for each lipid category in the LIPID MAPs database (as of April 2016). Y= yes, N= no.

Lipids are hydrophobic or amphiphilic small molecules generally recognized for their solubility in non-polar solvents. LIPID MAPS is the most widely accepted lipid database and currently divides lipids into eight major categories: fatty acids, glycerolipids, glycerophospholipids, sphingolipids, saccharolipids, polyketides, sterol lipids, and prenol lipids. Each category also includes many subcategories not listed here. **Table 1-1** presents the number of entries for each lipid class in the LIPID MAPS database as of April 2016, and whether to date they have been imaged by MALDI. **Figure 1-7** shows pertinent example structures. Saccharolipids and polyketides, not yet imaged by MALDI IMS, are primarily found in microorganisms. Given the increasing interest in microbial studies by MALDI IMS[69] and their detection by other MS techniques[70,71], these species are likely to be detectable by IMS in the near future. A brief introduction to each subcategory of lipids and background on lipid nomenclature will be provided in this section.

#### *1.2.2.2.1 Fatty acids*

Fatty acyls (FAs) are polar carbon chains (aliphatic chains) with a carboxylic acid end that serve as building blocks of many other lipids as well as having function of their own as free FAs (FFAs). FAs are generally synthesized in the liver from carbohydrates and incorporated into triacylglycerols (TAGs) for storage or as the side chains in phospholipids. FFAs are released due to breakdown of other more complex lipid species. Their nomenclature is important and incorporated into other lipids with FAs. It is distinguished by the number of carbons, number of unsaturations (carbon double bonds on FA chain), position of the unsaturations along the chain, and orientation of each position (*cis* or *trans*). In bioanalytical work, the *cis-trans* orientation of the double bonds is often ignored as *trans* orientations are not found in nature. As an example

of FA nomenclature, docosahexaenoic acid (DHA) is reduced to C22:6n-3,6,9,12,15,18, and in many cases simplified to C22:6 as MS techniques to locate the double bond are relatively new and not yet widely used but will likely prove to be important.[72-75]

#### *1.2.2.2.2 Glycerophospholipids*

Phospholipids (PLs) form cell membranes as lipid bilayers, and can signal cell activity directly from modification at the cell membrane. Structurally, they are amphiphilic with one polar end (head-group) and other non-polar end of two FAs. In lipid membranes, composed of bilayers, the headgroup ends are towards in the exterior and interior of the cell (the surrounding aqueous environment) while the hydrophobic ends interact in the interior of a lipid bilayer. Phosphotidylcholines (PCs) are a major subclass of PLs and the majority of lipids in absolute quantity, and are the primary class composing lipid bilayers in membranes. Alongside the abundant PCs, there are phosphoethanolamines (PEs), phosphoserines (PSs), phosphotidic acids (PAs), and phosphoinositides (PIs). Besides the basic form of PLs, PL species are regularly modified into their lysoPL and into diacylglycerols (DGs) by cleavage of one of the FAs or the headgroup by a phospholipase enzyme. LysoPLs and DGs are implicated in cell signaling.[76]

PL nomenclature incorporates FA nomenclature; PC(16:1/16:1) would denote a lipid containing a phosphotidylcholine head-group with two FA residues of C16:1. A lysed version of the same molecule would be denoted LPC(16:1).

#### *1.2.2.2.3 Sphingolipids*

SPs are a group of lipids based on an 18 carbon amino-alcohol backbone as shown in Figure 1-7. The diversity of SLs includes important subcategories such as sphingosines, ceramides (Cer), sphingomyelines (SM), and cerebrosides among others. The diversity encompasses phopholipid headgroups, phosphate species, and sugar residues linked to the sphinolipid

backbone. These structural differences are consequential biologically and SLs have been implicated non-exhaustively in cellular apoptosis, proliferation, necrosis, inflammation, and differentiation[77-81].

#### *1.2.2.2.4 Glycerolipids*

Glycerolipids are an important and more narrowly defined class of lipids containing a glycerol backbone with FAs attached. The most common of which is the diacylglycerol and triacylglycerol (TAG), sometimes referred to as di- and triglyceride. These lipids are heavily implicated in energy storage and compose the bulk of adipose tissue. Metabolism of glycerolipids is one source of cellular energy.[82,83]

#### *1.2.2.2.5 Sterol lipids*

Sterol lipids are structurally disparate from the previously described lipids as their base structure is the fused four ringed sterol. The most notable examples are cholesterol and cholesterol metabolites like testosterone. Cholesterol is integral in the cellular membrane and its modification to hormonal steroids control many biological processes on short (metabolism, inflammation) and long time scales (secondary sex differentiation).

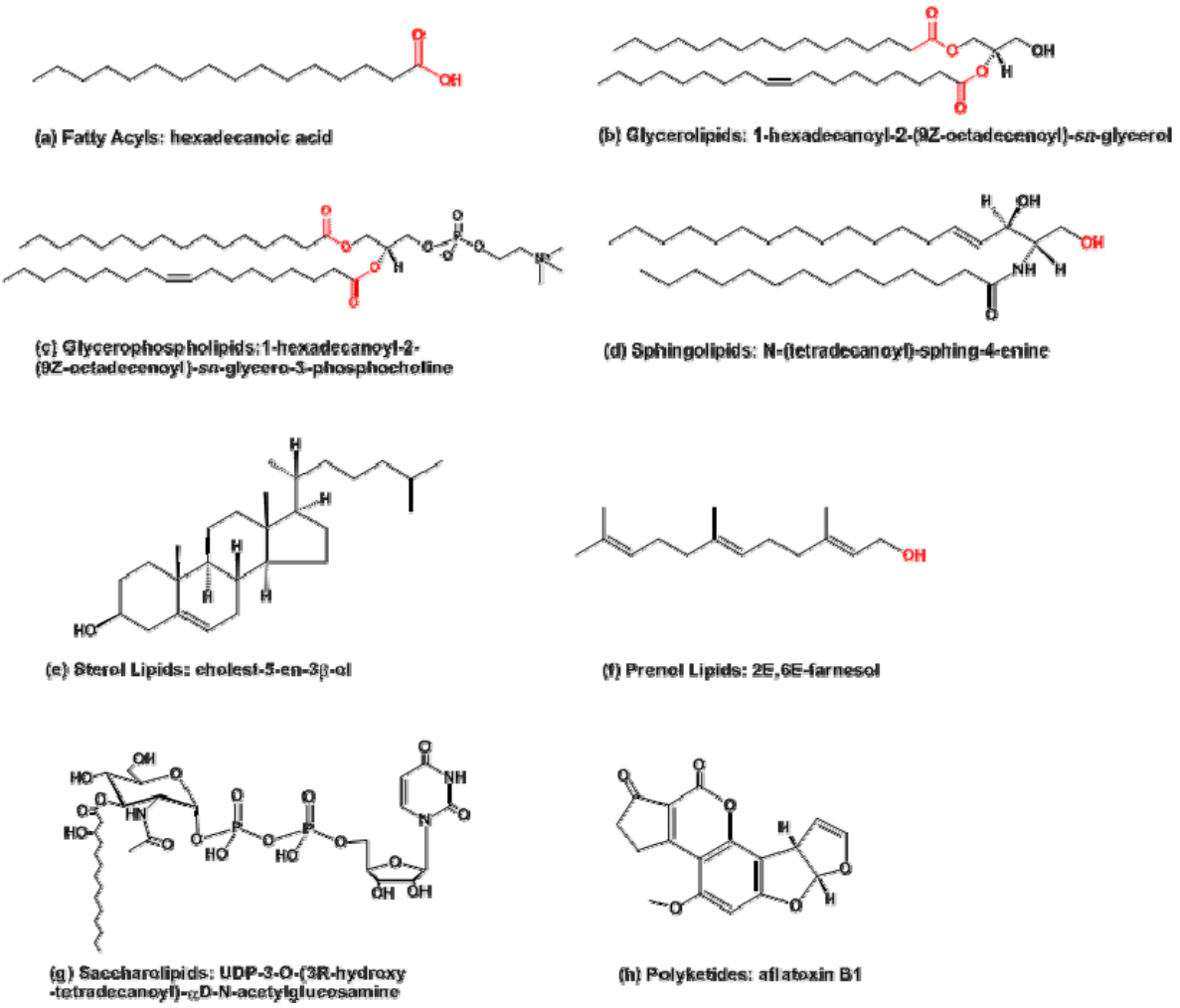


**Figure 1-7. Examples of lipid structures from the main classes.** Figure demonstrates the chemically simple FAs and their use as building blocks of more complex lipid and the sterols structural difference to other lipid classes. Figure from reference.[84]

### 1.2.2.3 MALDI IMS experimental aspects with lipids

It is simple to infer from the expanse of lipids in biology that localizing them in biological samples offers novel insights. The relative ease of lipid IMS is due to the high abundance of lipids in cells, the fact that many species contain charged headgroups which readily form cations/anions, and that most lipids have molecular weights in the mass range where modern MS instruments are most sensitive and possess the best resolving power (< *m/z* 2000). Despite

this seeming coalescence of factors, imaging of lipids by MALDI was first introduced in 2005[66], a few years after studies had demonstrated protein imaging. The first critical development in MALDI MS of lipids is sample preparation. This had been achieved through matrix choice for MALDI analysis of dissolved lipids, and eventually by spraying matrix onto tissue sections. Since the beginning of MALDI IMS, techniques in matrix deposition have advanced. At the outset, depositions using matrix dissolved in solvent were used almost exclusively, and remain in common use. As such, automated sprayer systems have been commercialized greatly improving reproducibility. In solvent free matrix application, sublimation of matrix onto tissue samples was demonstrated as highly effective for PL analysis.[85] Sublimation works well in MALDI IMS because it yields a highly uniform matrix layers across tissue sections. The added step of matrix recrystallization after sublimation has shown that a combined sublimation/solvent application can also be beneficial.[86,87]

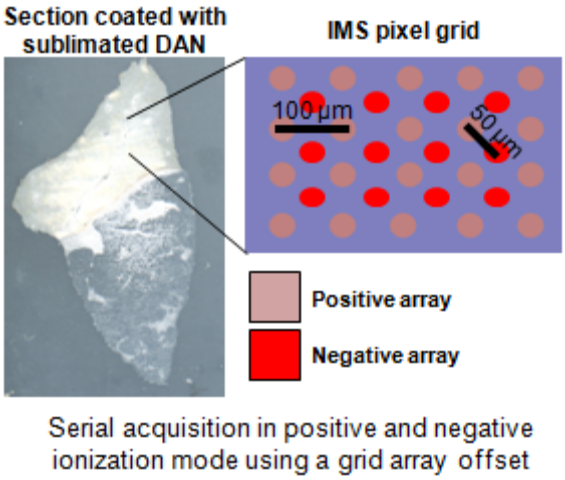


**Figure 1-8. Schematic of dual ionization mode imaging.** Grid offset is displayed by two color pixel locations.

MALDI IMS of phospholipids has been achieved at <1 µm imaging resolution by employing matrix sublimation.[88] Sublimation of matrix primarily produces ions of PLs with charged headgroups: PCs, PEs, PSs, PIs and many SLs. As previously outlined, PLs are diverse; some

PL headgroups are charged negatively and others positively and thus more easily ionize through protonation or deprotonation. Thus capturing the full spectrum of species requires analysis in both positive and negative ionization mode. With performance of most matrices limited to a single ionization mode, it was discovered that 1,5-diaminonapthalene (DAN) offers high sensitivity for PLs in both modes and the option of sublimation.[89] Dual ionization imaging, shown in **Figure 1-8** utilizes DAN in acquiring both a positive and negative dataset on a single tissue section and is performed using an x-y imaging grid offset of ½ the imaging resolution.[90]

The use of metals as desorption/ionization agents in IMS has also been important to lipid analysis. Silver-assisted LDI (AgLDI) IMS uses sputtered or evaporated silver layers on tissue sections to achieve imaging of FAs, cholesterol, cholesterol esters and other olefin containing compounds.[65] More recently, gold-assisted LDI has been used to image TAGs with high sensitivity.[65]

There are drawbacks of MALDI analysis for lipids, chiefly the fact that MALDI matrices may produce signals and spectral noise in the mass range of lipids. This has its largest effects on species below *m/z* 450 where most matrices produce the majority of their molecular, adduct, and fragment ions. Above *m/z* 450 contaminating matrix signals can still be observed, but in the case of DAN, the matrix adduct ions are primarily detected in regions with few lipid signals. Downstream data analysis also easily allows elimination of matrix species from analysis, however, the effect of the matrix on ionization efficiency could be important.

#### *1.2.2.3.1 Lipid identification through MS and MS/MS*

Identification of lipids in MS experiments usually begins with searching the exact mass of the lipid in a database. High mass resolution instruments are best suited for this task, but a well mass calibrated TOF method is usually accurate enough to be within Δ0.1 *m/z* at maximum deviation. With lipids there are often many species with closely spaced in mass or even with the

exact same mass and different structure. The potential structures can be hypothesized by experimental mass alone but must be confirmed by MS/MS.

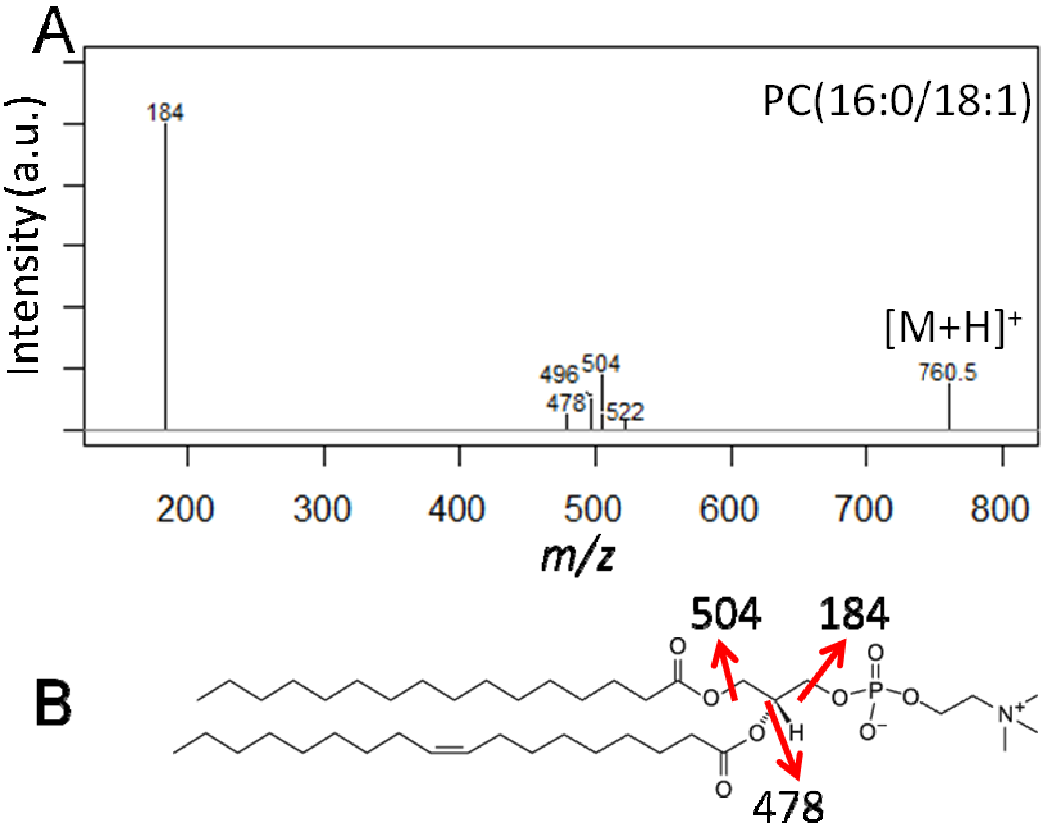


**Figure 1-9. MS/MS of PC(16:0/18:1).** LC-ESI-MS/MS by collision induced fragmentation of PC(16:0/18:1) standard. Figure adapted from reference.[91] (B) Fragmentation pathways showing loss of PC headgroup, and the two FA chains. Note: the position of the double bond is just a placeholder, as this MS/MS does not provide it.

MALDI MS/MS of lipids returns characteristic fragments in most cases. GLs, GPs, and SPs all contain FAs and sterol lipids also can contain FAs chains. In GPs and SPs, headgroups are attached to the two FA chains by a phosphate group. The loss of FAs in MS/MS of GLs, GPs, and SPs is one of the most common and characteristic fragmentation pathways, but also found in other lipids categories. Loss of the headgroup is another very characteristic fragmentation in

GPs and SLs. Indeed, any lipid MS/MS with a fragment at *m/z* 184 (PC headgroup) is likely to be a PC species, and other characteristic headgroup fragments exist. In the case of SL where several sugar residues form the headgroup, the sugar residue may be sequenced. PC(16:0/18:1), as shown in **Figure 1-9**, contains two FA side chains at sn-1 and sn-2 position, and the loss of these two side chains along with the loss of the headgroup can confirm the structure after database search of the original mass. Elongation of FAs during synthesis is done 2 carbons at a time and this has important consequences in MS identification; for a single mass and a given tolerance, many lipids will be present, but the removal of rare odd-chain FAs clarifies candidate structures before MS/MS. For instance, PC(17:0/17:1) has the same mass as PC(16:0/18:1), however, the rarity of PCs with odd chains limits the possibility of it as a potential ID.

As mentioned in the primer on fatty acids, locating the double bonds in fatty acids chains remains an MS challenge, but another potential solution that is not MS/MS based is the use of ion mobility MS. Ion mobility MS measures the collisional cross-section of ions and can give clues about their shape in the gas phase. As the structure and shape of the lipid is determined by the position of the double bond, ion mobility may be able to help determine the location of the bond by changes in the mobility profile. [92]

## 1.3 Disease applications

MALDI IMS has already touched a multitude of diseases at the fundamental and clinical level. Indeed, the desire to track and localize molecular changes in diseased tissue sections has been the driving force behind developments in IMS in every direction. The field has an ever growing number of applications with cancer being one of the primary focuses.[93,94] Much of the work by IMS in cancer has focused on classifying cancerous tissue[95,96] against normal tissue and stratifying samples based on IMS signals or to discriminate types of cancer in a given tissue.[97,98] Many of these developments have led to strong correlation with clinical pathology[99] as well as

improvements through new IMS-based clinical criteria.[100] Fundamental studies in cancer are also aided by IMS; they benefit from direct localization of important biomolecules and in conjunction with histological staining data give the specific cells expressing the biomolecule.[101] Importantly, IMS studies working with human tissue are working directly with real patient samples and not models, adding a level of validity and immediate applicability to the results. In IMS studies the analysis of real samples is complicated by naturally heterogeneous samples but when results are consistent across a large cohort they are undoubtedly robust. Besides cancer there has been research in other diseases and it has become difficult to monitor all the different diseases in the field as the technique can be applied to nearly any tissue, some examples include brain, kidney, or retinal diseases.[102-105] However, what was true above about cancer is largely true about any disease studied by IMS. An important first step in utilizing IMS is considering the basics of a disease. In the aim of providing background on the diseases studied in this thesis the following sections give brief introductions to atherosclerosis and colorectal cancer liver metastasis.

## 1.3.1 Cardiovascular disease and atherosclerosis

Cardiovascular diseases (CVDs) are diseases affecting the vasculature and its function in delivering blood to tissues. CVD is the leading cause of death in the world[106] and the primary risks are related to lifestyle. Atherosclerosis is a CVD with chronic inflammation resulting in a build-up of white blood cells and smooth muscle cells (SMCs) at the arterial wall. Atherosclerosis leads to hardening of the arteries.

### 1.3.1.1 Atherosclerosis disease progression

The arterial wall tissue contains 3 layers: intima, media, and adventitia (**Figure 1-10** a). The progression of atherosclerosis begins with deposition of inflammatory cells into the intima. Under normal circumstances, the outer endothelial layer in contact with circulating blood allows

white blood cells to pass without attachment, however, in atherosclerosis, abnormal blood lipid profiles, high blood pressure or pro-inflammatory mediators cause the outer endothelial cells to express adhesion molecules at their surface which capture monocytes in the blood. The monocytes are deposited into the arterial intimia and begin maturing into macrophages (**Figure 1-10** b). The mature macrophages uptake lipids from low density lipoprotein (LDL) particles that have also penetrated into the intima due to the more permeable arterial wall and develop into foam cells when engorged with the lipids.[107] After foam cells begin to develop, SMCs migrate from the media to the intima and produce extracellular matrix molecules such as collagen. Eventually, this collagen rich environment can cover the plaque and harden it with a fibrous cap. Within the fibrous cap, some macrophages turned foam cells die and their cellular contents are released into the extracellular matrix. The lipids and cellular debris of the apoptotic foam cells build up in the plaque and form a lipid-rich necrotic core (**Figure 1-10** c). [108]

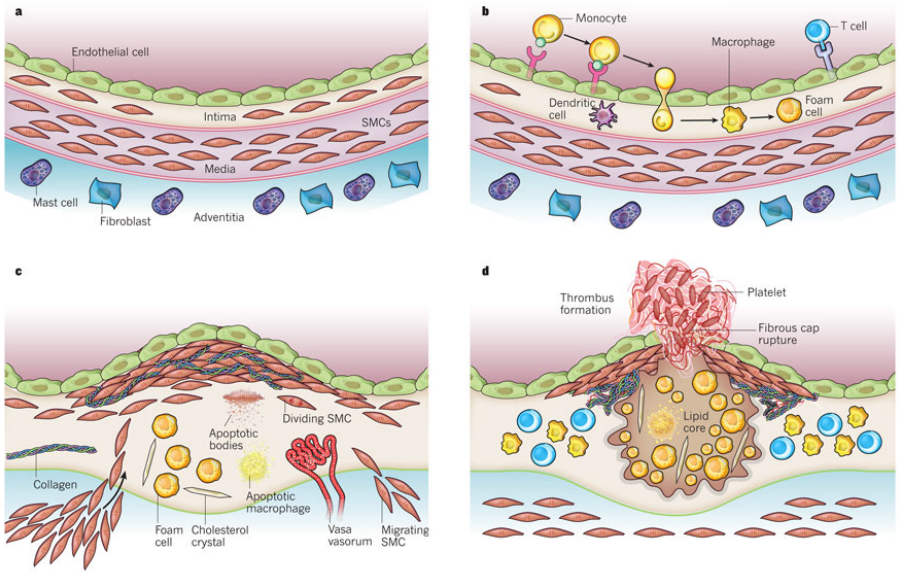


**Figure 1-10. Schematic of atherosclerotic progression.** (a) Normal artery showing the arterial layers. (b) Initial stages of plaque development with white blood cell invasion and of LDL

in the intima. (c) later plaque development with invasion of SMCs in the intima, and development of a fibrous cap. (d) late stage plaque development with a large lipid core and rupture of the plaque. Figure taken from reference.[109]

The end stage of plaque development can either be thinning of the fibrous cap and release of the accumulated cellular material into the bloodstream or complete occlusion of the blood vessel at the site of the plaque (**Figure 1-10** d). Thinning of the fibrous area of plaque is due to inflammatory cells releasing enzymes which breakdown the collagen and other extracellular matrix materials composing the plaque. As the plaque thins, it is ruptured by the mechanical forces of the blood pressure, thus the risk of high blood pressure with plaques. When release, the accumulated atherosclerotic material in the bloodstream quickly triggers an inflammatory response and causes coagulation of the material into a thrombosis. The thrombosis can occlude at the site of the plaque or further downstream in smaller vessels. Most notably, rupture of plaque at the carotid artery in the neck often occludes downstream blood vessels in the brain causing stroke.[109]

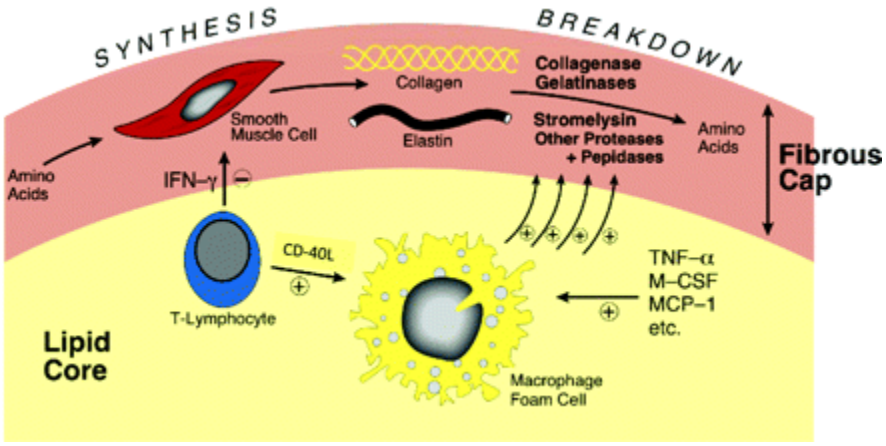


**Figure 1-11. Processing of extracellular material at fibrous cap.** The synthesis and breakdown of extracellular material between the macrophages and SMCs which leads to

thinning of the cap and less resistance to shearing by the mechanical force of blood pressure. Figure taken from reference.[110]

Atherosclerosis plaques in humans are individually unique and develop over a lifetime although most complications occur in the second half of life. One often cited study performed autopsies on healthy, young soldiers who died in the Korean War and found many already had developed plaques before the age of 30.[111] Plaques generally exist on a spectrum of fatty to fibrotic with fatty plaques being at higher risk of rupture.[110] The development of a fatty or fibrous plaques depends on the balance between inflammatory cells and SMCs in the plaque. The inflammatory cells accumulate lipids and develop the necrotic core, while the SMCs produce collagen and other reinforcing molecules into the plaque (**Figure 1-11**). The highly fibrous plaque is thus less likely to rupture by the previously described mechanism. The inflammation-related rupture has also been highlighted by the increased risk of plaque rupture in patients with acute illness.[110]

#### 1.3.1.2 Analysis of atherosclerotic plaques

Analysis of atherosclerotic plaques is done through a variety of techniques, including *in vivo* imaging. The foremost examination of plaque character comes from pathological analysis of stained tissues, where histologically distinct areas are recognized by their coloring with dyes. This approach is useful in examining some of the gross morphology and structure of plaques but has little clinical applicability as it is *ex vivo*. Clinically, plaque is often assessed by ultrasound imaging, where the degree of plaque occlusion of the artery (stenosis) is determined and measures of blood flow around the plaque give some indication about its development. However, highly stenotic plaques are not necessarily high-risk plaques in that stenosis is not always related to rupture, and indeed, the elucidation of the fatty atheromas as high-risk has led the need for alternative assessment of plaque vulnerability. In this aim, magnetic resonance imaging and other tag based *in vivo* imaging platforms have been used. MS has been implicated as well, but the invasive sample requirements lead to MS working in a discovery role

in determination of the biomolecular character of plaque diversity or working with biofluids to determine any CVD association.[112]

## 1.3.2 Colorectal cancer and colorectal cancer liver metastasis

Cancer is another major leading cause of death globally. Cancer is abnormal cell growth that can spread from one organ or area to another (metastasis). Cancer causes malfunction of the organ's where it has infiltrated and is due to environmental and genetic factors. Colorectal cancer (CRC) is cancer in the large intestine at the colon and rectum and is the third most common cancer globally as of 2014.[113] CRC originates from the endothelial cells lining the colon or rectum and often is an adenocarcinoma, or glandular mucus secreting cancer. Early detection of CRC by colonoscopy and surgical resection can often be curative, but metastatic CRC has a poorer prognosis. Particularly, the liver as a metastasis site (colorectal cancer liver metastasis (CRCLM)) is common, and surgical resection has curative potential but it is not applicable in all CRCLM cases.[114,115]

### 1.3.1.1 Colorectal cancer liver metastasis progression

CRC metastasizes when CRC cells detach from the colon or rectum and enter the blood or lymphatic circulation and attach to other organs. CRC cells that metastasize have often progressive mutations which allow them to proliferate in face of immune response at the colon/rectum and in the circulatory system. Alongside these protective mutations, the colon area is also transformed by the CRC progression and develops "leaky vasculature" whereby the mutated CRC cells can enter the bloodstream.[116] Despite the mutations, metastatic cancer cells have a very small chance of survival with recent studies indicating 0.01% of cells survive the circulatory system, where mechanical stress or immune response kills them.[117,118] For the metastatic cells that do survive, the liver is a common site for proliferation given its major role in metabolism and therefore interaction with circulating bio-fluids. Once the circulating tumor cells

reach the liver, they attach to the basement membrane and form micro-metastases (**Figure 1-12**). These small areas of cells are often clinically silent and in many cases, die out before growth into debilitating tumors. Indeed, survival in the external environment is rare.

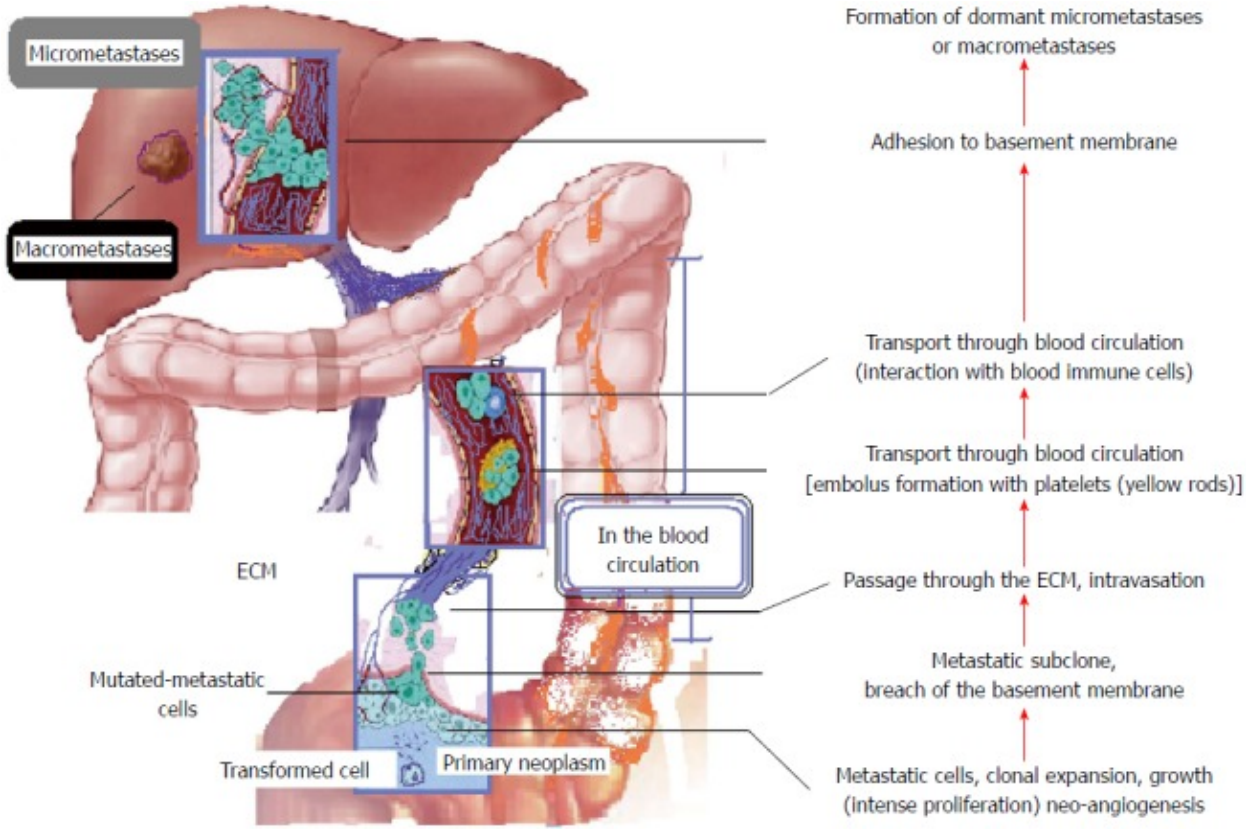


**Figure 1-12. Process of hepatic invasion by colorectal cancer cells.** Schematic explaining the steps initial cancerous development to attachment in the liver. From reference.[116]

In the cases where larger macro-metastases are formed, CRCLM slow moves from the liver sinuses to the normal liver tissue, eventually affecting function. Lipid analysis has clarified some biology of the CRC process.[119]

### 1.3.1.2 Colorectal cancer liver metastasis diagnosis, treatment and monitoring

CRCLM is usually detected after the initial CRC has been detected, and CRCLM is said to be synchronous or asynchronous if has occurred with the detection of the CRC or after the

detection of the CRC. Because CRCLM can occur even after clinical silence of CRC, monitoring and follow up is important. Typically, CT scans of the liver are performed and tumor nodules are counted and sized. From here, there is the option of chemotherapy or surgical intervention. Pre-surgical assessment of the tumor is very important and a small biopsy may be taken and examined by a pathologist after staining. In the case of surgery, large sections of the liver are removed (up to 60%) and all nodules and surgical tumor margins considered. IMS can complement a surgical biopsy but in general, the biopsy is small and it may be difficult to reliably assess with IMS alone. However, when large amounts of liver are excised, tumor lesions can be banked and explored by IMS with the aim of developing IMS data to guide biopsy analysis.

## 1.4 Large cohort applications of IMS

Development of IMS technology and demonstration of IMS's utility has made analysis of ever larger cohorts inevitable. Most imaging capable commercial MALDI-TOFs are capable of 2 pixel/s imaging with next generation commercial MALDI-TOFs capable of 25-50 pixel/s imaging, increasing speed by up to 25 times.[120] Tissue lipid analysis by MALDI-TOF is thus on the cusp of high throughput and/or high imaging resolution analysis of large cohorts. This movement stretches all aspects of the imaging process: more data being acquired demands faster, more robust instrumentation. More samples being analyzed alongside higher imaging resolution necessitate data analysis workflows that rapidly return valuable information. More users being integrated into IMS requires data analysis workflows that can be easily examined and interpreted by non-experts. Addressing these concerns and in order to standardize the field, researchers in IMS are attempting multi-institutional studies to validate findings, a vendor-neutral data format (imzML) has been developed[121,122] along with public IMS databases[123], and standard reporting guidelines are being proposed.[124,125] Although the call for standardization has highlighted a weak point in the field of IMS, there does appear to be some consensus on IMS data quality as expert survey has demonstrated.[126] This thesis' work has partly addressed the

call for standardization with sample handling protocols. The work has also addressed accessibility, and strategies for data analysis that easily interpreted.

## 1.4.1 Practical considerations: lipid degradation

Technological and methodological IMS advances apply to studies of cohorts of tissues from multiple patients/animals, but also 3D imaging, where many sections are acquired from a single tissue. Any IMS experiment needs guidelines in how the samples should be physically handled. This is especially important in lipids as they are subject to oxidative degradation.

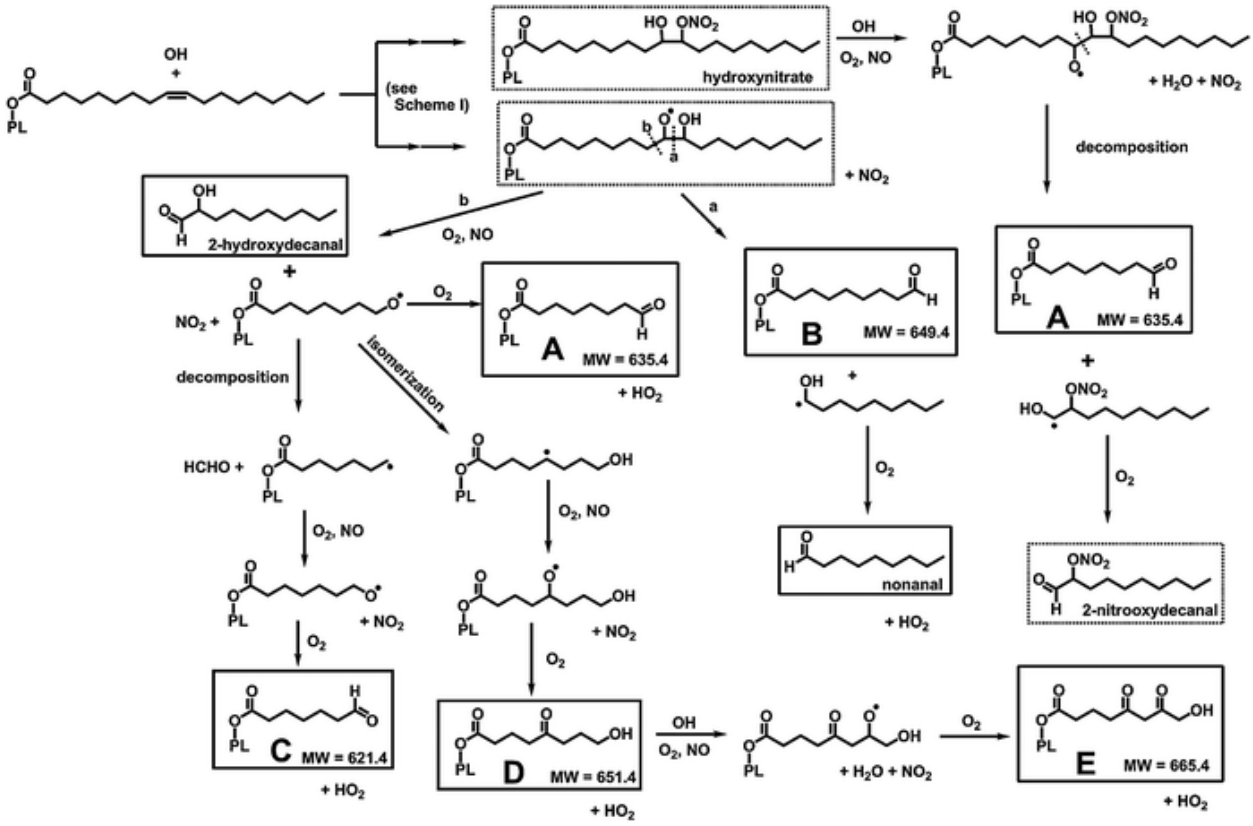


**Figure 1-13. Mechanism and resultant structures of peroxidation along unsaturated FA chain.** Top left is the initial FA chain with one unsaturation, followed by radicalization and hydrogen abstraction to the right. The site of hydrogen extraction is then replaced by peroxide which is finally reduced to a variety of positions and structures. From reference[127].

Lipids containing FAs are subject to peroxidation at unsaturations along the FA chain. This oxidation is responsible for the smell of fish and is fought in the food industry through additives. The same processes are applicable to the lipids imaged by MALDI as all can contain a FA. The oxidation occurs when hydrogens adjacent to FA unsaturations, weakened from the double bond, undergo free radicalization and accept atmospheric oxygen along the FA chain. After the oxygen is added, oxidation can take many forms (**Figure 1-13**).[128] Importantly in the imaging of lipids, oxidized species will diminish the abundance of the naturally occurring lipids, introduce oxidized lipids as artifacts, and reduce the validity of any lipid results. Oxidized lipids may also have different ionization efficiencies than normal lipids due to the shorter chain lengths which generally ionize more efficiently.

## 1.4.2 Serial 3D IMS

Serial 3D IMS is the 3D reconstruction from multiple 2D datasets acquired in regular intervals in the x,y and z plane (**Figure 1-14**). Non serial 3D IMS like 3D SIMS can be used for depth profiling of a tissue section or material study: in this case, 3D imaging is done by imaging a layer, sputtering a layer of material off, and imaging at the deeper depth and finally reconstructing in 3D the data acquired at several depths. 3D SIMS provides high resolution in the z plane but is not currently practical for 3D reconstruction of whole tissue samples. Serial 3D allows for imaging of whole tissues in a more reasonable time scale (several days of acquisition at 2 pixel/s) but entails new challenges in sample preparation and data analysis. The realization of serial 3D IMS beyond a research laboratory curiosity depends on simple methods for reconstruction and interpretation of 3D IMS data, as well as determining which applications are best suited for the technology.

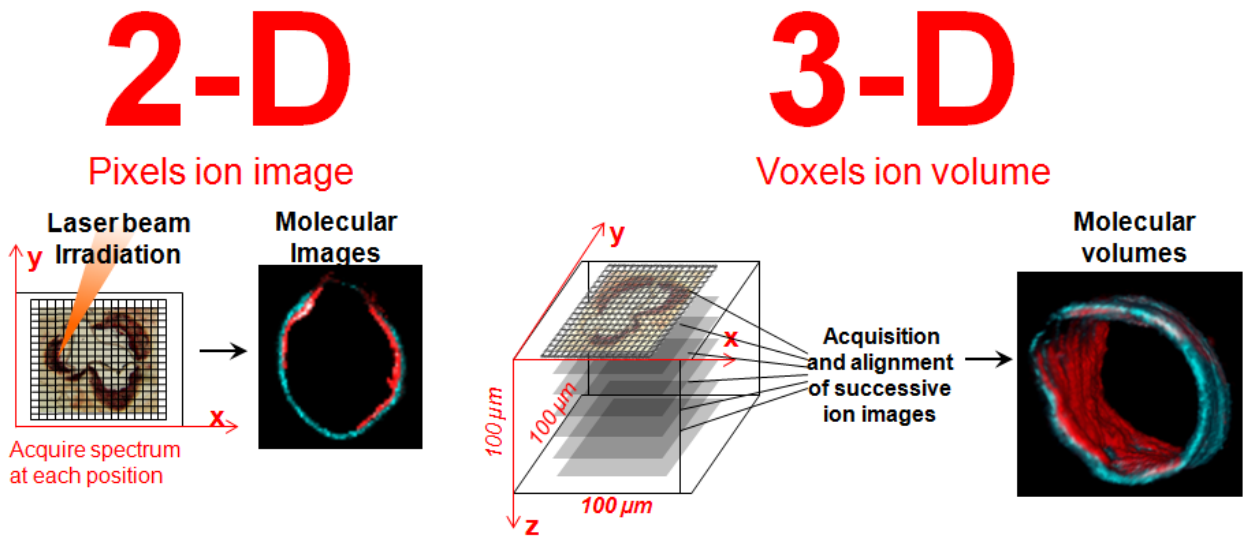


**Figure 1-14. Principle of going from 2D IMS to serial 3D IMS.**

To date, studies in 3D IMS have been largely technical with limited application in full scale, multi-sample studies due to preparation and analysis time. Microbial metabolite interactions in 3D have been studied[129] and biomolecules have been mapped out in normal[130] and diseased tissues.[131-133]The challenges have been in many cases logistic. There is only one commercially available software for analysis of 3D datasets and most studies in this discipline have required embedded bioinformatics expertise. Although many open-source and free software exist for IMS data analysis, none feature innate support for 3D IMS datasets. Besides this logistic challenge, a secondary challenge is in the interpretation of the data. In this vein, several IMS data analysis packages now exist[134-136] and their combination with software for microscopy analysis has been successful.[137,138] In serial 3D MS, the data analysis also includes the alignment of the data in 3D coordinate space. In order to keep the alignment true to the original morphology of the tissue, fiducial markers can be used for alignment. Use of an *in vivo* imaging technology is more appropriate for determining true morphology of a sample, but the tissue may be damaged in extraction from its source and lose its original morphology. Importantly, *in vivo* imaging common in medical practice provides an excellent correlation to serial 3D datasets in the case where

previously 3D imaged material is extracted for IMS, or in a mouse model where imaging can be performed before sacrifice.[139]

### 1.4.3 MALDI IMS data analysis in large datasets

Carrying out IMS studies of sections from multiple tissues requires validated workflows and analysis strategies. The datasets themselves are multivariate, and in many cases can be quite large in terms of disk space, especially if high mass resolution instruments are used. In comparison, computational analysis of histological staining data can be de-convoluted to three color channels (red, green, blue) for each pixel, whereas each IMS experiment will have thousands of mass channels over potentially thousands of spectra (pixels). To confront this challenge, and reduce manual inspection of IMS data, multivariate analysis of IMS data has proved useful.[140] Signals will likely co-localize and multivariate analysis algorithms are useful for finding this underlying structure or patterns to the data. The most well-known and widely-used algorithm is principal components analysis (PCA), which reduces the dimensionality of the multivariate data through derivation of so-called principal components individually describing a percentage of the data's total variance. Many similar algorithms exist and are useful.[140] Alongside component analysis, there is clustering analysis, which assigns spectra into groups according to the similarity of signals within the spectra. Clustering of the data has been termed "segmentation"[141] in IMS and many algorithms exist for this purpose.[140] They are very useful for visualizing the distinct molecular histologies of the dataset (i.e. tissue areas of similar molecular profile).[142]

Histology and pathology based on stained tissue sections is essential in IMS because it is already validated, widely used, and begins with the same sample type. The wealth of knowledge available about disease pathology from stained tissue sections is thus easily integrated into IMS studies. As such, IMS data analysis workflows almost always leverage histological data in interpreting MS chemical data.

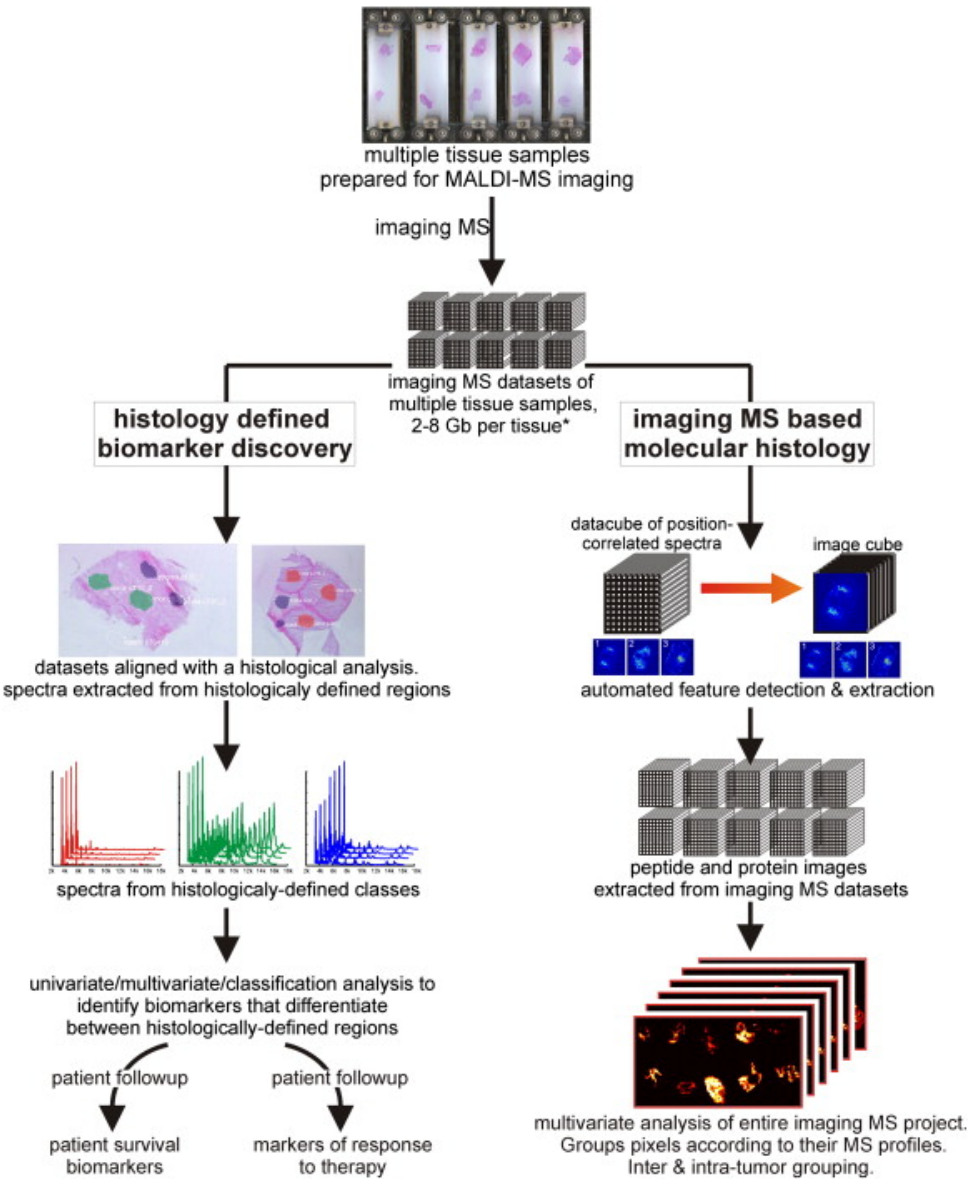


**Figure 1-15. Histology-driven and molecular histology IMS data analysis strategies.** *Left:* Histology-driven data analysis where ROIs are either pre-selected or selected for later analysis. *Right:* Molecular histology where unsupervised data analysis defines regions of interest. Figure from reference.[143]

The two major pathways to analysis in IMS of tissues are *histology-driven* and *molecular histology driven*. (**Figure 1-15**) Histology-driven data analysis determines regions of interest (ROIs) based on histological annotation of a stained section that has been previously imaged by

IMS, or is serial to the imaged section. The spectra underneath the annotated areas are collected and analyzed according to the annotation for discriminant species. This method is simple and rapid but may ignore the molecular differences that are not visualized in the histological staining, and being a supervised analysis, it requires outside expertise. Molecular histology driven approaches look at the inherit structure of the data through unsupervised multivariate analysis to determine common features across a cohort. At times these correlate with the staining data and sometimes they further segregate the samples. Molecular histology approaches require more computer power and data analysis expertise, but they give the most complete analysis of IMS data. Work in this field has proposed new data analysis algorithms[144] as well as work attempting to predict high-resolution IMS from lower resolution IMS data from fusion of staining and IMS data.[145]

The complexity of tissue histology creates challenges in data analysis. As an example, analysis of tumor samples with reduction into “normal” vs “tumor” is a simplistic model to tease out differences within a cohort of samples. However, this approach is ignorant of the diversity of tissue compartments in a cancer sample. There will likely be inflammation, fibrosis, and necrotic areas in tumor itself, and then the normal areas will have reaction to the tumor at the tumor normal interface. These histological distinctions are termed the tumor micro-environment and are increasingly studied in IMS analysis.[146] A histology driven approach may disregard such distinctions, whereas a molecular histology approach is likely to elucidate the tissue compartments through molecular features.

## 1.5 Research Objectives

The objective of this thesis was to develop methods to prepare and analyze complex, large lipid IMS datasets.

Often the tissue comes directly from a bio-bank or laboratory where animal models are produced. Because of this, collaborators must take special precaution in transferring samples.

Thin tissue sections destined for IMS have some unique considerations in this process; biomolecules will be imaged off the tissue surface, and the tissue surface is necessarily exposed during the transport. Chapter 2 of this thesis works towards characterization of lipid degradation markers and sample handling procedures that prevent lipid degradation.

In chapter 3 we address the need for data analysis strategies in 3D IMS. Large 3d datasets require not only high computing power, but strategies to implement all elements of the data without over-simplification. In this aim, we demonstrate an open-source methodology for 3D IMS data alignment, visualization and analysis.

In the case of 2D IMS data of a cohort of tumor samples, a reduction of datasets to two regions of normal vs tumor is too reductive to be definitive and excludes enormous amounts of information regularly integrated into a pathological analysis like the tumor microenvironment. With this in mind, we developed a strategy to analyze a large cohort of CRCLM sample that excludes none of the IMS data over a relatively large IMS cohort of 52 samples. We used our strategy to identify consistent regions across the sample with strong correlation to a battery of classic histological staining. Finally, our strategy extracts the signatures of the major histologies and uses these signatures and their presence to automatically classify the samples for clinical grading. This work addresses the need for developing independent IMS criteria for evaluation of clinical data, but starts from what is already validated through pathology.

## 1.5 Contents of this thesis

The second chapter of this thesis describes work on sample handling to prevent lipid degradation. The work describes markers of degradation, and means of preventing degradation.

The third chapter of this thesis presents our strategies for the analysis of 3D imaging datasets. The analysis included a total of 6 datasets from 3 samples, and addresses the challenge of

correlating analytical results from two different sample preparations in 3D. Our method of analysis was developed and scripts and example data are provided to increase accessibility.

The fourth chapter is work on developing strategies for the analysis of a large cohort of CRCLM samples by lipid IMS. The work is a middle way approach combining molecular histology provided by IMS to classical histology given in histological staining. We exploited the high correlation of segmentation of lipid data to histological staining to classify the regions of new samples and extract clinical information from the classification.

The fifth chapter of this thesis is the conclusion, highlighting the link between all the proceeding chapters and describing future perspectives on IMS.

# Chapter 2: Monitoring time-dependent degradation of phospholipids in sectioned tissues by MALDI imaging mass spectrometry

Nathan Heath Patterson, Aurélien Thomas and Pierre Chaurand

*Journal of Mass Spectrometry*, Volume 49, Issue 7, pages 622–627, July 2014

## 2.1 Abstract

Imaging Mass Spectrometry (IMS) is useful for visualizing the localization of phospholipids on biological tissue surfaces creating great opportunities for IMS in lipidomics investigations. With advancements in IMS of lipids there is a demand for large scale tissue studies necessitating stable, efficient and well-defined sample handling procedures. Our work within this article shows the effects of different storage conditions on the phospholipid composition of sectioned tissues from mouse organs. We have taken serial sections from mouse brain, kidney, and liver thaw mounted unto ITO coated glass slides and stored them under various conditions later analyzing them at fixed time points. A global decrease in phospholipid signal intensity is shown to occur and to be a function of time and temperature. Contrary to the global decrease, oxidized phospholipid and lysophospholipid species are found to increase within 2 h and 24 h, respectively, when kept at ambient room conditions. Imaging experiments reveal degradation products increase globally across the tissue. Degradation is shown to be inhibited by cold temperatures, with sample integrity maintained up to a week after storage in -80°C freezer under $N_2$ atmosphere. Overall, the results demonstrate a timeline of the effects of lipid degradation specific to sectioned tissues and provide several lipid species which can serve as markers of degradation. Importantly, the timeline demonstrates oxidative sample degradation begins appearing within the normal timescale of IMS sample preparation of lipids (i.e. 1-2 h) and that long term degradation is global. Taken together, these results strengthen the notion that standardized procedures are required for phospholipid IMS of large sample sets, or in studies where many serial sections are prepared together but analyzed over time such as in 3D IMS reconstruction experiments.

## 2.2 Introduction

Imaging Mass Spectrometry (IMS) by MALDI (MALDI IMS) is an innovative technique allowing simultaneous measurement of the abundance and location of multiple molecules within an area of fixed dimension [147]. MALDI IMS has already been applied to map several classes of biomolecules including proteins [148], peptides [149], metabolites [150], and lipids [151] on biological tissues. Within these classes of analytes, lipids are of increasing focus. Indeed, the ability of MS instruments to detect lipids has become part of the foundation of a new *–omics* field titled "lipidomics" [62]. Lipids are a class of molecules that have numerous biological roles including but not limited to forming and maintaining function of cell membranes, energy storage, and acting as chemical messengers. Many classes of lipids have already been identified by MALDI with the majority of IMS experiments centered on the analysis of the phospholipidodome due to its abundance on tissue surfaces and ease of ionization [152]. MALDI IMS analyses of phospholipids have been shown to provide direct correlation to tissue histology and measurement of localized molecular abundance with spatial resolutions down to 10 μm [153]. Highly reproducible and rapid matrix deposition by sublimation [85] and the option of dual negative/positive ionization acquisition over a single tissue section are other recent developments contributing to the analytical value of the phospholipid MALDI IMS experiment [89]. Alongside the advances in sample preparation mentioned above for lipid imaging, improvement in MALDI instrumentation has reduced sample acquisition time increasing the feasibility of larger scale studies [41,154,155]. Thanks to these front-end advancements, MALDI IMS of lipids allows exploration of diverse subjects such as mouse brain injury [156,157],cardiovascular disease [158,] polycystic kidney disease [159], and human skin lipids [160].

With large scale IMS studies of either many serial sections of a single tissue or sections coming from cohorts of different tissues, minimization of variation at key controllable points like matrix deposition, and instrument operational parameters needs to be routine to assure high quality

data. Despite these controls and data normalization approaches to ensure high quality display of data [161,162], there is to date little work concerning degradation and the lifetime of sectioned and mounted tissues over time. Already, protein degradation of sectioned and mounted tissues due to sample handling has been reported [163] and is mentioned frequently in method sections of IMS articles. Additionally, Richard Goodwin *et al.* have shown changes of several peptide biomarkers' abundances and localizations occur within minutes after sectioning unless proper care is taken [164]. For lipids, fatty acids being subject to time dependent heat degradation has been mentioned for analysis of latent fingermarks by MALDI IMS [165]. To our knowledge, very little data has been published with a view of global degradation of tissue sections in MALDI IMS experiments although the issue was recently highlighted in a review of sample preparation for MALDI IMS [166]. Sectioned tissues containing many preserved cellular components may have different and possibly unexpected molecular evolutions over time compared to cellular extractions such as the ones commonly used in lipidomics analysis by chromatography linked MS techniques. It is then of interest to define post-sectioning sample handling protocols that will give more accurate and reproducible lipid IMS results. This study therefore examines the time dependent changes of phospholipid composition on sectioned tissues by both positive and negative ionization modes.

In the aim stated previously, we have used mouse model organs including brain, kidney and liver to evaluate post sectioning changes of phospholipid composition and abundance over time under various storage conditions. Globally, our data have shown native lipid signals to decrease after only days if kept at ambient room conditions. Additionally the data presents phospholipid signals that increase in abundance shortly after sectioning, providing time-sensitive markers of degradation. Factors that affect these signal changes have equally been examined and sample storage methods that minimize degradation are proposed.

# 2.3 Experimental

## 2.3.1 Chemicals and Reagents

1,5-diaminonapthalene(DAN) matrix was purchased from Sigma-Aldrich (St. Louis, MO, USA).

## 2.3.2 Tissue sampling, sectioning and storage

Mice (15 days) were euthanized by $CO_2$ asphyxiation. After sacrifice, harvested organs were flash frozen by deposition on finely powdered dry ice in order to preserve the native tissue morphology. All animal studies were approved by the local Ethical Committee of the University of Montreal.

Mouse brain, kidney and liver tissues were sectioned for profiling and IMS analysis at 12 μm thickness and -15°C using a Leica CM3050 cryostat (Leica Microsystems GmbH, Wetzlar, Germany) and thaw-mounted on ITO coated glass slides (Delta Technologies, LTD, Loveland, CO, USA) according to previously published protocols [167]. Prior to sectioning, tissues were stored at -80°C. At the time of sectioning, tissues were removed from the -80°C and placed in the cryostat for 30 min at -20°C before sectioning. Immediately after mounting the sections, the slides were desiccated for 30 minutes. In all experimental conditions used, there were three technical replicates originating from serial sections. Following desiccation, slides were placed in their experimental storage conditions. In the case of 0-day samples, matrix was deposited and the samples analyzed the same day as sectioning. The effects of the following two conditions were examined: storage temperature and time of matrix deposition. Temperature was controlled at room temperature (~20°C), and deep freezer (-80°C). Tissues kept in freezing conditions were placed under $N_2$ gas in small plastic bags in order to avoid condensation on the tissue surface that may occur when removing the slices from cold storage.

### 2.3.3 MALDI matrix deposition

For IMS measurements, sublimation of DAN matrix was performed using a cold finger approach previously described [89]. Optimizations were performed by weighing the amount of matrix deposited on the slide, and correlating the subsequent results to the amount of matrix deposited.

### 2.3.4 MALDI mass spectrometry

Profiling and IMS of tissue sections were performed on a Bruker Daltoniks UltrafleXtreme MALDI-TOF/TOF mass spectrometer equipped with SmartBeam-II Nd:YAG/355 nm laser operating at a repetition rate of 1 KHz. Profiling and imaging data acquisitions were performed in reflectron geometry under optimized delayed extraction conditions, in a mass range of 480 to 1000 Da for positive, and 600 to 1800 Da for negative ionization modes, respectively. Instrumental parameters (delayed extraction parameters, laser fluence, detector gain) were set to obtain the best signal to noise ratio and remained constant throughout. For IMS data acquisitions, 100 shots were summed per array position with a spatial resolution of 125 µm. For imaging of mouse brain in all experiments, the positive and negative acquisitions were split along each brain section's horizontal bi-lateral symmetry with the left half used for positive, and the right for negative. A laser raster offset of 60 µm in both x- and y-axis was used for sequential positive and negative imaging of mouse kidney and liver as described by Thomas *et al* [89].

### 2.3.5 Data analysis

Data analysis was performed with MALDIquant [134], R, and FlexImaging 3.0. MALDIquant was used to perform peak picking with known matrix peaks manually removed from the generated peak lists. All data are compared relative to the corresponding 0-day data using the ratio of peak intensities and finally averaging all of the ratios to give a single value delineating global changes

in signal. Replicate samples were averaged to account for measurement error. Additional data analysis was performed in R.

For display, imaging data was loaded using FlexImaging 3.0 and a list of masses corresponding to peaks was created. The masses' intensities within the list were all scaled to the absolute intensity of the 0-day analysis, and the list was loaded into each individual imaging experiment. Gray scale ion images were then exported in .tiff format and manually realigned in ImageJ for easier comparison of the ion images between experiments.

## 2.3 Results and Discussion

We have developed a study of time-dependent changes of lipids by IMS with the goal of assessing the factors producing changes in signal and concurrently finding sample handling procedures minimizing such changes. This can be achieved by imaging serial sections held under different conditions for varying lengths of time. Ideally, changes in the native lipid composition due to major changes in tissue histology between serial sections should be smaller than those due to degradation.

### 2.3.1 Global decrease in lipid signal over time at room temperature

To determine the extent of degradation occurring on sectioned tissues, a mouse brain model was initially used. A set of signals from 0-day IMS experiments (sections analyzed as soon as possible after desiccation and matrix deposition) were compared to sections analyzed after multiple days at room temperature (20°C) and humidity with matrix being deposited the day of analysis. For all time points, 3 serial sections were analyzed. Peak picking using a signal-to-noise ratio of 3.0 was performed on the IMS datasets in positive and negative ionization mode resulting in 86 and 82 peaks, respectively.

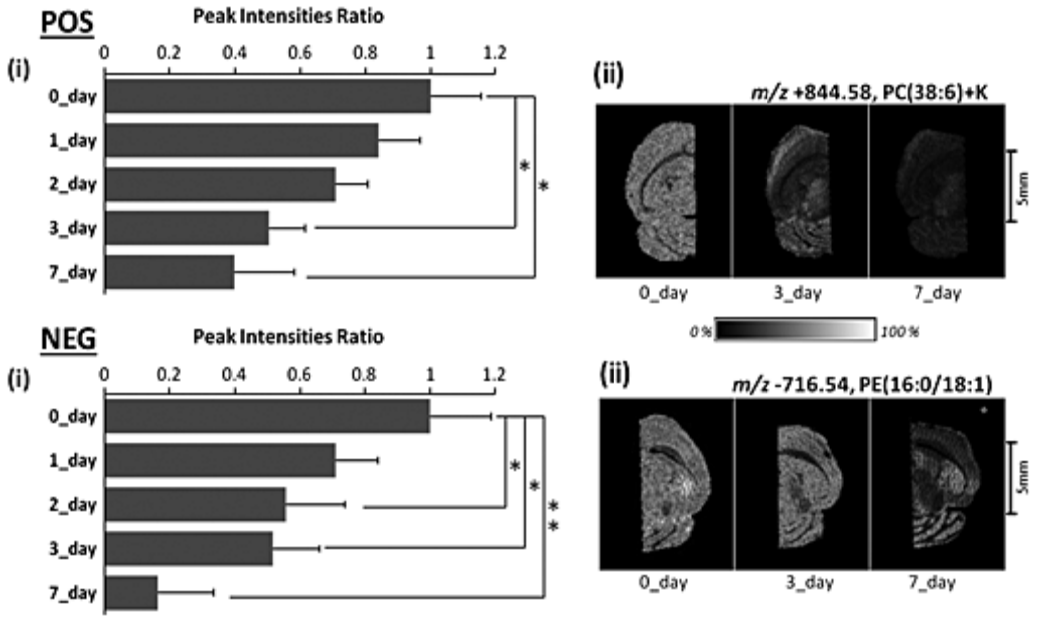


**Figure 2-1. Temporal changes of positive and negative lipid peak intensities with representative ion images.** Panel POS shows the data coming from positive ionization mode, while panel NEG shows the data coming from negative ionization mode. Section (i) graphs are comparisons of samples' total lipid signal intensity after storage at ambient room conditions for the indicated lengths of time (* = $p < 0.05$, ** = $p < 0.01$). Section (ii) displays representative ion images of horizontal mouse brain sections imaged at 125 μm of resolution scaled to the absolute intensity of the 0-day data.

**Figure 2-1** shows the global changes in signal intensity using the intensity ratio of picked peaks over time for positive mode-**Figure 2-1**-POS-(i) and negative mode-**Figure 2-1**-NEG-(i) with the data normalized to the 0-day intensity. Both modes showed loss of signal after a day of room temperature storage, however, these losses do not present a statistically significant difference at the 95 percent confidence interval with an n=3. At 3 days, positive and negative modes exhibited an average loss of 50% and 60%, respectively. At 7 days, positive mode signal abundance decreased by over 60% from the 0-day analysis, whereas negative mode finished the 7 day trial with a decrease of over 80% with respect to the 0-day signal abundance resulting

in many signals becoming indistinguishable from spectral noise. The total signal abundance was significantly lowered (* = $p < 0.05$, ** = $p < 0.01$) in both positive and negative ionization mode at the 3 and 7 day time points with $p< 0.05$ using a student's t-test. For negative analysis, the t-test resulted in $p < 0.05$ after only 2 days of storage and $p < 0.01$ after 7 days. **Figure 2-1**.A(ii) and B(ii) shows ion images scaled to the zero day intensity for representative phospholipids of each ionization mode. The ion images show that degradation seems to occur at different rates within the different histologies found in the sections. Both positive and negative mode show similar degradation, suggesting the phospholipid head group does not play a role in degradation. Representative ion images from mouse kidney and liver sections acquired under the same experimental conditions are shown in **Chapter 2 Supplemental Figure 1**, supporting the idea that such global degradation occurs independently of tissue type. These results indicate the sensitivity of sectioned tissues to their ambient conditions and the need for proper storage if samples are to be analyzed on different days. Particularly, lipids analyzed in negative mode are sensitive to degradation with results indicating almost a complete loss of analyzable phospholipid content after 7 days of room temperature storage.

## 2.3.2 Products of Degradation

As mentioned previously, tissues kept at ambient room conditions show significant decrease in global signal intensity at 3 days. However, certain signals were found to increase in intensity over time in the positive and negative mode contrary to global decreases. These signals can be separated into two groups based on lipid class and their respective rates of degradation: oxidized phospholipid (OxPCs) species and lysophoslipids (LPLs).

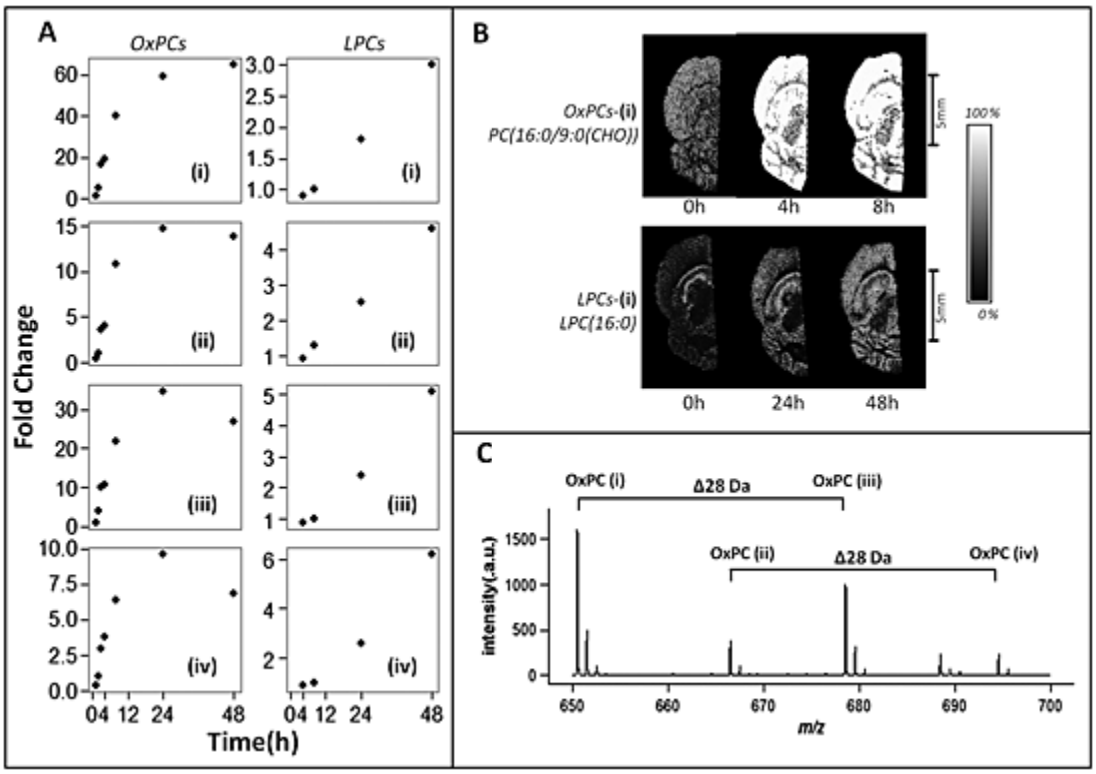


**Figure 2-2. Temporal changes of markers of phospholipid degradation in mouse brain tissue in positive ionization mode.** Panel A shows fold change over time of 4 representative oxidized phospholipids (OxPCs) (i= PC(16:0/9:0(CHO)), ii= PC(16:0/9:0(COOH)), iii=PC(16:0/11:0(CHO)), iv= PC(16:0/11:0(COOH))), and from lyso-phosphotidylcholines (LPCs) group (i=LPC(16:0), ii=LPC(18:0), iii=LPC(18:1), iv=LPC(18:1)+K) with n=3. Panel B shows ion images at 125 μm of resolution of the most intense member of each group the data is scaled to the absolute intensity of the 0-day data. Panel C shows a zoom on *m/z* 650-700 from a representative mass spectrum of the OxPC species with MS signals differing by 28 Da, or C2H4, indicating two saturated carbons difference.

The OxPC group, whose fold change versus time for 4 positive species (OxPCs) from mouse brain model is plotted in **Figure 2-2**-A-OxPC (i-iv), showed rapid increases even after 2 hours in ambient conditions with a short time scale study presenting a logarithmic increase in intensity reaching a plateau after one day of storage and then beginning to decrease. The fold change in

signal intensity reached 60x for the highest intensity signal at *m/z* +650.4 (**Figure 2-2**-A-OxPC (i), ion image displayed at **Figure 2-2**-B (i)). The fold changes of the OxPCs at *m/z* +650.4*,* +666.4, +678.4 and +694.4 are displayed in **Figure 2-2**-A-OxPCs (i-iv), respectively. The series are also related in intensity, the two peaks displayed in **Figure 2-2**-A-OxPCs (i& iii) show correlated increases in intensity. A similar correlation is observed between the peaks shown in **Figure 2-2**-A-OxPCs (ii & iv). The OxPCs also show a decrease after 2 days, possibly indicating their temporary nature. These signals formed two series of peaks where the individual members of each series are separated by 28 Da indicating a difference in the number of 2 saturated carbons on one of the lipid's fatty acid chains (**Figure 2-2**-C). OxPC signals were found to increase in kidney and liver as well (**Chapter 2 Supplemental Figure 2**). MALDI-TOF/TOF tandem MS analysis of fragmentation of the OxPC positive ions indicates a phosphotidylcholine head group but does not provide information about position of oxidation or chain length of the fatty acid (data not shown), however, a broad collection of studies on OxPCs strongly suggests the same series of masses as oxidation species when analyzed by ESI [168,169] or MALDI [127,170,171]. Additionally, the highly abundant positive species PC(34:0) at *m/z* 734.5 exhibited less decrease relative to the global average (**Chapter 2 Supplemental Figure 3**), possibly due to species' lack of an unsaturation. A similar resistance to loss is observed in the kidney and liver ion images in saturated phospholipids (**Chapter 2 Supplemental Figure 1**). Fragmentation spectra from negative ionization supports further the evidence of the OxPL group: with two signals, one at *m/z* -650.4 and another at *m/z* -664.4 representing the OxPL group (Supplemental Figure 4). The second signal at *m/z* -664.4 is particularly interesting as this same signal is detected in positive ionization (*m/z* +666.4, **Figure 2-2**-A-OxPC(ii)). The oxidized species found in negative mode were more useful as their MS/MS fragmentation patterns show that *m/z* -650.4 and *m/z* -664.4 are separated by the addition of an oxygen on the oxidized fatty acid chain. **Chapter 2 Supplemental Figure 4** shows the proposed structures and the pertinent fragmentations in negative mode of these two species.

The second group of degradation related signals, composed of 4 lyso-phophotidylcholines (LPCs) in positive mode using a mouse brain model, showed an increase of intensity in IMS data after a day at ambient conditions and continued to increase thereafter over the 2-day period measured (shown in **Figure 2-2**-B-LPCs (i-iv)). LPCs were identified using MS/MS and the Lipid MAPS database (**Chapter 2 Supplemental Figure 5**). Interestingly, LPCs do not show a decrease in signal after two days like OxPCs, but continue to increase.

These results present markers of degradation which can be seen to increase and plateau in a group wise manner despite global decreases over time. The OxPC group is of particular interest because its ability to diagnose sample degradation in both positive and negative ionization mode and its relative rapid increase in abundance after 1 hour. 1-2 h are typical time scales for IMS sample preparation and this result shows that even minor negligence can create unreliable results in lipid analysis. Due to their extremely low native abundance [172], a phenomenon we have observed in all tissues analyzed to date in our laboratory, any increase in this group of signals can indicate non-native changes have occurred in the model tissues. Extreme caution must be exercised if researchers wish to image native OxPLs as non-native increases in abundance can occur after only 1 hour of exposure in ambient conditions. Given the two OxPC series of peaks rise and fall in intensity together in positive ionization mode, it is possible to use the most intense signal of the two series, *m/z* +650.44 (**Figure 2-2**-A (i)), alone as an indicator of sample mishandling and degradation. LPLs require caution due to their native abundance in many organs, and their potential use as biomarkers [173]. Researcher should also be careful in assessing changes in this species between samples.

## 2.3.3 Preventing short term lipid degradation

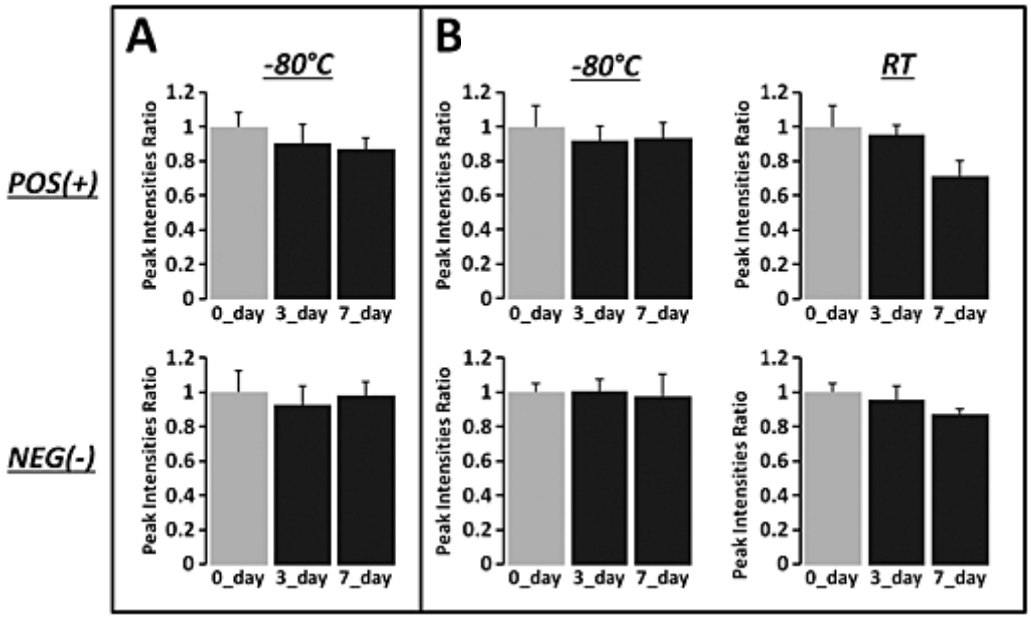


**Figure 2-3. Temporal changes of positive and negative ionization (marked POS(+) and NEG(-), respectively) phospholipid IMS global peak intensities with degradation inhibiting storage.** Panel A shows the changes in intensities from day of sectioning to sections cut and stored at -80°C for 3 and 7 days with matrix applied the day of IMS analysis. Panel B shows the same type of plots as panel A but the matrix was applied the day of tissue sectioning and sections were stored either at -80°C or room temperature (RT, ~20°C) for 3 and 7 days for comparison.

The effect of storage at -80°C and the timing of matrix deposition on degradation using a mouse brain model was explored over the period of a week using n=3 for all experiments. Our experiments included 3 sets of samples: sections stored at -80°C with matrix applied the day of analysis (**Figure 2-3**-A), sections stored at -80°C with matrix applied the day of sectioning (**Figure 2-3**-B, column -80°C), and sections stored at ambient conditions with matrix applied the day of sectioning (**Figure 2-3**-B, column RT). As expected, storage at -80°C was very effective in preventing degradation in both positive and negative ionization and prevented statistically

significant losses up to a week (**Figure 2-3**-A). These results compare favorably with the much longer term data recently published on human plasma lipid extract integrity [174]. Application of matrix the day of sectioning followed by storage at -80°C returned results negligibly different from simple -80°C storage after a week (**Figure 2-3**, -80°C column) in both ionization modes. Storage at ambient room conditions of tissue sections where the matrix had been applied the day of sectioning resulted in a 30% loss in signal occurring by day 7 in positive mode (**Figure 2-3**-B, RT column).

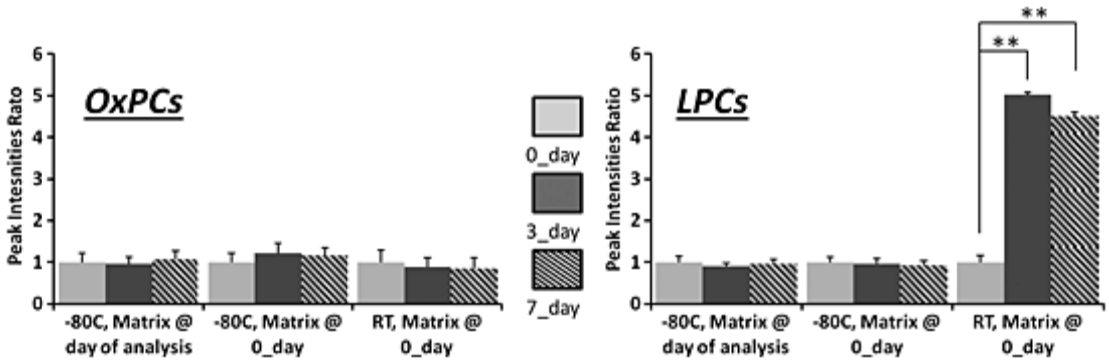


**Figure 2-4. Temporal changes of oxidized phosphotidylcholine (OxPCs) and lyso-phosphotidylcholine (LPCs) signals from mouse brain sections (n=3) stored under varying conditions.** The left plot of averages of the sum of OxPC signals in positive mode (PC(16:0/9:0(CHO)), PC(16:0/9:0(COOH)), PC(16:0/11:0(CHO)), PC(16:0/11:0(COOH))) from 3 time points, with different storage conditions of the tissues listed below. Here “Matrix @ 0_day” are samples where matrix was applied immediately after desiccation of the sample, before the sample was placed in the storage conditions tested. “Matrix @ day of analysis” is the condition where matrix was applied immediately before analysis. The right plot is the same but with the average of the sums intensities of 5 protonated LPCs (LPC(16:0), LPC(18:0), LPC(18:1), LPC(20:1), LPC(20:3)). The double asterisk (**) signifies a calculated p value < 0.01 using student’s t-test between the samples indicated by the bars.

Interestingly, this preparation and storage condition showed an increase in the abundance of LPC species after 3 days, but not in OxPC species (**Figure 2-4**). Considering this result along with the different rates of increase for the two degradation product groups mentioned in the previous section, it is possible that the mechanism producing these degradations is different. It is also possible that the DAN matrix acts as an anti-oxidant at the surface preventing phospholipid oxidation. The use of the hydroxyflavone class of anti-oxidants as a MALDI matrix was recently explored for lipid IMS analysis and was also noted as having the potential to prevent oxidative sample degradation [175]. Degradation of proteins can be in large part be prevented at the point of tissue procurement using the Denator system described by Goodwin *et al* [176]. Such a system may also prevent lipid hydrolysis of phospholipids to lysophospholipids by denaturing the enzymes responsible. This may allow researchers to be confident that observed differences in LPL signals are biologically relevant rather than sample handling artifacts.

## 2.4 Conclusions

We have used mouse tissue as models to highlight the role of storage conditions on the type and speed of phospholipid degradation after tissues have been cryo-sectioned and thin slices thaw mounted for MALDI IMS analysis. Our results show that temperature and atmosphere are the primary influence on phospholipid degradation. In the process of examining degradation we have found two groups of species, OxPLs and LPLs that can serve as markers of section or sample degradation. Additionally, we have demonstrated -80°C freezing of samples under $N_2$ as an effective means of sample preservation for up to at least a week. The demonstration that LPCs increase at room temperature storage even when there is matrix on the sample is also an important result for researchers who consider a tissue section finalized when the matrix has been applied. We further recommend applying matrix the day of sectioning before freezer storage as our results have shown that DAN matrix seems to prevent oxidation of phospholipids on tissues stored at room temperature. These results emphasize some current realities of

MALDI IMS and the need to fundamentally understand the behavior of cut sections to be used in biological IMS analysis. This is to say that sectioned tissues with many cellular components fully intact will have different and possibly unexpected molecular evolutions over time compared to cells, plasma extracts, or other biological samples that require extraction. This important difference between isolated cellular components in solution and intact components exposed as thin tissue sections necessitates the exploration of molecular degradation to ensure quality science is being performed. In this regard, relying on degradation behaviors observed for other types of lipid or protein analysis is not satisfactory in a scientific context. These expectations of sample integrity can be further pressed if IMS is performed on a (large) cohort of clinical samples, or if a study is performed on a single sample using many sections such as a 3D reconstruction. Our findings could also be of use in the field of food science as lipid degradation is known to produce unpleasant odors and tastes [177]. Future work could focus on long term cold storage to compliment the short term data presented here.

## 2.5 Acknowledgements

The authors would like to acknowledge Sebastien Gibb at the University of Leipzig for his help in implementing the MALDIquant R package. The authors would also like to acknowledge funding from the Canadian Foundation for Innovation and the Natural Sciences and Engineering Research Council of Canada. Dr. A. Thomas is recipient of a fellowship awarded by the Swiss National Science Foundation.

# Chapter 3: 3D Imaging Mass Spectrometry of Lipids in Atherosclerotic Plaques: Open-source Methods for Reconstruction and Analysis

Nathan Heath Patterson, Robert J Doonan, Stella S Daskalopoulou, Martin Dufresne, Sébastien Lenglet, Fabrizio Montecucco, Aurélien Thomas, Pierre Chaurand

*Proteomics*, **Accepted manuscript**, 2016

## 3.1 Abstract

3D matrix assisted laser desorption/Ionization imaging mass spectrometry (MALDI IMS) is a growing branch of IMS still requiring developments in methodology and technology to make the technique routinely accessible. Many challenges are simply a matter of producing 3D reconstructions and interpreting them in a timely fashion. In this aim and using analysis of lipids from atherosclerotic plaques from a human carotid and mouse aortic sinuses, we describe 3D reconstruction methods using open-source software that provides high quality visualization and rapid interpretation through multivariate segmentation of the 3D IMS data. Multiple datasets were generated for each sample and we provide insight into simple means to correlate the separate datasets.

## 3.2 Statement of importance

Atherosclerosis is a 3 dimensional biological phenomenon and in its study 3D imaging mass spectrometry (IMS) is an ideal approach to describe the development of the disease. This article demonstrates methods to analyse complex 3D IMS datasets with open-source software using mouse and human atherosclerosis samples. Additionally, we used several different IMS approaches, created multiple datasets per sample and describe methods to best correlate separated datasets in 3D. Finally, we demonstrate the strength of 3D IMS on a clinical human atherosclerosis plaque sampled in a carotid and outline the potential of the approach to further understand plaque formation and instability.

## 3.3 Introduction

Imaging mass spectrometry (IMS) has become a useful tool for tissue analysis.[29] IMS achieves imaging using the point-and-fire surface analysis technology of MALDI (Matrix Assisted Laser Desorption/Ionization), SIMS (Secondary Ion Mass Spectrometry) and other imaging compatible MS sources by acquiring spectra in regular arrays of fixed dimension.[178] Once spectra are acquired, maps of ion distribution can be plotted providing label-free, untargeted *in-situ* molecular detection. Integration of IMS of thin tissue sections into biomedical research has created opportunities in biomarker discovery, medical diagnostics, prognostics, and fundamental biological studies.[179]

3D-MALDI IMS is among the most promising applications of IMS technology.[180] 3D-MALDI IMS aligns serial 2D-MALDI IMS acquisitions from a single sample into a 3D volume.[137,181] Imaging of molecules throughout a whole tissue sample by reconstruction of consecutive 2D images can provide accurate localization on a truly anatomical scale; however, it entails challenges.[182] Among the challenges is serially sectioning the whole tissue with minimal error. The task is laborious and requires exceptionally careful manipulations. Formalin fixation paraffin embedding or use of other embedding media aids in sectioning but many fixation procedures remove small molecules, effectively eliminating some analytes from consideration.[56]

Alongside sample preparation, 3D data processing and analysis figure as important challenges.[183] The third dimension of 3D imaging data sets multiplies the complexity of 2D IMS data analysis, which is already complex due to its multivariate nature and large data size.[143] Currently, only one commercially available software exists capable of 3D reconstruction of IMS data (SCiLS GmbH, Germany).[184] However, researchers have repurposed many open source data analysis and 3D imaging softwares for 3D IMS with success.[182]

The fidelity of the 3D IMS reconstructions from serial sections is critical. In 3D reconstruction using cross-sections without outside morphological information, a curved object may be represented as straight due to unknown curvature during section alignment, dubbed the "banana" problem..[185] Consequently, morphologically accurate 3D reconstructions of 2D data will benefit immensely from correlation to other 3D imaging modalities. *In vivo* imaging provides the actual morphology of the imaged sample, and correlation to or, at best, registration of the IMS reconstruction data to the *in vivo* data generates the most accurate volumes. 3D IMS data has been demonstrated to correlate with *in* vivo and *ex vivo* MRI scans of whole tissues.[56,186] Given the increasing number of medical imaging platforms, one can expect a growing number of correlations between 3D IMS and other imaging techniques to give new insight into the molecular organization of tissues, organs and organisms.

3D IMS has thus far been implemented only in few in-depth biological studies due to the tedious sample preparation and extended imaging acquisition time required to generate a complete dataset.[133] However, acquisition time considerations may soon change in the case of 3D-MALDI IMS as high acquisition speed instrumentation becomes more widely available.[120,187] High-speed instrumentation will allow acquisition of a 3D-MALDI IMS dataset in a matter of hours or days rather than weeks and is expected to have a major impact on the advancement of the field, inspiring new applications. Alongside high speed IMS data acquisition, new sample types including 3D spheres of cultured cells or bacterial cultures will increase interest in 3D IMS.[188,189]

Cardiovascular disease (CVD) is the leading cause of death worldwide.[190,191] Atherosclerosis, a process that contributes significantly to CVD sequelae, is a chronic inflammatory condition, which results in the build-up of lipids, cells, and debris in the arterial wall, ultimately leading to plaque development and blockage of the arterial lumen.[192] It has severe clinical outcomes, which depend on the location of involvement; manifestations include angina or myocardial infarctions with coronary artery involvement, stroke with carotid or intra-cranial artery

involvement, peripheral arterial disease with arm or leg arterial involvement, and aneurysms in the aorta or other major vessels.[193] The tissue composition of plaques can reflect and contribute to the severity of disease and likelihood of further developing and causing symptoms, i.e. in cases of unstable plaques.[193] Therefore, applying advanced tissue characterization techniques can help unravel the biology of atherosclerosis. Indeed, IMS has been applied to atherosclerosis using SIMS imaging [194-197] and MALDI IMS.[198-200] A 3D reconstruction was performed using SIMS on a mouse heart.[130] Clinical studies of atherosclerotic plaques are possible because the tissue is often small enough that it can be 3D imaged in its entirety, and current medical practice allowing the surgical removal of the whole plaque from the arterial wall.

With IMS and 3D IMS of atherosclerosis on the cusp of major research development, we propose methods to effectively perform 3D IMS of lipids in atherosclerotic plaques. We report the use of open source software for the generation of 3D IMS reconstructions of atherosclerotic plaques from both mouse model animals and human clinical samples. We describe an effective strategy for generation of 3D reconstructions and rapid interpretation of the complex datasets. We identify the major areas of the imaged plaques through probabilistic clustering of the entire data set and highlight the 3D features by their component lipid signals. The methods described within this article highlight the potential of 3D IMS in describing atherosclerotic plaque development and progression as well as the viability and exciting possibilities of the technique in the study of human carotid clinical samples.

# 3.4 Materials and Methods

## 3.4.1 Tissue procuration

Two Apolipoprotein E-deficient ($ApoE^{-/-}$) male mice with 10 weeks of high cholesterol diet (1.25% cholesterol) were used in this study. For tissue harvest, mice were anaesthetized with ketamine-xylazine and after a cardiac puncture, hearts were rinsed with NaCl 0.9% and rapidly excised. All animal studies have been approved by the Swiss Federal Veterinarian Office and conform to the Guide for the Care and Use of Laboratory Animals published by the US National Institutes of Health.

One human carotid atherosclerotic specimen was obtained from a patient who underwent elective carotid endarterectomy for surgical removal of the carotid plaque at the Royal Victoria Hospital in Montreal, Canada. The whole specimen was acquired immediately after removal from the patient and rinsed several times in 4 °C phosphate buffered saline (PBS). It was placed in -40°C isopropyl alcohol to freeze, and then stored at -80°C until cryosectioning. The patient from whom the specimen was obtained was enrolled in an ongoing study at the McGill University Health Centre. Ethics approval has been granted from McGill University's Faculty of Medicine Institutional Review Board (A12-M145-09B), and the patient provided written informed consent.

## 3.4.2 Tissue preparation and cryosectionning of mouse hearts

The mouse hearts were received embedded in OCT. One heart was used for DAN analysis and another for silver-assisted LDI analysis. The entirety of the heart was sectioned from the bottom to the top of the heart (towards the aorta) at 10 µm. Prior to the aortic sinuses, 10 µm sections were kept at 40 µm intervals for OilRedO (ORO) staining. Once sectioning reached the aortic sinuses, three serial sections were taken for 1,5-diaminonapthalene (DAN) positive ionization

mode, DAN negative ionization mode and histological staining, or for silver assisted LDI and histological staining. 31 sections were acquired for positive and negative DAN MALDI IMS analysis, while silver assisted LDI IMS was performed on 64 sections. More details are available in the supplemental methods.

### 3.4.4 Tissue preparation and cryosectioning of human carotid

Fresh frozen carotid tissue was first embedded in OCT by placing a small amount of room-temperature OCT in a cubic container and then placing the frozen tissue in the OCT, and freezing the OCT at -20°C within the cryostat. In order to prevent cutting the tissue at an angle, attention was taken during the freezing of the OCT to maintain the tissue at a right angle to the bottom of the container. Once embedded, sections were cut at 10 µm in thickness with 100 µm between sections designated for IMS and were thaw-mounted onto slides for IMS. The tissue was cut in the direction of blood flow. Two sections were taken for IMS, 1 thaw-mounted onto an ITO slide for IMS using POS/NEG 1-5-diaminonapthalene (DAN) and 1 thaw-mounted onto a silver coated slide for silver assisted LDI. For DAN analysis, 133 sections were analyzed by MALDI IMS in positive and negative ionization modes, while silver-assisted LDI IMS was performed on 130 sections. More details are available in the supplemental methods.

### 3.4.5 1,5-DAN sublimation and silver deposition

The methods for DAN matrix sublimation [90] and silver sputtering [201] were followed as described elsewhere. Briefly, DAN was sublimated onto the sections after a 30 min desiccation of the slides at atmospheric pressure. The sublimation system was optimized for a coating of 0.1 mg per $cm^2$. A silver sputtering system was used for depositing a ~40 nm homogenous layer of atomic silver onto the sections designated for silver assisted LDI IMS.

### 3.4.6. MALDI IMS parameters

2D-TOF IMS of the mouse aortic sinuses sections was carried out with a spatial resolution of 40 μm using DAN and 30 μm using silver assisted LDI in reflectron mode using a Bruker Daltonics UltraFlextreme MALDI-TOF/TOF instrument. IMS of the human atherosclerotic plaque sample was acquired with a spatial resolution of 100 μm resolution in all imaging methods using the same instrument. The ion accelerating voltages, delayed extraction time, and laser fluence were optimized for the best S/N ratio in each acquisition method with only slight adjustments between sample plates made to laser fluence. The instrument's SmartBeam II laser was operated in "small" mode creating ablation sizes of approximately 30 μm with the given laser energy. For the human sample, DAN imaging was first performed in positive ionization mode at 100 μm, then offset by 50 μm in the x- and y- axis to acquire data in negative ionization mode. [90]

### 3.4.7. Histological Staining

The human carotid was stained with H&E after IMS acquisition. Mouse heart sections were stained by OilRedO (ORO), with serial sections stained at the aorta level. Stained slides were scanned at 20x magnification (0.454 μm pixel resolution).

### 3.4.8 Processing IMS data, statistical analysis, and imaging output

IMS data was first exported into the common imzML format using FlexImaging 4.1 (Bruker Daltonics,[122] then preprocessed and analyzed in R using Cardinal.[202] Pre-processing was limited to TIC normalization, and followed by peak picking of the spectra using a S/N threshold of 3, with a minimum appearance threshold of 5% for each peak in all spectra. In the carotid data, positive and negative datasets acquired through x-y position offset were merged into a single dataset. Lipids were identified by searching the mass in LIPIDMAPS database.[203] The reduced features were coerced into a data matrix containing the imaging depth, pixel coordinate and retained *m/z* values and their intensities for each pixel. Statistical analyses were performed in R,

using base R and Cardinal. Ion images of each retained *m/z* and statistical analysis outputs were exported as greyscale 8-bit tiff images organized by depth using a custom R script.

### 3.4.9 3D reconstruction of IMS data

Stained serial sections or imaged and stained sections were scanned and automated rigid body registration was performed with the StackReg plugin in ImageJ.[204] Fiji's TrakEm2 plugin was used to align the noise-excluded mask of the IMS area (detailed in results and discussion) to the computationally aligned histological staining.[205] These transformations were saved and applied to all ion images by parsing the TrakEm2 XML file into R and extracting the transformation matrix. Using R package EBImage [206], the transformations for each section were applied to every image previously exported.

## 3.5 Results and Discussion

The results presented herein concern atherosclerotic plaques found within a mouse heart aortic sinuses and a human carotid artery. In-depth discussion and details on the 3D reconstruction can be found in the **Chapter 3: Supplemental Methods Figure 1**along with a tutorial and accompanying R code.

### 3.5.1 3D IMS of atherosclerotic plaque in mouse heart aortic sinuses

#### 3.5.1.1 Localized phospholipid accumulation revealed by segmentation and correlation of separate positive and negative ionization datasets

Initial experiments were carried out using a mouse model of atherosclerosis where the plaque was induced by knockout of the ApoE gene and a high cholesterol diet. Segmentation was used to explore the molecular histology of the plaque across multiple IMS modalities (silver-assisted

LDI, DAN positive and negative ionization mode imaging). Multivariate clustering or segmentation of the IMS data are a powerful aid in determining molecular histology as well as identifying non-relevant regions, dominated by matrix clusters or embedding polymer peaks. Spatially aware shrunken centroids is a segmentation algorithm featured in the Cardinal R package that clusters IMS data, while accounting for the image's coordinate space and also estimates the probability of each coordinate belonging to each cluster. The probabilities are helpful with imaging pixels, which lie on the border of two distinct molecular histologies.

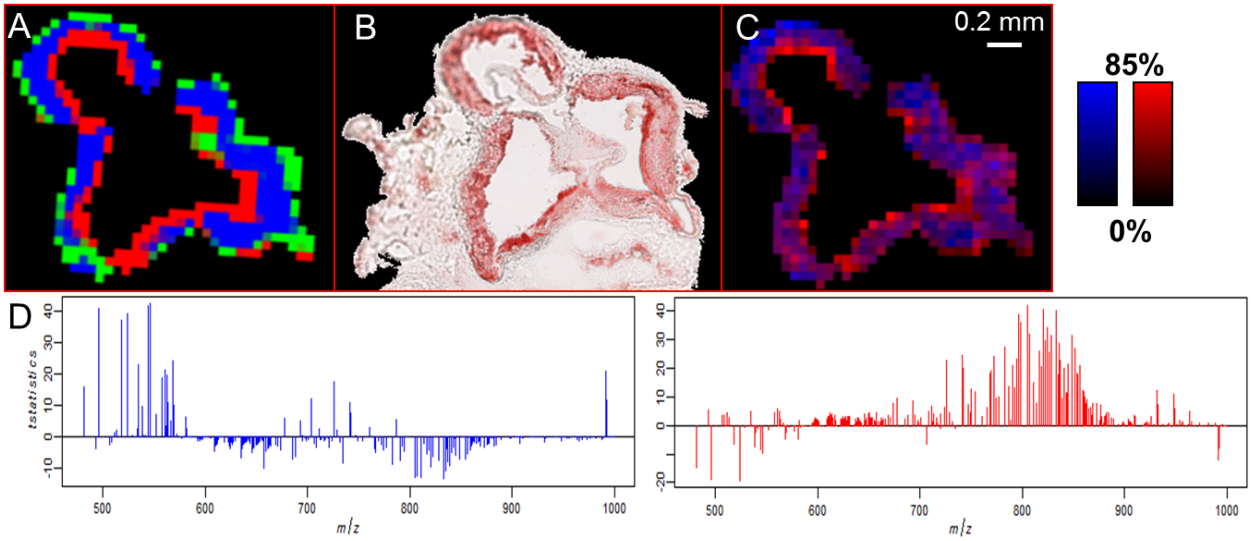


**Figure 3-1. Mouse heart aortic sinus reconstruction using positive ion mode IMS data.** A: Spatially aware shrunken centroids clustering segmentation (k=4) image from 3D at the middle point of the plaque. B: Corresponding ORO staining of the plaque area. C: Ion images of the top two markers as defined by the t-statistics of the clustering, in blue, LPC(16:0), *m/z* 496.3 and in red, 804.55, PC(16:0/20:4). D: T-statistics of the clustering analysis indicating correlation (positive values), or inverse correlation (negative values) for the red and blue clusters.

The DAN 3D reconstructions were done using 31 sections for a total length of 0.124 cm. Supplemental video 1 shows the mouse aortic sinuses data from the DAN analysis in positive ionization mode reconstructed in 3D, with **Figure 3-1** A-B along with the corresponding ORO

staining for a section chosen from the middle of the plaque. Within this data set, the entire tissue section was not imaged as it was primarily adjacent heart tissue and the plaque was the target of the experiment. Because the plaque area is obscured after matrix deposition, it was necessary to make a general selection of the region, including some heart tissue and the interior of the aortic sinuses.

**Chapter 3: Supplemental Figure 1** contains the segmentation data for aortic sinuses in positive and negative mode. Supplemental videos 1 and 2 contain a rotation of the 3D reconstruction of the plaque from positive and negative ionization mode analyses. The color-coding for the k=3 segmentation in **Figure 3-1**-A and Supplemental Figure 1 was chosen to best represent the regional correlations between positive and negative mode observed after registration to the ORO staining. Three segmentations were sufficient in describing the plaque area; clustering groupings did not reveal distinct molecular regions, but rather areas of similar molecular composition but with only moderate intensity differences. In **Figure 3-1**-A-B, three regions of the artery from positive mode data are displayed, the largest plaque region being colored in blue, an interior region colored in red, and an outer region in green. In this case, the segmentation colored in red was often found along the inner wall of the aortic sinuses and associated with a deep red ORO coloration (**Chapter 3: Supplemental Figure 1**, sample 10), while the other less deeply ORO stained areas are colored by blue and green. The loadings of segmentation for the red and blue are shown in Figure 1E, where a positive value indicates association and negative values inverse correlation. The positive mode indicated that the bulk of the plaque, highlighted in blue is associated with the lyso-phosphatidylcholines (LPCs). LPCs' numerous roles in atherosclerosis have been studied and are beyond the scope of this article.[207] They are the primary lipid component of oxidized low-density lipoprotein, a precursor to macrophage and foam cells contributing to proliferating inflammation in plaques.[208] The plaque interior wall was indicated by several PC species, with the top species being PC(16:0/20:4) at

*m/z* 804.5 and PC(18:0/20:4) at *m/z* 832.5, previously identified to be related to smooth muscle cells (SMCs) in both human and mouse atherosclerosis samples.[198] **Figure 3-1**-D visualizes LPC(16:0) and PC(16:0/20:4) from a single section, confirming the species localization. The SMC associated PC was more highly-correlated with the strongly ORO staining region of the plaque, rather than in the area of abundant LPC, where a "lipid-core" is typically found and one would expect to find strong ORO staining. This may indicate an early-stage plaque where lipids from inflammatory cell invasion are accumulating and disrupting the intima (inner-region) for deposition in such a lipid core.

#### 3.5.1.2 Silver-assisted LDI IMS detects differential localization of free fatty acids, cholesterol / cholesterol esters, and triglycerides

Silver-assisted LDI is an IMS technique that generates silver adducted ions of free fatty acids, cholesterol, cholesterol esters and triglycerides. The 3D reconstruction was done using 31 sections for a total length of 0.093 cm. Like the data from DAN, segmentation of the silver-assisted LDI data revealed signals associated with different areas of the plaque (**Chapter 3: Supplemental Figure 2**). Within the strongly stained ORO regions, free fatty acids (FFAs) arachidonic acid, oleic acid, and docosahexaenoic acid were abundant (Red segmentation, Supplemental Figures 2 & 3). These FFAs all contain 1 or multiple unsaturations on the fatty acids (FA) chain and this is thought to be the point of silver chelation and ionization as saturated chains are only marginally detected. The blue segmentation in **Chapter 3: Supplemental Figure 2** shows the rest of the plaque area where these FFAs were also present, but to a lesser degree. The blue segmentation is multivariately distinct, but lacks individual highly expressed species. ORO stained plaque area's signal was homogenous and the FFAs showed localization as a group rather than distinct localization by species.

The plaque contains distinct regions of high cholesterol signal abundance that are not co-localized with the free fatty acids. Examination of the cholesterol containing segmentation's t-

statistics (Supplemental Figure 3, green segmentation) revealed the presence of C18:1, C20:4, and C22:6 cholesterol esters (CEs) adducted by silver alongside silver-adducted cholesterol.

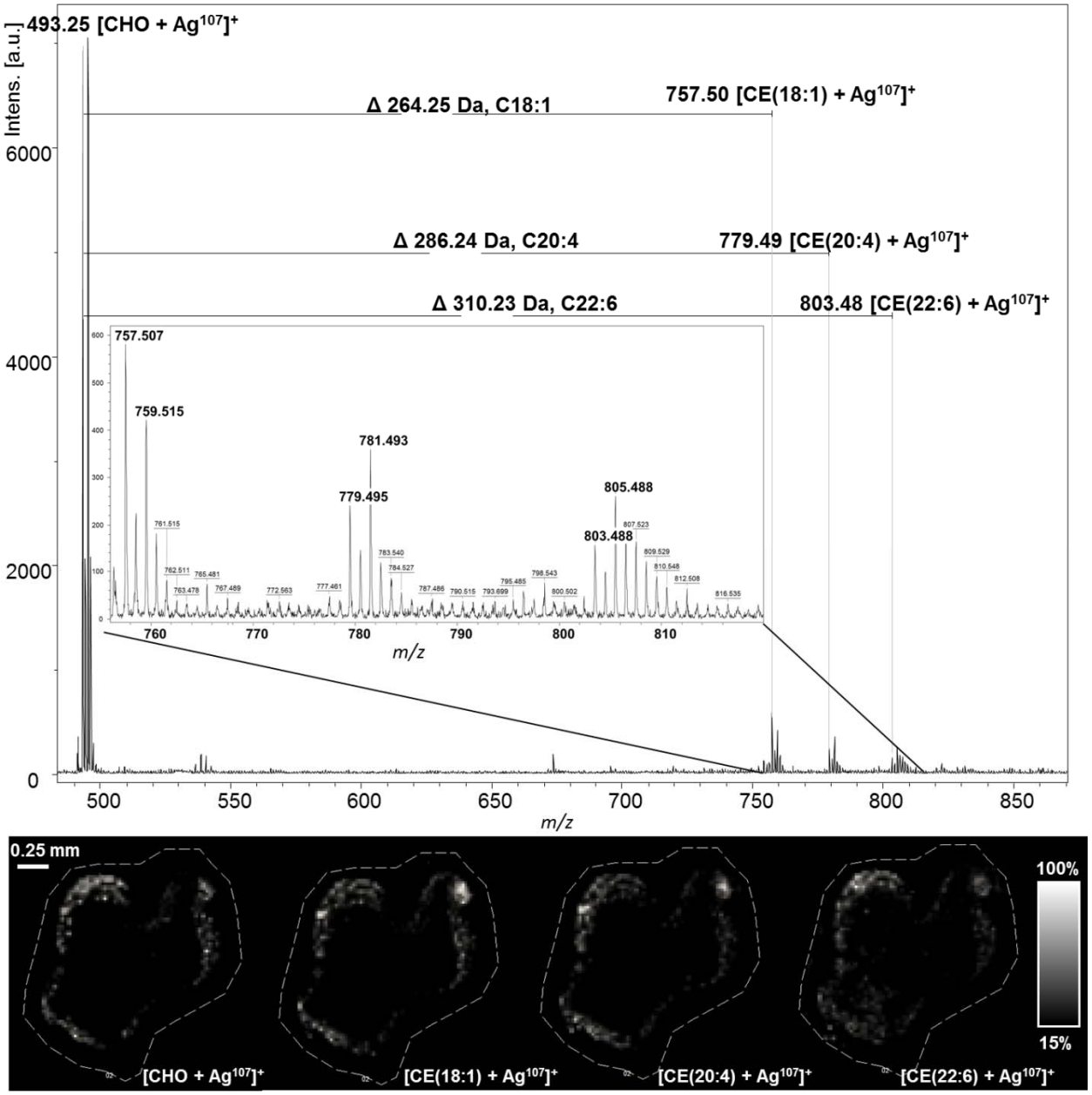


**Figure 3-2. Cholesteryl esters in mouse heart aortic sinuses detected by silver-assisted LDI IMS.** Representative spectrum on top shows the change in mass between silver adducted cholesterol and cholesteryl esters (CE), with a zoom of the CE region. Below are ion images from one of the 3D sections showing the co-localization of cholesterol and CEs.

**Figure 3-2** shows annotated representative spectrum from the cholesterol rich region alongside ion images of the CEs detected. The ion images show the co-localization of the CEs and cholesterol, with CE (22:6) showing some polymer artifacts due to its low abundance and a coinciding polymer ion at *m/z* 803.5. Silver ionization generates Ag107 and Ag109 adducted ions separated 2.003 Da, leading to signal convolution of lipids where FAs may contain 0 to 6 unsaturations (two hydrogens: 2.015 Da). Such an effect is visible for the detected CEs in **Figure 3-2**, CE(20:4) at 779.495 which is next to a species at 781.493. If CE(20:4) was isolated, one would expect that the isotope ratio of the species would follow the Ag107 to Ag109 isotope ratio of ~100/92%, however, this set of peaks also likely contains CE(20:3), detected at *m/z* 781.5. With high mass resolving power this problem can be mitigated. The detected CEs contained fatty acid chains also found as FFAs by IMS and may not indicate all of the esters that are co-localized in the plaque as the CEs with saturated FAs may be poorly ionized by silver assisted LDI. Indeed, we do not detect CEs with C16:0, but they are presumed to exist and have been detected elsewhere.[196] Regardless, CEs are important blood markers of heart disease, and their presence gives clues to the biology underlying the plaque's formation and thus may be more promising than the ubiquitous cholesterol as an IMS marker. ToF-SIMS imaging identified the ratio of CE(16:0) to CE(18:1) to be an important dynamic in atherosclerotic progression.[196] Our results contain several co-localized CE species, but CE(16:0) is not detected for comparison.

Finally, the aortic valve cusps were detected by the presence of sodiated adducts of triglycerides (TAGs) at some tissue depths (**Chapter 3: Supplemental Figure 3**, yellow segmentation). This histology was difficult to consistently detect and is not visible throughout the reconstruction owing to its small size and position within interior of the aortic sinuses exposed to OCT. Although the TAG ions were not unique to the cusps, their presence on the cusps may be

indicative of atherosclerotic progression. Again, a ToF-SIMS analysis reported similar results in that they found no co-localization of cholesterol and TAGs in atherosclerotic plaques.[197]

## 3.5.2 3D IMS of atherosclerotic plaque in a human carotid artery

### 3.5.2.1 Segmentation of dataset reveals 3D localization of molecular histologies correlated to the degree of artery stenosis

The human carotid used in this study was surgically excised and thus contains a cut along the plaque. Due to this limitation, accurate representation of the plaque as would be seen *in vivo* cannot be obtained, especially considering that the cut edge is more easily deformed during sample removal, freezing or embedding. However, in the case of this sample, the incision was at the superior portion of the artery and the bulk of the plaque was in the inferior aspect of the artery and therefore, was relatively undisturbed. It is important to understand that such limitations will arise in 3D reconstructions of human tissue since the entire artery cannot be recovered. We stained the imaged sections with H&E over ORO because the human plaques are more varied and complex and H&E provides a better overview of the histology compared to ORO where only neutral lipids are stained. ORO was sufficient for the mouse model where plaque is less variable.

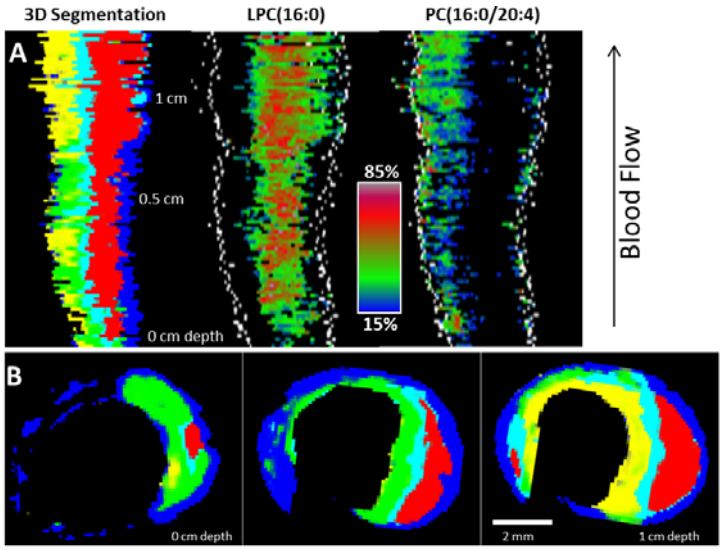


**Figure 3-3. Longitudinal view of 3D IMS reconstructed human carotid atherosclerotic plaque.** A: 3D longitudinal view at the plaque's center. 3D ion volumes from the same depth plane distinguishing the yellow and red segments. B: 2D segment images from increasing depth in the plaque showing the evolution of the molecular histology with increasing stenosis.

The major regions of the bulk and non-cut area of the plaque are outlined by spatial shrunken centroids segmentation in **Figure 3-3**-A as a longitudinal view. The DAN 3D reconstruction was done using 118 plaque containing sections for a total length of 1.18 cm. Supplemental video 3 contains rotations of the 3D segmentation of the plaque. There are several areas of interest in the plaque: inner portion of the plaque (typically intima and fibrous cap - yellow, green segments), middle plaque region (heterogeneous mix of cell types and lipid core - red, cyan segmentations) and outer plaque region (primarily connective tissue - blue) observed in both a 3D cross section and at increasing depth in 2D.

Interestingly, the segmentation revealed that these major arterial features diverge molecularly depending on depth and total composition of the individual segments. The inner plaque region's segmentation changes from the green to yellow segment as the stenosis increases (**Figure 3-3**-A, segmentation). The negative and positive t-statistics are available in **Chapter 3:**

**Supplemental Figure 4** & **Chapter 3: Supplemental Figure 5** and provide the important signals of each region. The molecular change is due to the species previously associated to SMCs and seen at the intima of the mouse species, again, PC(16:0/20:4) and PC(18:0/20:4). This result may suggest a proliferation of SMCs in this plaque as stenosis increases. Additionally, the prescence of the arachadonic acid containin PCs outside of the plaque interior may point to a lack of degradative inflammation in this area. This fits as well with The red and cyan segments are the primary contributing molecular histologies to increased stenosis with the plaque intima area increasing less significantly. The red and cyan segments have similar molecular composition, with the red having a higher abundance of protonated LPCs and the cyan segment containing LPCs with higher abundance of sodium and potassium adducts. The plaques outer connective tissue (blue segmentation) does not vary molecularly with 3D location on the plaque. **Figure 3-3**-A shows the LPC(16:0) compared to the longitudinal view of the segmentation. The 3rd dimension gives a clue about plaque formation, as greater stenosis is a known risk factor for plaque rupture and thus for stroke [209], and the more stenotic area of the plaque contains regions pooled with LPC. Negative mode data showed abundance of ceramide species (Cer-1-Phosphate at *m/z* 616.4 and phosphoethanolamine (PE)-ceramides *m/z* 687.6 and 685.6) in the bulk plaque area, co-localized with LPCs.

### 3.5.2.2 Registration of IMS to H&E increases efficiency and accuracy of analysis

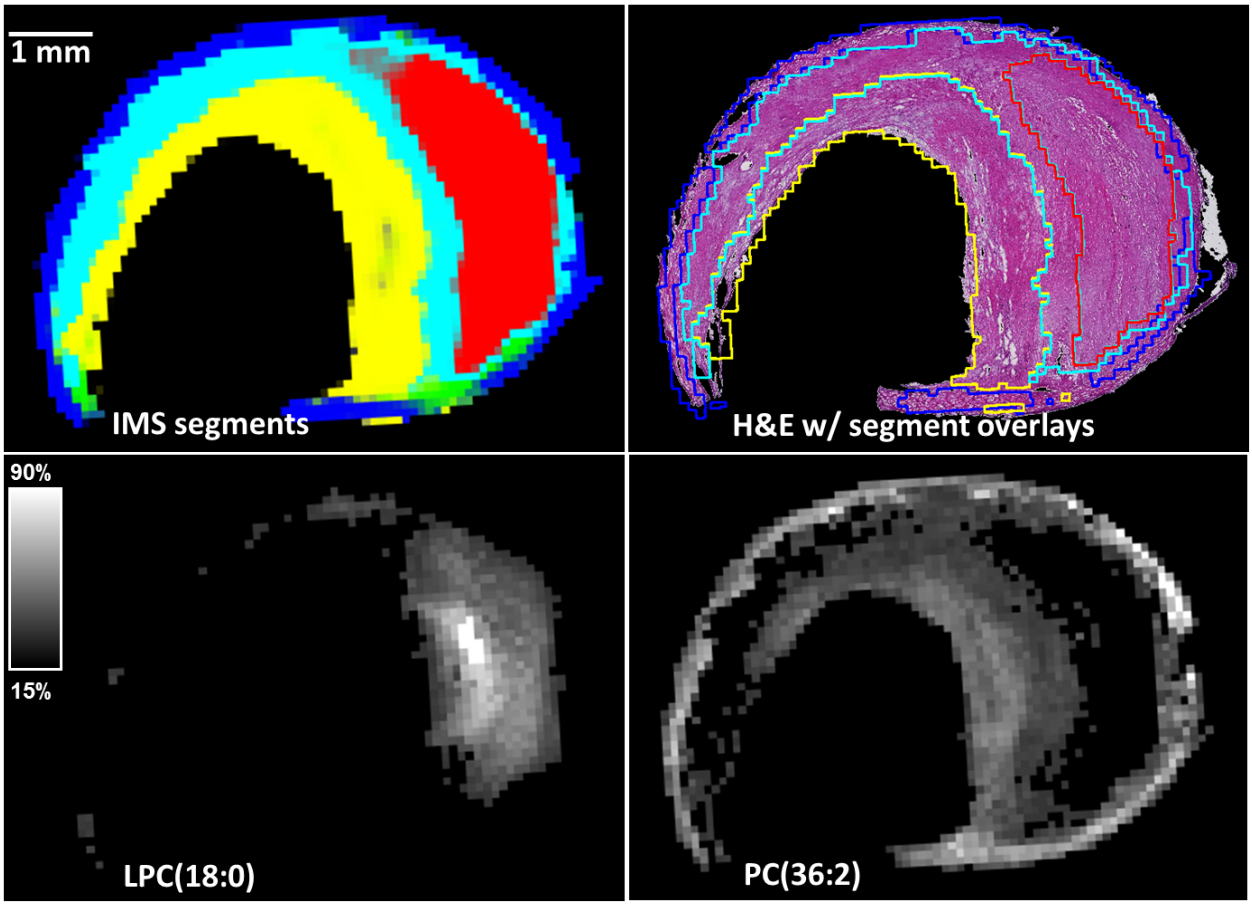


**Figure 3-4. Segmentation of optical data by molecular histology.** Top-left: IMS segmentation as previously described. Top-Right: Overlay of H&E with the IMS segment data, highlighting correlation between molecular information and histology. Bottom: Ion images associated with the red and blue segmentation, left and right, respectively.

In collaborative efforts involving IMS, dissemination of IMS data in a format that is pertinent and interpretable by clinicians and collaborators with less familiarity with the technology is important. In the case of co-registered 3D IMS and 3D histological data, the advantage is segmentation of the optical data according to the molecular histology, as shown in Figure 4 where the optical data section are dissected by the IMS regions. The classic histological approach is used in determining histological correlation and validating molecular histology with experts. Dissecting

optical data by molecular histology is an automated manner to reveal where the IMS data and staining data are congruent and is particularly powerful in 3D applications as the amount of digital pathology data increases with the IMS data. There are limitations as the low resolution IMS data's segmentation does not describe well border regions but the bulk of an area is quickly displayable and interpretable. Examination of the IMS segmented H&E data over the entire 3D reconstruction revealed that the plaque is predominantly fibrous in character, indicating a better prognosis [210]. As previously indicated, the yellow segmentation describes areas rich in fibrous tissue and SMCs (**Figure 3-4**), while the outer blue area is predominantly composed of connective tissue. **Figure 3-4** shows two ion images from lipid species highly correlated to the bulk plaque area (left and right ion images, respectively). Careful examination of the ion images also reveals that individual ion intensity can depend on the density of certain histology as shown in LPC (16:0) where the most saturated pixels are correlated with a more eosin rich and dense fibrotic area (H&E available in **Chapter 3: Supplemental Figure 6**). Another useful aspect of IMS data registered to staining data in the context of 3D IMS is confirmation of the tissue structure by 3D reconstruction of the H&E staining as shown in Supplemental Videos 4 & 5.

Silver-assisted IMS did not provide interesting results in 3D as there was very limited signal intensity throughout the plaque. This is likely due to the fibrotic nature of plaque. The unaligned 3D segmentation data is given in **Chapter 3: Supplemental Figure 7**. The data did show some association of FAs with the plaque area highlighted in cyan in the DAN data, but oftentimes a complete depletion of signal in the bulk plaque area (red segment in DAN) is noted.

### 3.5.3.2 3D IMS has unique potential in atherosclerosis research

The results shown above demonstrate that mouse models of atherosclerosis and human samples contain similar molecular histology at the lipid level and at the 3D spatial level. Here we have demonstrated the capability of our techniques to identify molecular histologies in mouse models as well as a human carotid plaque. These techniques should be further applied in

different types of human plaques with different tissue composition and instability level. Indeed, it is well known that plaque morphology is heterogenous between patients and that particular histological features are considered to be higher risk, leading to rupture, and clinical symptoms, e.g. stroke [210-212]. It would be interesting to determine if molecular histologies and their 3D spatial organization, obtained from the IMS techniques used herein, can predict high-risk features, and particularly identify areas of plaque that have higher-risk of rupture. These investigations would help further unravel the biological complexities of atherosclerosis, and predict clinical outcomes. Furthermore, it could also help identify treatment efficacy in stabilizing atherosclerotic plaques.

## 3.6 Concluding Remarks

3D IMS is a developing field that requires both front end and back end method development, but another important consideration is what types of studies best leverage the technology. The suitability of the human carotid for 3D IMS is demonstrated as this tissue has characteristics favorable to 3D IMS including its size and the surgical excision that involves removing the entire plaque. The latter is particularly important as a primary advantage of 3D IMS is to describe a system in its 3D entirety and mitigate concerns about the representativeness of the sample.

We have presented a method for 3D reconstruction of IMS data that is robust and uses open source software. We apply the reconstruction method to atherosclerosis, a 3D biological phenomenon. We demonstrate the power of 3D using both mouse model and human carotid atherosclerosis tissue. In both cases, we acquire multiple datasets for the plaque and detail methods for comparing the datasets. Although this study is limited to a small number of samples, correlations are demonstrated from the mouse model to the human tissue. The methods developed on mouse tissue scaled up to more complex human tissue and proved their effectiveness across sample preparations and tissue type. Numerous interesting applications for

these methods in the future may help further unravel the biological complexities of atherosclerosis.

## 3.7 Acknowledgements

NHP, MD, AT and PC acknowledge funding from the Natural Sciences and Engineering Research Council of Canada and from the Canadian Foundation for Innovation. RJD is supported by a Canadian Institutes of Health Research (CIHR) MD-PhD Studentship, a CIHR Doctoral Award, and a McGill University Systems Biology Training Program Studentship. SSD (Chercheur-Boursier Clinicien) is supported by the Fonds de recherche du Québec – Santé (FRQS). The authors also acknowledge JF Masson (Université de Montréal) for the gracious use of his metal sputtering system. The funding sources had no involvement in the study or decision to submit the manuscript for publication.

# Chapter 4: Automated Assessment of Colorectal Cancer Liver Metastasis Modified Tumor Regression Grade (mTRG) by Lipid Imaging Mass Spectrometry

Nathan Heath Patterson, Balqis Alabdulkarim, Anthoula Lazaris, Aurélien Thomas, Martin M. Marcinkiewicz, Zu-hua Gao, Peter B. Vermeulen, Pierre Chaurand and Peter Metrakos

*Nature Medicine,* **In submission**, 2016

# 4. 1 Abstract:

In many cancers, the establishment of a patient's future treatment regime often relies on histopathological assessment of tumor tissue specimens in order to determine the extent of the 'pathological response' to a given therapy. However, histopathological assessment of pathological response remains subjective. Here we use MALDI imaging mass spectrometry to generate lipid signatures from colorectal cancer liver metastasis specimens resected from patients preoperatively treated with chemotherapy. Using these signatures we obtained a quantitative and objective pathological response score that correlates with prognosis. In addition, we identify single lipid moieties that are unique to different histopathological features of the tumor, which have potential as new biomarkers for assessing response to therapy. These data show that automated and objective methods, focusing on the lipidome, can be used as prognostic markers for response to chemotherapy which will improve risk assessment and patient care.

## 4.2 Introduction:

Many solid tumors (colon cancer, breast cancer, gastric cancer, oesophageal cancer etc.) receive neoadjuvant chemotherapy prior to resection and the prognosis of the patient as well as the adjuvant therapeutic strategy is determined by the pathologic response to the neoadjuvant regime. Thus, the development of objective and quantitative strategies to evaluate pathologic response is important in many solid tumors.

Despite advances in management of colorectal cancer liver metastasis (CRCLM) patients, the majority are incurable.[213-215] Surgical resection is the only chance for cure but only feasible in 15-20% of patients.[216,217] Various clinical parameters such as the number and size of lesions, disease free interval, and serum Carcinoembryonic antigen levels, among others have been used to prognosticate these patients. However, with modern day therapies including preoperative chemotherapy and loco-regional modalities, these factors no longer correlate effectively with post-operative disease free and overall survival rates.[218-221] Similarly, clinical scoring systems that utilize these parameters are no longer appropriate, in that even patients with a poor clinical risk score that have a good response to neoadjuvant chemotherapy will have a better outcome than the clinical risk score would have predicted.[222,223] There are only a few molecular biomarkers that can predict prognosis and guide treatment. [224,225] These include KRAS that is used to select patients for treatment with anti-EGFR agents and microsatellite instability that is a prognostic factor and a marker for response to 5-FU.[226,227]

Pathological evaluation can predict patient outcome by assessing response to preoperative chemotherapy but can also evaluate surrounding unaffected liver parenchyma for chemotherapy associated toxicity that could lead to morbidity, further driving the choice of future chemotherapy and patient management.[228,229] Pathological grading systems have been developed to address this with variable correlation with survival.[230-234] Early post chemotherapy grading systems

looked at percent viable tumor cells and more recently the Tumor Regression Grade (TRG) [21] demonstrates a correlation with patient outcomes. This grading takes into consideration the degree of fibrosis and necrosis in relation to tumor viability, in which fibrosis is considered a positive indicator and necrosis a negative indicator of response.[232] However with the widespread use of Bevacizumab, an angiogenesis inhibitor precipitating tumor necrosis as a form of response, the Modified Tumor Regression Grade (mTRG) emerged.[235] mTRG differentiates between two types of necrosis seen in resection specimens; usual necrosis (UN), typical of tumor progression, and infarct-like necrosis (ILN), a response to treatment, whose presence has been associated with favourable prognosis.[235] However, the pathological evaluation process remains a subjective semi-quantitative one regardless of which grading system is applied and is subsequently vulnerable to inter-pathologist variability necessitating a complementary technical approach[236,237]. In addition, the final pathological report can take between 7-14 days, depending on the institution.

We propose to compliment pathologic assessment of CRCLMs with Matrix-assisted laser desorption/ionization (MALDI) imaging mass spectrometry (IMS). IMS images biomolecules including proteins and lipids directly on thin tissue sections of clinical origin maintaining spatial orientation.[29,100,147,178] IMS acquires mass spectra at defined 2-D positions across a surface and reconstructs these data into ion distribution maps reflecting molecular distributions.[179,238] Phospholipids are of clinical interest due to their biological roles in both physiological states and cancer processes.[90] The potential clinical utility of phospholipid IMS has been demonstrated in a number of applications[90,239-241], however, tissue studies with large cohorts still require robust and validated approaches for data interpretation due to the highly multivariate nature of IMS datasets and the inherently complex nature of biological tissue.[242] Currently, two approaches exist for analyzing clinical IMS data: Histology-driven IMS approaches where one determines IMS regions of interest based on histopathology annotations of stained serial sections, and

histology-independent approaches where regions of interests are determined from multivariate molecular patterns inherent to the IMS data.[143] Upon isolating and validating signal patterns found in tissue, IMS offers the capability to automatically classify the topography of new samples.[243] When a sufficient spectral library has been generated and correlated with pathology and/or clinical outcomes, IMS data can then be further mined for potential disease biomarkers. Thus IMS can compliment a subjective semi-quantitative pathology assessment with an automated objective quantitative assessment. Equally important is that this automated methodology can generate a quantitative numerical output within a fraction of the time that it takes to deliver a conventional, semi-quantitative pathology report in most clinical institutions.

Here we describe the use of IMS to generate an objective automated quantification for grading CRCLM that reflects disease progression and overall survival. In addition, we propose that this approach can identify lipid biomarkers that can better prognosticate and serve as potential therapeutic targets as well as further our understanding of the role of lipids in the mechanisms of cancer progression. Briefly, our workflow begins with IMS data acquisition from CRCLM specimens in both positive and negative ionization modes allowing us to detect a greater number of potentially discriminant lipid species (**Figure 4-1**- step 1). The spectral data is then pre-processed (normalization, smoothing and peak picking) and the resultant peak data segmented with the spatially-aware k means algorithm (unsupervised clustering) (**Figure 4-1**- step 2). The generated segmentation map is then correlated with a five stain histological panel to determine lipid signatures of major histological areas (**Figure 4-1**- step 3). From here, a spectral library is generated from the histologically correlated IMS data. The spectral library were used to train a classifier that was validated by classifying an independent cohort of specimens. The robustness of the lipid signature for classification was evaluated by a specialist pathologist comparing serial H&E stained sections and IMS classification over the cohort (**Figure 4-1**-step 4). This validation was further evaluated by observing comparable clinical

application between IMS and independent pathologists (**Figure 4-1**-step 5). Finally cancer biology and biomarker discovery can be investigated by further mining of the data for individual or classes of histologically discriminant lipids (**Figure 4-1**-step 6).

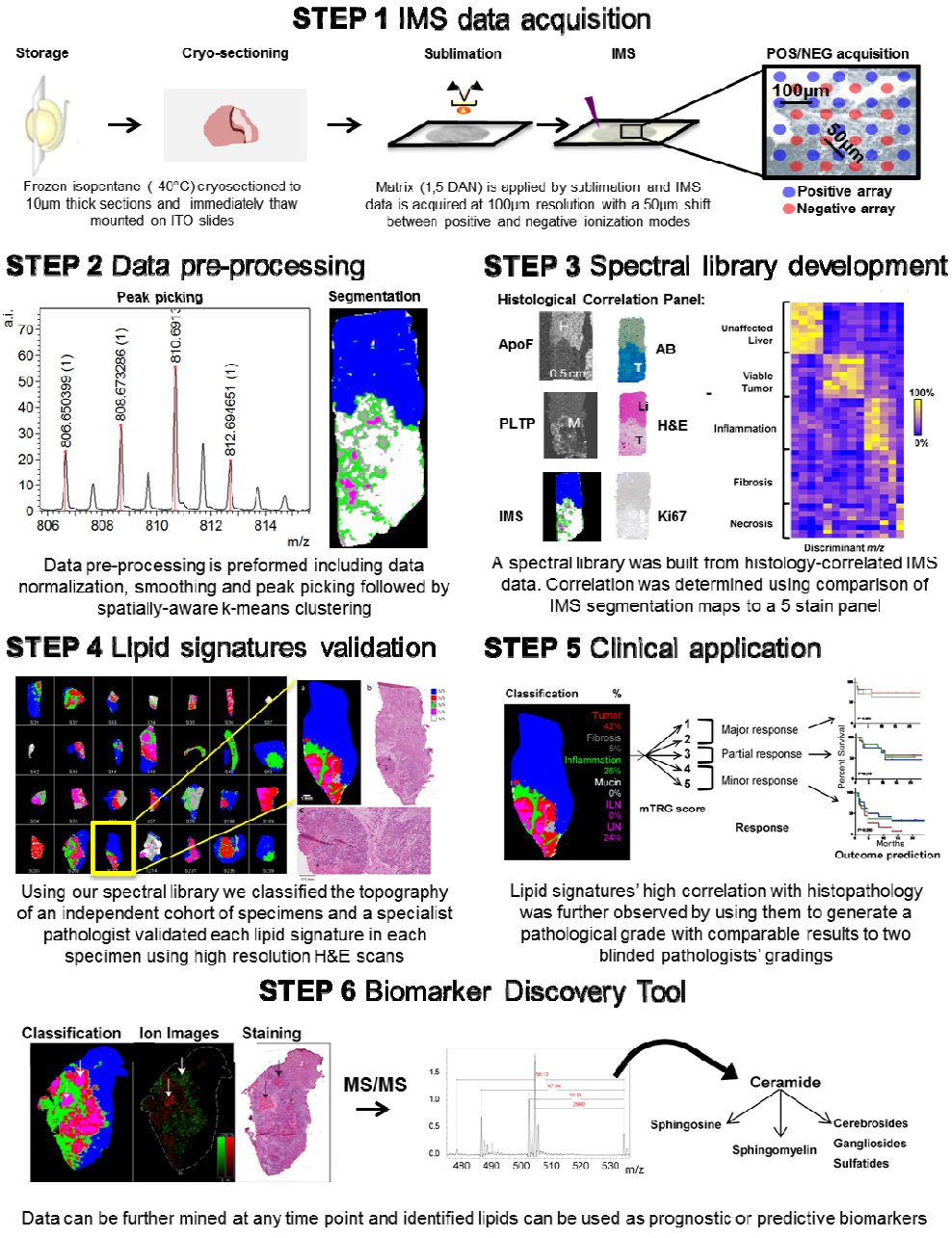


**Figure 4-1. Workflow employed to determine histological markers and generate mTRG scores.**

# 4.3 Results

## 4.3.1 Correlation of histopathology to imaging mass spectrometry

The initial goal was to determine whether signatures derived from IMS data are capable of robustly distinguishing different histopathological features within CRCLM tumor specimens. To achieve this, a training set of 12 CRCLM specimens from 12 patients was analyzed by IMS. The acquired IMS spectra were segmented in an unsupervised fashion (spatially aware k-means clustering) based on their location within the sample (x-y coordinate) and lipid content (peak intensity data). The segmentation maps were then correlated to tumor morphology through a series of stainings from the same specimens, generating robust histological lipid signatures. Liver lesions ranged in size between 0.3 and 9.2 cm with an mean of 4.7 cm. The mean follow up for this cohort of patients was 30.2 months. Overall survival (OS) and disease free survival (DFS) by the end of the study period in this group of patients was 81.8% and 48.6% respectively. Data presented in supplementary **Chapter 4: Supplemental Table 1** and **Chapter 4: Supplemental Figure 1**.

Figure 4-2 illustrates IMS segmentation of a tissue section from the training set, visually correlated to a high resolution scan of the H&E stain of the same section at low magnification (Figure 4-2-A). Segmentation of the data into 7 molecular signatures was able to identify 6 different histopathological regions of the tumor, as one cluster was defined by MALDI matrix. We have color coded the 6 signatures (a signature is defined as a lipid intensity profile unique to a histopathology) as: adjacent unaffected liver (blue), tumor (red), necrosis (purple), fibrosis (grey), inflammation (green) and mucin/MALDI matrix noise (white). Clustering algorithms provide an automated means of ROI selection reducing the introduction of non-relevant IMS pixels that occurs with manual selection of ROI in microscopically heterogeneous samples. It also allows the comparison of histologies across a cohort (i.e. comparison of tumor cells from

one sample to another). A tile plot of average peak intensity shows univariate comparisons of 14 top marker ions for the correlated topographies (Figure 4-2-B). Receiver operator characteristic (ROC) curves were calculated for all picked peaks and the calculated area under the curve (auROC) determined the most discriminant. In the ROC analysis, histologies were compared in a one vs. all approach, effectively excluding markers that may be discriminant for a combination of histologies.

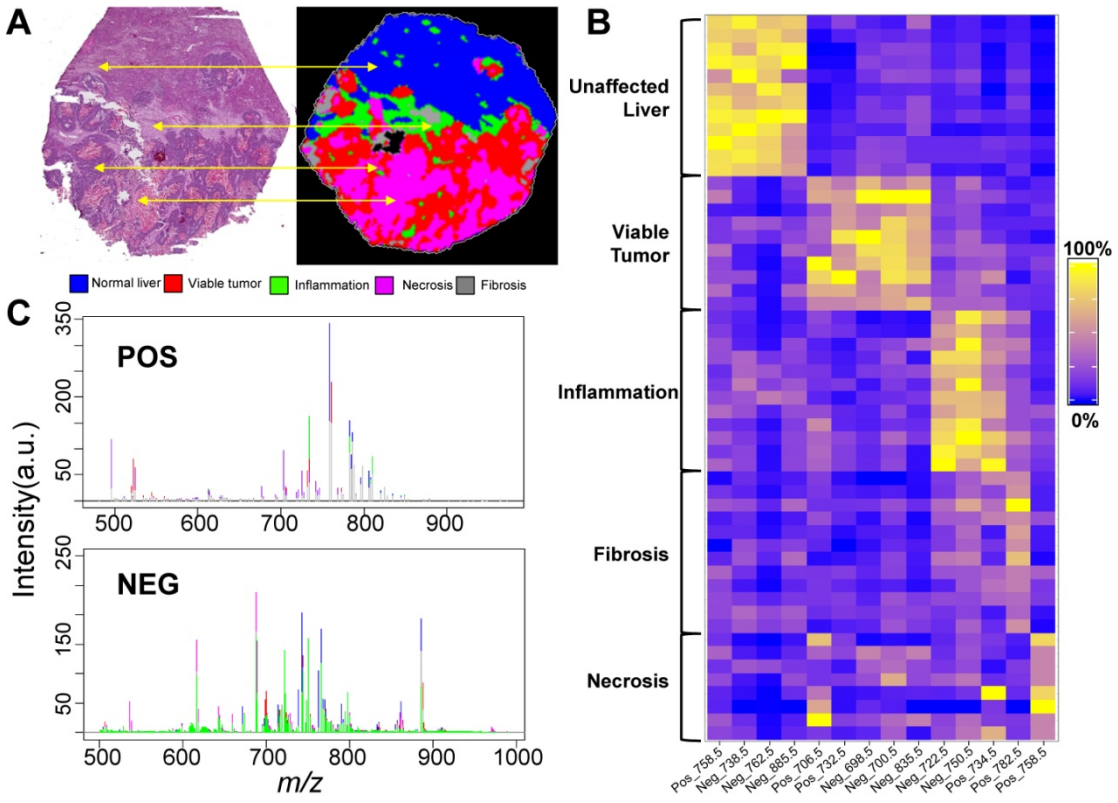


Figure 4-2. **Correlation of IMS to histological staining and mining IMS data. A)** Visualization of the workflow employed comparing IMS segmentations to staining of serial sections. Color scheme of various detected regions is given below. **B)** Tile plot of signal intensity of averages of 14 most discriminant markers from IMS listed by correlated histology. **C)** Averages from peak data of the regions detected by IMS.

| Topography | *m/z* | Identity | Fold change | auROC | MS/MS |
|---|---|---|---|---|---|
| Normal | NEG_738.5 | PE(16:0/20:4) | 3.161 ± 0.23 | 0.923 | FA-1:255,FA-2:303,434(Etn),452(Etn) |
| | NEG_762.5 | PE(16:0/22:6) | 4.827 ± 0.45 | 0.940 | FA-1:255,FA-2:327, 434(Etn),452(Etn), 506(Etn),524(Etn) |
| | NEG_885.56 | PI(18:0/20:4) | 3.227 ± 0.19 | 0.964 | 303, 283 (fatty acyl chains), 297 (Glycerophosphoinositol), 241 (Inositol phosphate ion) |
| | POS_758.57 | PC(16:0/18:2) | 2.71 ± 0.66 | 0.996 | Li_fragmentation: 508(NL of 16:0), 484(NL of FA 18:2), 508(NL of 16:0), NL of 59, NL of 183 (PC headgroup) |
| Tumor | NEG_698.48 | PE(p-16:0/18:2) | 2.408 ± 0.42 | 0.878 | FA-2: 279, 436 (Loss of sn2 acyl chain as ketene (RCH=C=O) from [M-H]-) |
| | NEG_700.51 | PE(p-16:0/18:1) | 2.151 ± 0.52 | 0.864 | FA-2: 281, 436 (Loss of sn2 acyl chain as ketene (RCH=C=O) from [M-H]-) |
| | NEG_835.54 | PI(16:0/18:1) | 2.813 ± 0.63 | 0.885 | 281, 255 (fatty acyl chains), 297 (Glycerophosphoinositol), 241 (Inositol phosphate ion), 673(NL of inositol) |
| | POS_706.55 | PC(14:0/16:0) | 2.835 ± 0.51 | 0.829 | 184(PC headgroup), ~0.7 ppm error |
| | POS_732.55 | PC(16:0/16:1) | 5.355 ± 1.29 | 0.921 | Li_fragmentation: 480(NL of 16:1), 482(NL of 16:0), NL of 59, NL of 183 (PC headgroup) |
| Inflammation | NEG_722.49 | PE(p-16:0/20:4) | 3.749 ± 0.62 | 0.935 | 436(Loss of sn2 acyl chain as ketene (RCH=C=O) from [M-H]-), 303(FA chain) |
| | NEG_750.53 | PE(p-18:0/20:4) | 3.744 ± 0.66 | 0.845 | 464 (Loss sn2 acyl chain as ketene (RCH=C=O) from [M-H]-), 303(FA) |
| | POS_734.57 | PC(16:0/16:0) | 3.673 ± 0.72 | 0.942 | Li_fragmentation: 478(NL of 16:0), NL of 59, NL of 183 (PC headgroup) |
| Fibrosis | POS_782.55 | PC(18:2/18:2) | 1.5 ± 0.61 | 0.780 | 184(phophotidylcholine headgroup) |
| Infarct-like Necrosis | POS_703.57 | SM(d18:1/16:0) | 5.62 ± 0.66 | 0.902 | Li_fragmentation: 280(sn-2 loss), NL of 59, NL of 183 (PC headgroup) |
| | NEG_616.47 | Cer-1-P(d18:1/16:0) | 4.83 ± 1.12 | 0.880 | 96(phosphate group),78(phosphate-$H_2O$) |
| Usual Necrosis | POS_742.57 | PC(p-16:0/18:2) | 2.20 ± 0.43 | 0.823 | Li_fragmentation: NL of 189 (PC headgroup),279(NL of 189 + NL of non-plasmenyl FA) |
| | POS_744.59 | PC(p-16:0/18:1) | 5.16 ± 1.14 | 0.911 | Li_fragmentation: NL of 189 (PC headgroup),279(NL of 189 + NL of non-plasmenyl FA) |
| | POS_746.59 | PC(p-16:0/18:0) | 5.56 ± 0.78 | 0.912 | Li_fragmentation: NL of 189 (PC headgroup),279(NL of 189 + NL of non-plasmenyl FA) |
| | POS_768.57 | PC(p-18:0/18:3) | 5.02 ± 0.98 | 0.902 | Li_fragmentation: NL of 189 (PC headgroup),307(NL of 189 + NL of non-plasmenyl FA) |
| | POS_770.59 | PC(p-18:0/18:2) | 3.94 ± 0.74 | 0.872 | Li_fragmentation: NL of 189 (PC headgroup),307(NL of 189 + NL of non-plasmenyl FA) |
| | POS_772.59 | PC(p-18:0/18:1) | 3.54 ± 0.88 | 0.854 | Li_fragmentation: NL of 189 (PC headgroup),307(NL of 189 + NL of non-plasmenyl FA) |
| | NEG_536.50 | C16 Cer(d18:1/16:0) | 4.83 ± 1.19 | 0.945 | 506(NL of $H_2CO$), 504(NL of $H_2$-$H_2CO$), 488(NL of $H_2O$-$H_2CO$), 296(side chain loss), 254(FA loss) |

**Table 4-1 Table of characteristic ions.** Fold change and auROC calculated vs all other histologies. Etn = ethanolamine. NL = neutral loss. FA = fatty acid. PC = phosphotidylcholine.

PE=phosphoethanolamine. SM = Sphingomyelin. p-16:0/p-18:0 = plasmenyl lipid. Cer = Ceramide. PI = phosphoinositol.

IMS segmentation maps for the training set are shown in the farthest right column in **Chapter 4: Supplemental Figure 2** and again at higher magnification in **Chapter 4: Supplemental Figure 3**. The collation of the histological and IMS data allowed us to generate a IMS spectral library sorted by histopathological region. **Table 4-1** indicates the most discriminant species' topographies, masses, auROCs, fold changes, identity, and characteristic MS/MS ions (Individual ion images and annotated MS/MS spectra of the top markers are presented in **Chapter 4: Supplemental Figure 4** and **Chapter 4: Supplemental Figure 5**). These data show that IMS signatures can discriminate different histopathological features of colorectal cancer liver metastasis specimens.

## 4.3.2 Validation of Lipid signatures

We then used a classifier developed from the training set's segmentations and lipid signatures to classify the topography of 40 additional specimens by partial least squares–discriminant analysis (PLS-DA). The IMS predicted segments of this cohort of specimens (**Figure 4-3**-A-C, representatives of 3 specimens) were validated by comparing a pathologist anootation of each specimen's high resolution H&E scans (**Figure 4-3**- columns 2, 3 & 4) for the different histologies. Comparison of the IMS and pathologist's assignment of tissue types showed strong correlation between the two (**Figure 4-3**, column 5). For example, the sample in **Figure 4-3**-A IMS shows large areas of red indicating tumor cells verified by the H&E stain (**Figure 4-3**-column 3 & 4: magnified tumor area). Within the dense tumor cell areas, there are small areas of tumor stroma with inflammation (**Figure 4-3**-A: columns 1 & 2, indicated by arrow) evident in the H&E by their lighter pink stain compared to the dark purple staining of the tumor cells, that are also well classified by IMS in green (**Figure 4-3**-A: columns 1 & 2, indicated by arrow).

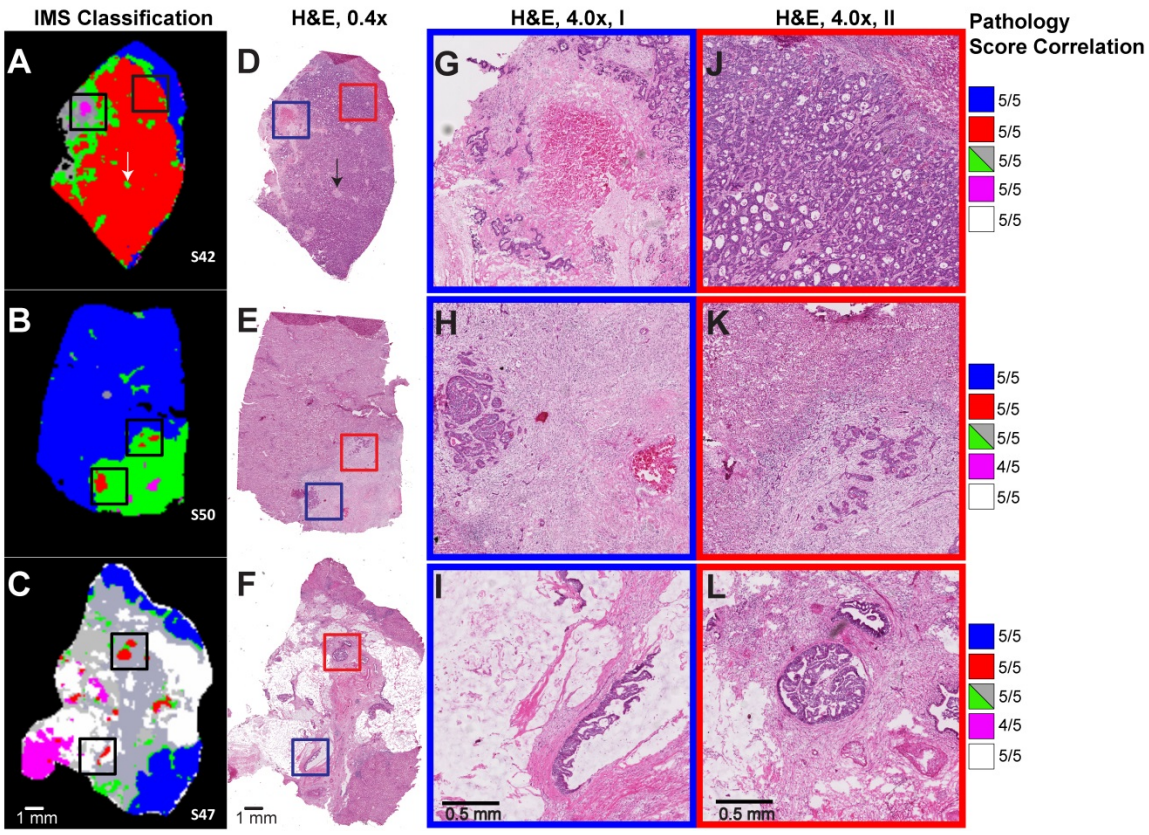


**Figure 4-3. Partial least squares-discriminant analysis classifications of tissue topography.** (3 representative samples classified based on the previously extracted segmentations) Box A-C: classified IMS image. D-F: low-magnification (0.4x) H&E staining of serial section. G-L: H&E staining of two areas from serial sections (high magnification,4.0x); G: enlargement of Blue box from D showing area of necrosis,; J: enlargement of Red Box from D showing tumor cells; H and I: enlargement of Blue boxes from E and F respectively showing small foci of tumor; K and L: enlargement of Red boxes from E and F respectively showing small foci of tumor; Right-most: Pathology correlation score. Arrows in Box A and D show small inflammation areas within tumor.

Each classified region, according to the lipid signature was scored from 1 to 5 for every lesion, 1 indicating $1/5^{th}$ of the histology matching and $5/5^{th}$ complete correlation. During the

development of the lipid signatures distinct areas of fibrosis and inflammation were identified. However, the pathologist was not able to evaluate the amount of inflammation if it was mixed within fibrosis (inflammatory fibrosis) on H&E staining as further special staining is needed to differentiate between their designated histologies. Since pathological response assessed by mTRG does not require the differentiation between the two, the IMS fibrosis (grey) and inflammation (green) segments were treated as one during evaluation. The adjacent unaffected liver (blue), tumor (red), necrosis (purple), fibrosis/inflammation (grey/green) and loose tissue mucin (white) segments scored an average of 5, 4.9, 4.5, 4.9, and 4.7 respectively indicating a very high level of correlation between the IMS prediction of all histologies in this cohort of specimens.

Classifications for a subset of our cohort with their validation score using the system described above are available in Supplemental Annex (attached as pdf) along with H&E staining of serial sections for comparison. One should note that the pathologist's evaluation was performed visually and compared to our color schemes for each histology; therefore an absolute quantitation is not possible. These data show that the IMS signatures developed from the initial training set can also discriminate different histopathological features of a tumour in a validation sample series.

### 4.3.2 Mining of the necrosis segmentation identified the two distinct types of necrosis

We next evaluated whether IMS signatures can differentiate infarct-like necrosis (ILN) and usual necrosis (UN) in CRCLMs. ILN is characterized by confluent areas of strong eosin staining while UN, found within tumor cell glands, also stains strongly with eosin, but is patchier and mixed with nuclear debris. Further, a ring of fibrosis sometimes surrounds ILN, whereas UN is found within the glands of CRC cells. ILN has been correlated with response to treatment and better

prognosis, whereas UN is considered a normal process of tumor cell proliferation and is associated with a worse patient outcome[235].

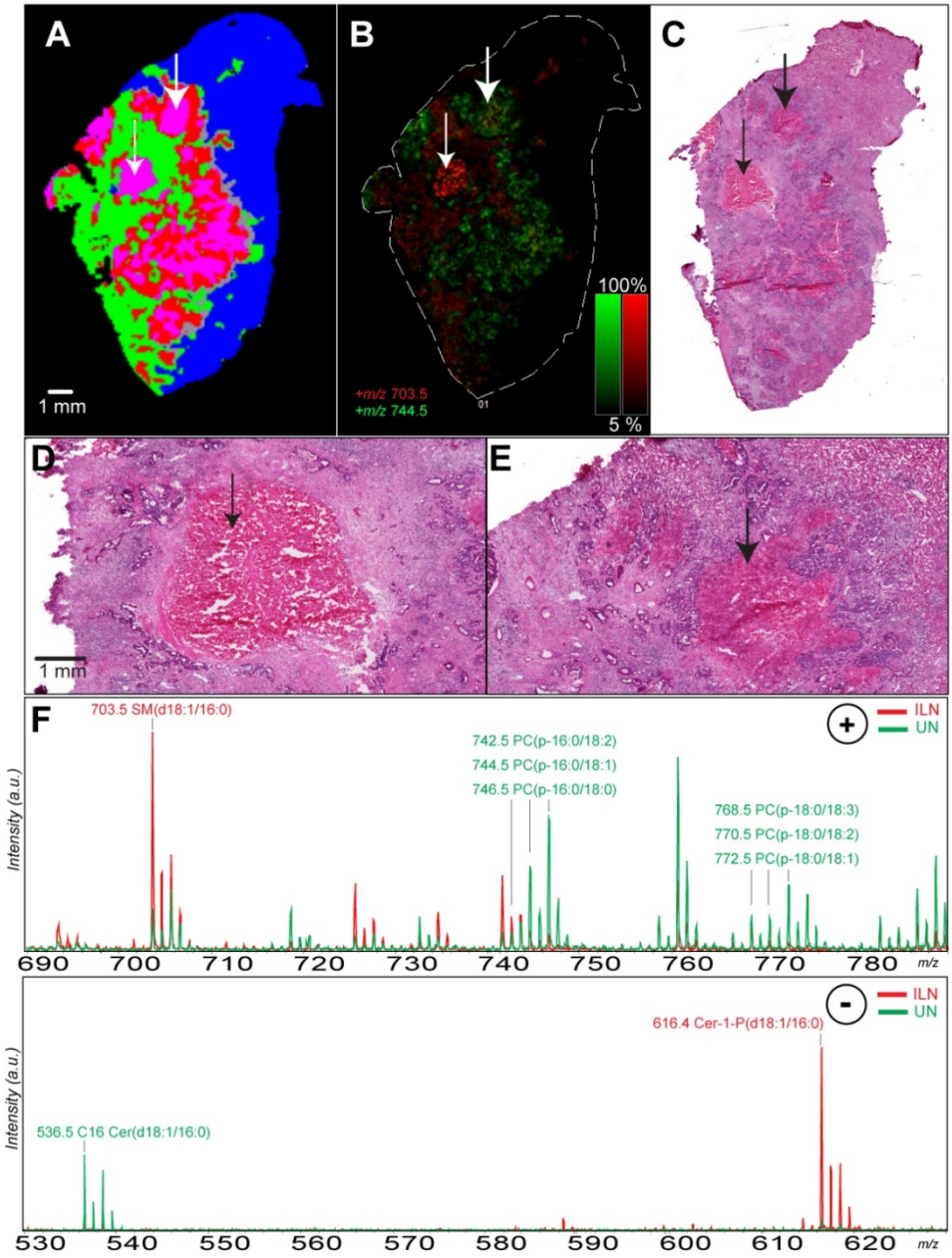


**Figure 4-4. IMS detection of infarct-like necrosis (ILN) and usual necrosis (UN). A)** IMS classification of sample, thin left arrow in ILN, fat right arrow in UN. **B)** Positive ionization mode ion images of *m/z* 703.57 (SM(d18:1/16:0)) in red and *m/z* 744.57 PC (p-16:0/18:1) in green. **C)** low-magnification (0.4x) H&E staining of serial section. **D-E)** High magnification (4.0x) of H&E

staining showing areas of ILN (left) and UN (right) from serial section. **F)** Representative spectra of the ILN and UN regions from the positive (top) and negative ionization modes (bottom). Lipid species identified are described in Table 1, with MS/MS spectra available in Supplemental Figures.

Mining of the necrosis IMS segmentation revealed lipids capable of discriminating the histologies. **Figure 4-4**-A shows a classified IMS sample with necrotic areas indicated in purple. In positive ionization mode, a spingomyelin (SM(d18:1/16:0), m/z + 703.57) was found to be abundant in ILN (**Figure 4-4**-B, red) and several PC plasmalogen species of different fatty acid chain length (**Table 4-1**, **Chapter 4: Supplemental Figure 6**) more abundant in UN (**Figure 4-4**-B, green, m/z + 744.59, PC(p-16:0/18:1)). These areas were confirmed under high-magnification H&Es (**Figure 4-4**-C, D & E). In addition, we identified C16 ceramide (Cer(d18:1/16:0), m/z -536.50) to be abundant in UN and C16 ceramide-1-phosphate (Cer-1-P(d18:1/16:0), m/z -616.47) to be abundant in ILN. All necrosis related species were identified through MS/MS fragmentation (**Chapter 4: Supplemental Figure 6** & **Chapter 4: Supplemental Figure 7**). Salient statistical information for these markers is available in **Table 4-1** and representative spectra from positive and negative ionization mode are displayed in **Figure 4-4**-F with the mass and names for all relevant species. These data show that IMS signatures can successfully discriminate different types of necrosis (ILN and UN) in tissue specimens and identify unique lipid markers within each histology, importantly, these types are necrosis are clinically relevant.

### 4.3.2 Exploring clinical application/relevance of the automated CRCLM IMS analysis

| mTRG | IMS lipid signature profile | |
|---|---|---|
| | *area viable tumor + UN (%)* | *area fibrosis + inflammation (%)* |
| 1 | 0 | 0-100 |
| 2 | <7 | 0-100 |
| 3 | ≥7 and < 50 | ≥50 |
| 4 | ≥50 | ≥5 |
| 5 | ≥50 | 0-5 |

**Table 4-2. Percentage of histological area used in calculation of mTRG.**

| | Pathologist 1 | Pathologist 2 | MALDI IMS |
|---|---|---|---|
| **Pathologist 1** | | 0.7361 | 0.8121 |
| **Pathologist 2** | 0.7361 | | 0.6227 |
| **MALDI IMS** | 0.8121 | 0.6227 | |
| **Average** | 0.7741 | 0.6794 | 0.7174 |

**Table 4-3. Correlation of pathologist and IMS mTRG grading (n=52).** Showing a high overall correlation of IMS based grading scores with the two pathologists (r=0.717, p<0.0001).

To evaluate the robustness of the classifications based on lipid signatures and their clinical application, we generated an automated, objective mTRG score from the IMS data. mTRG is a CRCLM tumor grading system that scores sections stained by H&E based on the presence and amount of the following histologies: viable tumor cells, usual necrosis, infarct-like necrosis and fibrosis. We developed an algorithm that converts the histologically correlated IMS lipid signatures' classifications to the published mTRG[232,235]. The algorithm was based on published grading guidelines[23] and is summarized in **Table 4-2**. The scores for all the specimens (n=52) were correlated with scores of two independent, blinded pathologists (**Chapter 4:**

**Supplemental Table 2**). Inter-pathologist correlation was observed at r=0.7361 (p<0.0001, **Table 4-3**). The IMS generated scores correlated with both pathologists (r=0.8121 and r=0.6227, for pathologist 1 and 2, respectively, (p<0.0001).

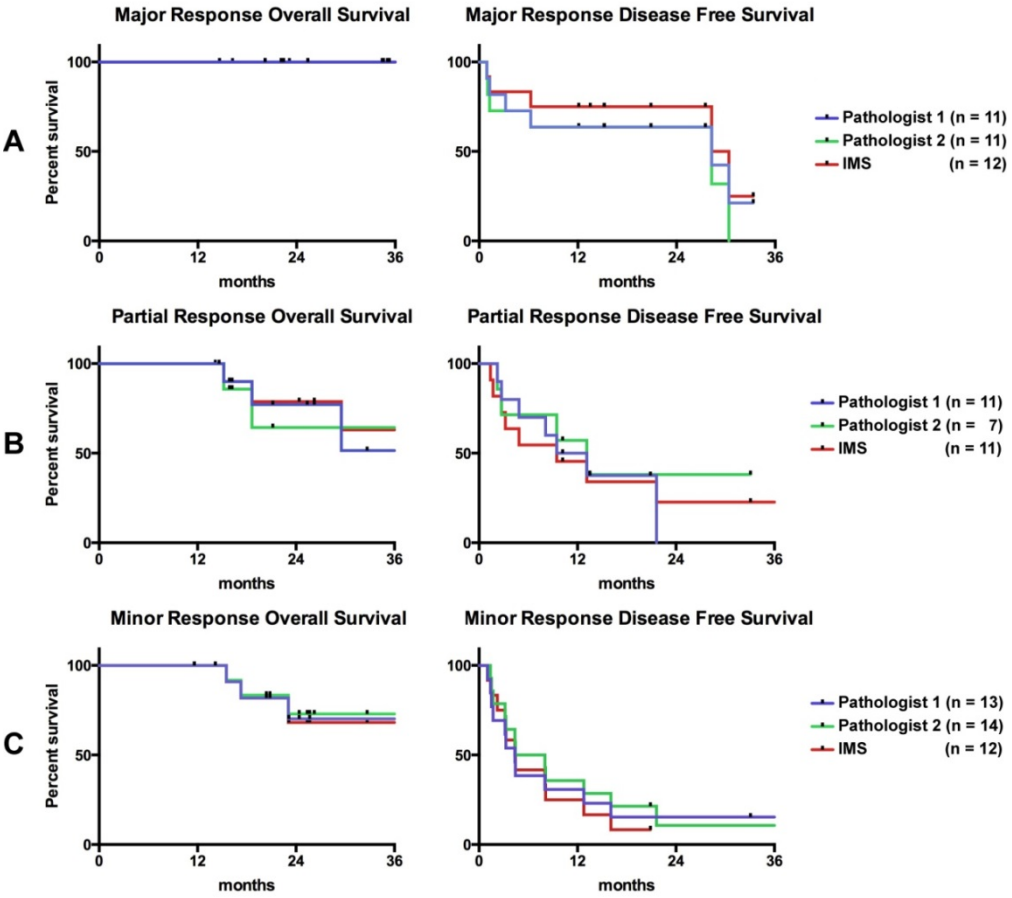


**Figure 4-5. Kaplan–Meier survival analysis for the three response groups stratified according to pathological grading as observed by two independent Pathologists and by IMS.** The p value of the log-rank (Mantel-Cox) test is shown. Significant differences between curves was not observed A) Left: Overall survival (OS) curve for major response group showing 100% OS at 12 and 36 in all three observation groups. All subjects censored. No events in this patient group. Right: Disease Free Survival (DFS) curve for major response groups showing 63.6% DFS for the Pathologist 1 and Pathologist 2 and 75% DFS for IMS at 12 months and 21.7%, 0% and 38% DFS for Pathologist 1, Pathologist 2 and IMS at 36 months respectively. B)

Left: OS curve for partial response group showing 100% OS at 12 months for all three observation groups and 51.4%, 64.2% and 63% OS at 36 months for Pathologist 1, Pathologist 2 and IMS respectively. Right: DFS curve for partial response groups showing 54.5%, 57.1% and 45.4% DFS at 12 and 0%, 38% and 22.7% at 36 months for the Pathologist 1, Pathologist 2 and IMS respectively. C) Left: OS curve for minor response group showing 100% OS at 12 months for all three observation groups and 70.1%, 72.9% and 68.1% OS at 36 months for Pathologist 1, Pathologist 2 and IMS respectively. Right: DFS curve for minor response group showing 30.7%, 35.7% and 25% DFS at 12 months and 15.3%, 10.7% and 8.3% DFS at 36 months for Pathologist 1, Pathologist 2 and IMS respectively.

To demonstrate clinical relevance, we plotted the mTRG grades from the pathologist and IMS lipid signatures to OS and DFS curves (**Figure 4-5**). Patients who received chemotherapy (n=35) were stratified into three response groups according to their scores (major response: grades 1 and 2, partial response: grade 3, and minor response: grades 4 and 5[232]). Three-year OS and DFS were calculated for each group and we observed comparable outcomes in all three gradings (Pathologist 1, Pathologist 2 and IMS lipid signatures,**Chapter 4: Supplemental Table 2**). These data confirm that IMS imaging can be used to provide prognostically useful information.

## 4.4 Discussion

We have succeeded in converting the mTRG from a subjective semi-quantitative grading system into an automated and quantitative system by using IMS lipid-signatures and classification. Importantly, this work was achieved on a relatively large cohort for an IMS study of resected tissues. The use of mTRG calculated by image analysis was comparable to the pathologist's grading in stratifying patients according to their OS and DFS We further demonstated a robust methodology using correlation to many staining and IMS. Compared to

histology driven approaches where one selects ROIs for IMS analysis based on outside annotation, we include the entirety of the IMS data available in our analyses, reducing error and increasing statistical power in inter-sample comparison. Although similar approaches have been described before to distinguish cancer lesions from adjacent normal using lipid signal intensities, previous studies have not partitioned the cancer lesions into their component histologies in such depth as described here[239,244]. This is significant because cancer lesions are composed of multiple tissue types and cancer progression and regression is a dynamic process with composition changes reflecting the status of the lesion. This detailed objective approach to histological evaluation is advantageous as it describes the tumor micro-environment along with the tumor burden. A challenge in the treatment of patients is the assessment of their response in an objective and quantitative manner. Currently a clinician relies on both the pathologist and radiologists assessment, which is very subjective and differs based on experience. By introducing an automated and objective method of evaluation we start to unify patient response grading, moving to a well defined synoptic reporting tool.

Pathologist assessments rely on “eye-ball” estimates of tumor burden and with the introduction of mTRG (differentiating the two types of necrosis) its subjectivity has been driven further. The clinical application of IMS lipid signatures goes beyond pathological grading as it can serve as a valuable tool for refining current grading parameters and the discovery of candidate biomarkers. For example, within the areas of necrosis we identified C16 ceramide and C16 C1P as biomarkers of UN and ILN, respectively. C16 ceramide has been described as having tumor suppressor activity (having both anti-proliferative and pro-apoptotic activities) while in contrast C1P has pro-survival and anti-apoptotic activity, making these lipids attractive biomarker candidates for reponse to therapy[79,245]. It has been reported that high levels of C1P, which stimulates cell division and inhibits apoptosis, is toxic and can kill cells.[246] Alongside the ceramides, plasmalogens were identified in the necrosis areas. Although found ubiquitously in

human cells, they have not been previously described in cancer or necrosis processes, unlike other ether lipids. In addition, they have been reported to be lower in abundance in liver tissue compared to other organs.[246,247] Interestingly, within our data set we identified PE (phosphoethanolamine) plasmalogens to be associated with both tumor areas and areas of inflammation, whereas PC plasmalogens are exclusively abundant in areas of UN. Current research indicates PE plasmalogens as the precursor to PC plasmalogens as no plasmenylcholine desaturase enzyme has been described. Compared to UN, we find minimal PC plasmalogen signal in surrounding liver tissue. The function of these lipids in the specific histologies opens further areas of research. The ability to distinguish between UN and ILN is extremely important and not always obvious when examining CRCLMs histologically. We have identified unique lipid biomarkers for each of these tissue types. In fact we are able to identify ILN areas within UN that has been graded by pathologists to be entirely UN. This needs to be investigated in a larger series of patients to determine if it impacts prognosis or response to therapeutic interventions.

From a technical standpoint, classification based on IMS data will be key in clinical analysis. It will not be practical for a routine clinical pathology lab to examine IMS data ion by ion. Furthermore, many molecules detected by IMS are generic and will be expressed by several types of cells, with changes in their relative abundance distinguishing histologies. By building a larger more heterogeneous spectral library with various types of cancers IMS could be used for diagnostic purposes in differentiating cancer type based on lipid profiles.

This study supports an evidence-based model for decision making in regards to diagnosis, prognosis and intervention for CRCLM. We demonstrate functional linkages between IMS and histopathology and the utility of this “omics” technology in the clinical setting as a companion diagnostic and prognostic tool for pathologists and clinicians. Finally, using lipidomics we have uncovered a novel set of markers (ceramides and plasmalogens) to start investigating the

mechanism of treatment effects and possibly novel drug targets. The introduction of IMS into the clinic and as a new tool for biomarker discovery will dramatically change the field of molecular pathology.

# 4.5 Methods

## 4.5.1 Clinical data

This retrospective study included a total of 52 lesions from 50 patients. Resections were preformed between November 2011 and July 2014. Clinical data was collected for each patient through the locally established hospital database and medical records. Included within the data are demographics, primary and metastatic disease characteristics, relevant laboratory results, chemotherapy and co-morbidities. As shown in the supplemental **Chapter 4: Supplemental Table 1**, median age of diagnosis was 63 (range 31-81) years. Rectal cancer accounted for 34% of the cases. Approximately two thirds (64%) of the patients had synchronous liver metastasis (developed metastasis within a year of diagnosing the primary). Seventeen lesions were chemo-naive while the rest received neoadjuvant chemotherapy with an average of 7 cycles (Range 3-28). Estimated 1 and 3-year OS is 100% and 82.6% respectively. Twenty-seven (54%) of patients had recurrence in the liver, estimated 1-year and 3-year DFS is 49.9% and 44.4% respectively (26.5 months mean follow up duration).

## 4.5.2 Tissue sample acquisition

Informed consent was obtained from all patients through the MUHC Liver Disease Biobank (LDB: MUHC research ethics board approved protocol). Surgical specimens were procured and released to the biobank immediately after the pathologist's confirmation of carcinoma and surgical margins. The specimens were frozen, within 30 minutes, according to the LDB standard operating procedures and processed as previously described[89].

## 4.5.3 Histochemical staining

Frozen tissues were cut using a cryostat at 10 µm, and stored at -80°C in tightly closed boxes until staining. Before use, the slides were allowed to dry on the benchtop for 10 minutes at room

temperature and then fixed for 60 minutes in freshly made 4% formaldehyde dissolved in 0.1 M phosphate buffer at pH 7.2. Comparative topography assays were performed between IMS and different histological stains: Apolipoprotein F (ApoF) in-situ hybridization (ISH), Phospholipid transfer protein (PLTP) ISH, alcian blue (AB)[248], H&E, and Ki67 immunostaining[249], of the training set. ApoF ISH is hepatocyte-specific, defining regions of liver adjacent to the tumor area; PLTP ISH labeling revealed the concentration of macrophages within or around the tumor; AB stains areas of the metastastic lesions that contain mucin; H&E staining provided basic histological information for IMS correlation and pathological grading; Ki67 immunostaining identified tumor cells with cell cycle activity.

### 4.5.4 In situ hybridization

*In situ* hybridization (ISH) was performed with [$^{35}$S]-labeled riboprobes synthesized *in vitro* from DNA Templates. Briefly, mouse Apolipoprotein F (ApoF, GenBank AF411832.1) DNA template of 675 bp was produced by PCR using sense gataccagatgcagacctca and antisense gttcgtcgttgttgacaaga primers. Human phospholipid transfer protein (PLTP, GenBank NM_006227.3) DNA Template of 884 bp was produced using GAAGAGCGGATGGTGTATGT (sense) and TGGTGGACGGACTGTAATTG (antisense) primers. Sequences recognized by SP6 Polymerase (5′-GCATTAATTTAGGTGACACTATAGAAGCG-3′) were attached to antisense and T7 Polymerase (5′-GCGCTATAATACGACTCACTATAGGGAGA-3′) to sense primers. Following hybridization, the results were visualized by x-ray film autoradiography showing anatomical level topography and emulsion autoradiography showing cellular level ISH labeling. Figure S2 represents the staining of the training set lesions.

### 4.5.5 Pathological evaluation methods

The following methods were used and compared to evaluate our lipid signatures:

i. Modified tumor regression grading (mTRG): All 52 lesions were stained (detailed in **Chapter 4: Supplemental Table 1**) to identify areas and relative percentage of viable liver cells, fibrosis, inflammation, mucin, usual necrosis and infarct like necrosis. Two independent pathologists assessed modified Tumor Regression Grade (mTRG) as described by *Chang et al.* for every sample using high-resolution H&E slide scans (**Chapter 4: Supplemental Table 2**).[235] For the mTRG grading UN was defined as containing nuclear debris and bordered by viable cells whereas ILN was defined as being a large confluent areas of eosinophilic cytoplasmic remnant located centrally within the lesion without the presence of nuclear debris. Briefly, mTRG1 is defined by the absence of tumor cells and replaced by fibrosis and ILN; mTRG2 contains rare scattered residual tumor cells with predominant fibrosis and the presence of both ILN and UN; mTRG3 contains more residual tumor cells throughout predominant fibrosis and UN; mTRG4 contains large amounts of tumor cells and intermingled UN which predominates over fibrosis and ILN; and mTRG5 contains tumor cells and intermingles UN without any fibrosis. The higher the grade the worse the response.

ii. Pathological response: All samples were grouped into 3 response groups based on their mTRG score. Major response includes: grades 1 and 2, partial response: grade 3, and minor response: grades 4 and 5[232].

## 4.5.6 Statistical analysis

Survival probabilities were calculated by the Kaplan-Meier method and compared by the log rank (Mantel-Cox) test. A p value of less than 0.05 was considered statistically significant. All analysis was performed using JMP.11 software. Overall survival was calculated from the date that the metastasis were detected to the date of last follow-up. Disease free survival was calculated from the date of surgical intervention to the date of recurrence or last follow-up if patient was still disease free.

## 4.5.7 Mass spectrometry

### 4.5.7.1 MALDI IMS tissue sectioning and sample preparation

Tissue sectioning and preparation was performed as previously described.[89] Briefly, tissue cryo-sections of 10 µm were thaw-mounted onto ITO coated glass slides (Delta Technologies, Loveland, CO) and 1,5-diaminonapthalene (DAN) matrix (Sigma Aldrich, Oakville, CA) was sublimated on the slide.

### 4.5.7.2 MALD IMS instrument parameters

IMS in both positive and negative polarity of each tissue section was performed using a Bruker MALDI-TOF/TOF Ultraflextreme as previously described with only minor changes.[89] Briefly, 150 laser shots were summed per array position, with 100 µm of resolution for every acquisition. Negative ionization mode was acquired using an offset of 50 µm to positive ionization mode IMS grid array. MALDI laser influence and ion accelerating voltages in reflectron mode were optimized for the sample set. The mass range was *m/z* 460-1200 for both ionization modes.

### 4.5.7.3 MALDI MS/MS

MS/MS measurements for species detected in positive mode were acquired in LIFT-TOF/TOF mode of the Ultraflexetreme and with a Bruker Solarix 15 T FT-ICR using dried droplet spotting of 2,5-dihydroxyacetophenone doped with 100 mM Lithium Trifluoroacetate for improved fragmentation[91] whereas negative species were directly fragmented after DAN sublimation. MS/MS data were processed using flexAnalysis v3.3 software (Bruker Daltonics, Billerica, MA). The LIPID MAPS database was used for comparing accurate mass and obtaining lipid structures for the determination of fragmentation pathways.[203]

#### 4.5.7.4 MALDI IMS data analysis

Data was displayed using flexImaging 4.1 (Bruker Daltonics, Billerica, Massachusetts). Data was exported to imzML format for processing.[122] Spectral smoothing using the Savitzky-Golasky algorithm, Total Ion Current (TIC) normalization, and peak picking using a signal-to-noise ratio of 3.0 were performed using the MALDIquant package in the R environment.[134] Generated peak intensity data were segmenteds using spatially aware K-means (k=7)[144], as implemented in the Cardinal MSI R package.[202] Partial Least Squares – Discriminant Analysis (PLS-DA) and ROC analysis were performed in the R environment using the mixOmics[250] and ROCR[251] packages, respectively.

# Chapter 5: Conclusion and future perspectives

## 5.1 Conclusion

In this thesis, we demonstrated developments in lipid IMS through applications using human and mouse model tissue. Lipids are extremely important biomolecules and their recent inclusion in the gamut of biological imaging by IMS means that many discoveries and applications await development.

Chapter 2 addresses lipid degradation in MALDI IMS studies. The goal of this this was to characterize lipid degradation in tissue sections on a time scale typical of MALDI IMS experiments and describe means to prevent this degradation. We characterized degradation in tissue sections and detected degradation markers in LPLs and OxPLs occurring on time scales typical of IMS experiments. Finally, we determined that freezer storage under $N_2$ is a simple means of inhibiting degradation. This work addresses an important area of research that assures the validity of lipid results and will become increasingly important in a clinical setting where many participants are between the sample and its analysis. In this case, we have clear markers of degradation and best practice protocols.

Challenges exist in how to apply and interpret IMS complex datasets. We looked at two types of large IMS datasets: 3D IMS datasets composed of analyses from a single tissue with sections taken at regular depth intervals, and a large cohort dataset where analyses are taken from different samples.

3D IMS is at a point where potential applications are limited by difficult analysis schemes or lack of freely available tools for reconstruction. In 3D IMS our work addressed several data analysis challenges: alignment, visualization and analysis. We developed simple, intuitive, free tools and made them publicly available. The work and tools demonstrate a pipeline for 3D IMS where a user can take computationally aligned high resolution microscopy data and apply this alignment to coarse resolution IMS data. The tools permit visual section to section alignment of the 3D

data that requires minimal programming skills. We demonstrated the tool's applicability in both a mouse model of atherosclerosis and a human carotid sample. In both tissues, more than one sample preparation and thus IMS dataset was acquired in the interest of a more complete lipid analysis. In the case of the human carotid we acquired all datasets on a single tissue.

Due to simple species like FFAs being imaged by AgLDI and their complex downstream or precursor lipids like PLs and TAGs imaged by other sample preparations, there is a need to examine the disparate datasets inclusively. We addressed this challenge in 3D in atherosclerotic plaques by segmenting the 3D IMS data and finding segments of similar 3D spatial distribution. In this case we found plaques to contain common regions first by their spatial pattern towards the interior or exterior of the plaque. Finally, these spatial patterns were related to an optical staining data, and their histology defined.

We found correlations in lipid distribution across the model and human sample with lysolipids and sphingolipids being present in the lipid core of either type of plaque. Segmentation of the human carotid data allowed us to visualize the development of the lipid core and the changing lipid profile of the outer plaque layer in response to a fuller lipid core. The mouse data revealed areas of TAG abundance in the aortic sinus cusps but not within the plaque area themselves. Human carotid data did not have significant TAGs. The lack of TAGs highlight the diversity of the atherosclerotic plaques, where some are very fibrous like the one we studied and others more lipid rich.

Serial 3D IMS compiles several technical challenges in IMS, but beyond the logistic challenges of analyzing the data, there is contextualization. In the 4$^{th}$ chapter of this work, we demonstrate the integration on IMS with clinical data with an eye towards decision making and automation of the tissue analysis process. Our data demonstrated determination of the mTRG by IMS and tries to combat problems of subjective inter-pathologist grading by creation of an automated

objective and quantitative system through lipid signal analysis. The mTRG we derived from IMS compared favorably to the pathologist data and showed the potential of IMS to compete in this area. Our method is a middle of the road approach between histology driven and data driven IMS analysis: a compilation of stainings are compared with IMS segmented data to determine the molecular histology counterparts to the major stained histologies. Oftentimes, the correlation was unmistakable at lower magnification. It was critical to analyse the CRCLM samples in depth because the development of cancer is a culmination of cellular events reflected in the histologies present, and a too-reductive analysis of “normal” vs “tumor” shuts the door on many potential inter-sample differences in other histologies.

Lipid profiles distinguishing histologies were also interesting and individual markers were able to discriminate between necrosis types. We found a series of PC plasmalogen species that were present in usual necrosis, typical of tumor proliferation. This series colocalized across FA chain length, and consequentially mass. This finding is notable as many normal PC species can have completely different localization based on side chain length or saturation. The class-wise localization of these species points to consistent biology behind their presence. Another surprising feature was the presence of PE plasmalogens in the inflammatory areas. This is especially interesting as PE plasmalogens are necessarily precursors of PC plasmalogens. Plasmalogens have not majorly implicated in cancer processes.

Another interesting result from necrosis was the presence of C16 Ceramide in usual necrosis, and the phosphated version C16 Ceramide-1-phosphate found in infarct-like necrosis. C16 Cer, a long chain ceramide, is implicated in cell survival, through normal autophagy. Whether cell death or survival is determined by ceramides is still an important research question and our results give clues about long chain ceramides in the usual necrosis being pro-survival. [252]

Taken together, this thesis extends in several directions, but is unified by the analysis of lipids and large complex datasets. It seeks to address the technical challenges in IMS data analysis while at the same time promoting IMS is biological and clinical contexts.

## 5.2 Future Perspectives

IMS's niche in tissue analysis is currently being carved out. IMS correlation to clinical and biological variables, and sample preparations accessing previously unimageable biomolecules *in situ* have driven the research interest in IMS, and in turn, developments in technology have aided the capacity of IMS to respond to the biological and clinical research questions posed.

The future developments in MALDI IMS sample preparation will have to increase specificity and sensitivity.[253] Biological studies may be targeted or already have corroborating evidence implicating certain biomolecules, with the question being the localization of the molecule in tissue. Clinical studies are more discovery-based in IMS and the more specific the analysis, or the broader the range of species accessed by IMS, the better for discovery. In general, improvement of sensitivity in tissue section MALDI IMS has been achieved by removal of interfering species.[254,255] For instance, washing away lipids to better detect intact proteins by MALDI on tissue or attempts to specifically remove the most abundant lipids to better image other lipids[256]. This improvement addresses the dynamic range in concentration of biomolecules in any biological tissue where some are extremely abundant and others less so. However, methods that modify matrix for better ionization, derivative species *in situ*[68,257-260], or capture specific species on a separate surface for analysis[261] are more recent and should be a major avenue of research in the future. Perhaps the most challenging aspect of sample preparation that will need to be addressed is in protein and peptide imaging, where seemingly less and less studies are focused. This may be done through more specific peptide or protein capture or other

sample preparations. Regardless of how they are detected, proteins are key in biology and are absolutely necessary to draw all the connections between metabolites.

In some biological and pharmaceutical applications, limitations in imaging resolution are apparent. Drug metabolism and pharmacokinetic studies may wish to localize species down to a subcellular level and there is no doubt this could greatly benefit tissue disease studies for locating the exact cellular machinery producing a potential biomarker or drug target. Sample preparation also plays a role in this aspect as the preparation determines the limit of resolution. Sublimation and other solvent-free matrix deposition techniques have shown the most promising results due to limited delocalization at high resolution. Again, the need for specific analyses comes into play because current solvent free sample preparations only ionize lipid molecules, and sparingly intact proteins.[86] The need for sensitive analysis is also present at high resolution because less material is ablated and therefore less ions are produced. Both instrumental and sample preparation development can relieve this issue.

In clinical application of MALDI IMS, the big movements are likely to be studies demonstrating applicability and eventually studies demonstrating accessibility and ease of use for clinical laboratories. One can imagine an ideal scenario mirroring that of MALDI-TOF MS for the identification of bacterial strains where bacteria are simply grown, put on a MALDI plate, spotted with matrix, spectra are collected and classification of the spectra returns the identification of bacterial species with a quantitative level of confidence. This ideal scenario works because cultured bacterial cells are homogenous in comparison to the complex histologies present in tissue sections from clinical patients or even model animals. To address this compexity, clinical tissue studies of MALDI IMS will have to incorporate evermore histological data to be competitive. Histopathology has an enormous advantage because H&E staining has been performed on every tissue and pathology, and the more than a century of collective knowledge has meant that an H&E performed in one hospital can be interpreted in another. The advantage

of MALDI's unbiased and numerical data is the capacity to database and automate tissue analysis, and beyond that, molecular information will extend past what can be known through staining. Classification-based methods should be vital in this drive to clinical applications as they have been with microbiological applications of MALDI-TOF MS. The question is partly, but not majorly one of finding the right algorithm as several classification algorithms have been successfully implemented in IMS datasets, but more a matter of curating a database and ensuring multi-institutional reproducibility. The lack of standardization in the field would need to be addressed in this case, and this may take time as sample preparation is an active field and even for phospholipids there are more than 5 efficient matrices that can be employed. Besides the logistical questions, there remains a need to develop IMS specific criteria for tissue analysis in the same way a pathologist would grade a tissue. If IMS is to compete with histopathological research, unifying data across types of cancer would be vital. As an example, lymphocytes appear in reaction to cancer and other diseases but whether the IMS signal is consistent across multiple organs is not confirmed. This sort of knowledge may form the basis of a well curated IMS database.

Despite the advances of IMS in tissue imaging in relation to tissue pathology, IMS cannot be said to be widely adopted for this purpose. The issue may be related to instrument cost, expertise required to operate the instrument, and skepticism from the clinical community. However, pilot adoption in pathology labs may be the best push forward in the field.[101]

Clearly, the field of IMS is relatively young and the enormous interest in direct on tissue localization of molecules exists. MALDI IMS remains the most important technique with new technologies coming into the fold for faster and more sensitive MALDI IMS. The potential of IMS hasn't been limited to MALDI however, and other instrumentation and their particular strengths in imaging can no longer be denied. Regardless of the instrumentation employed, IMS data requires the sort of robust and validated analysis strategies described in this thesis.

**Supplemental Annex: supplemental figures, tables, and methods for chapters 2-4**

# Supplemental figures for Chapter 2

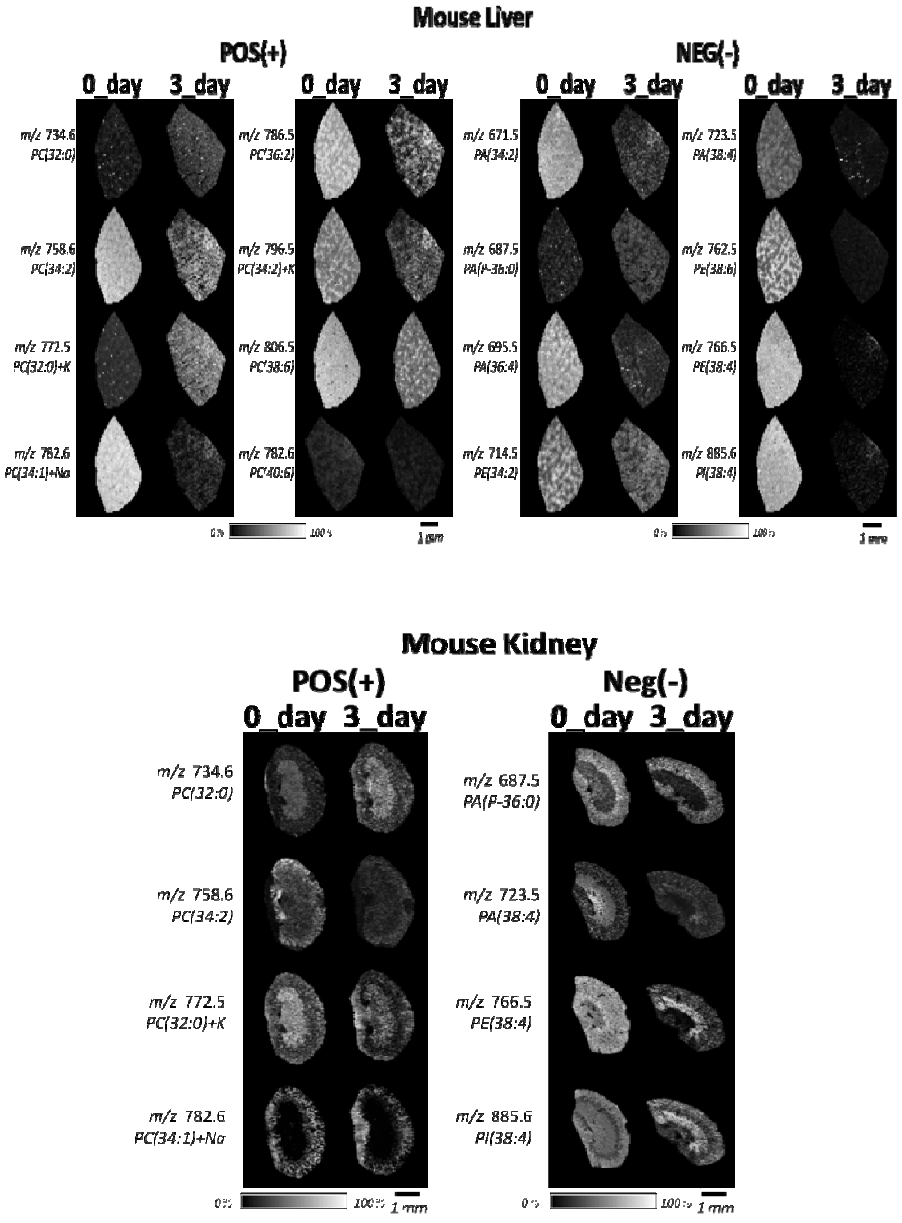


**Chapter 2 Supplemental Figure 1.Temporal changes of lipid peak intensities with representative ion MS images in the positive and negative ionization modes.** The top

panel shows the data coming from a mouse liver at two time points. The bottom panel shows the same data coming from a mouse kidney.

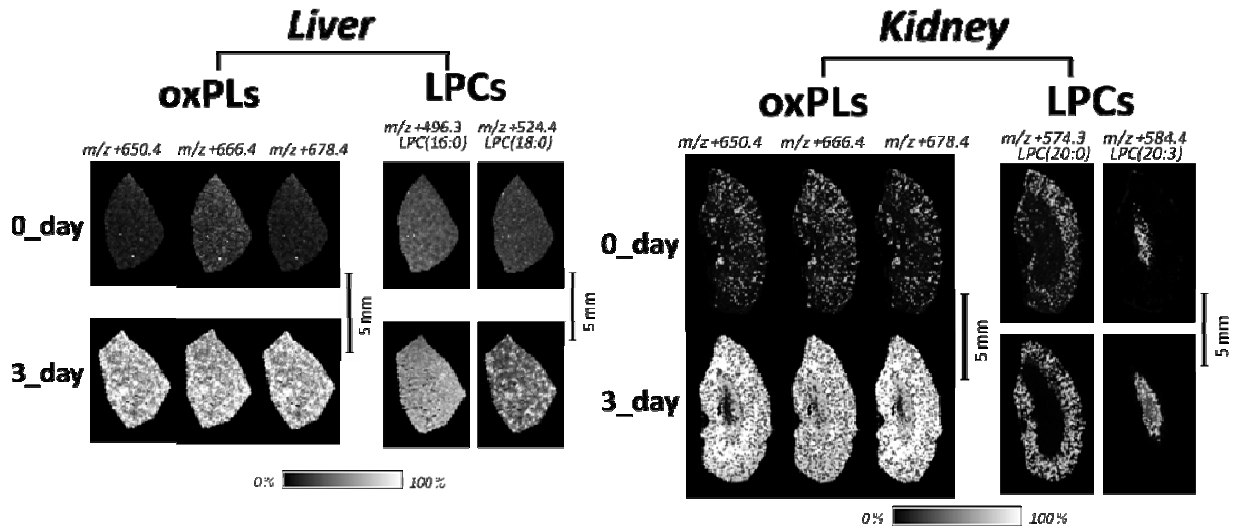


**Chapter 2 Supplemental Figure 2**. **Temporal changes of positive lipid peak intensities of 2 degradation product groups with representative ion images.** The left panel shows the data coming from a mouse liver at two time points with oxidized phospholipids and lysophophatidylcholines marked by OxPLs and LPCs respectively. The right panel shows the same data coming from a mouse kidney.

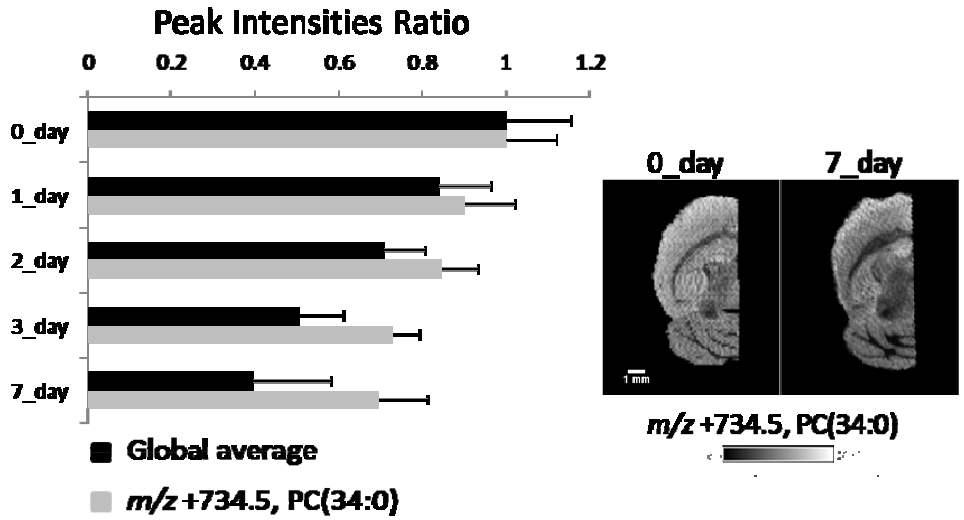

**Chapter 2 Supplemental Figure 3. Comparison of global peak intensity ratios with those of saturated phospholipid PC(34:0).** Left panel is 0 to 7 day comparison plots, and right panel shows representative ion images from 0 and 7 day measurements.

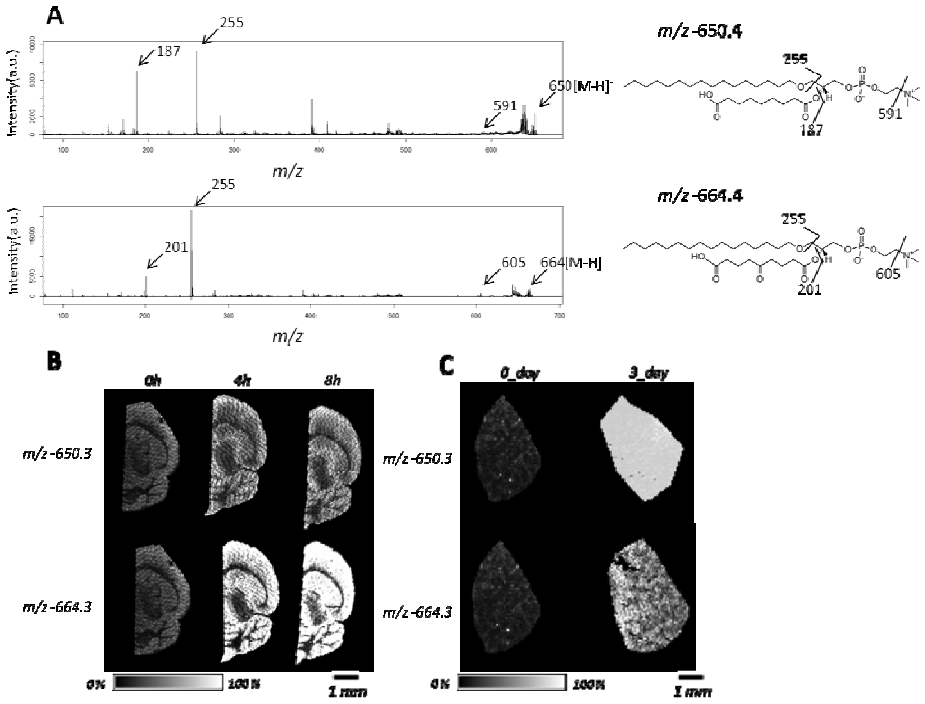


**Chapter 2 Supplemental Figure 4. MALDI MS/MS spectra of oxidized phosphotidylcholines acquired in the negative ionization mode.** Panel A contains MS/MS spectra for *m/z* -650.4 and -664.4, two oxidized phospholipids detectable in negative ionization mode. Panel B displays the corresponding time scaled ion images from mouse brain sections.

Panel C shows the same data acquired from mouse liver sections.

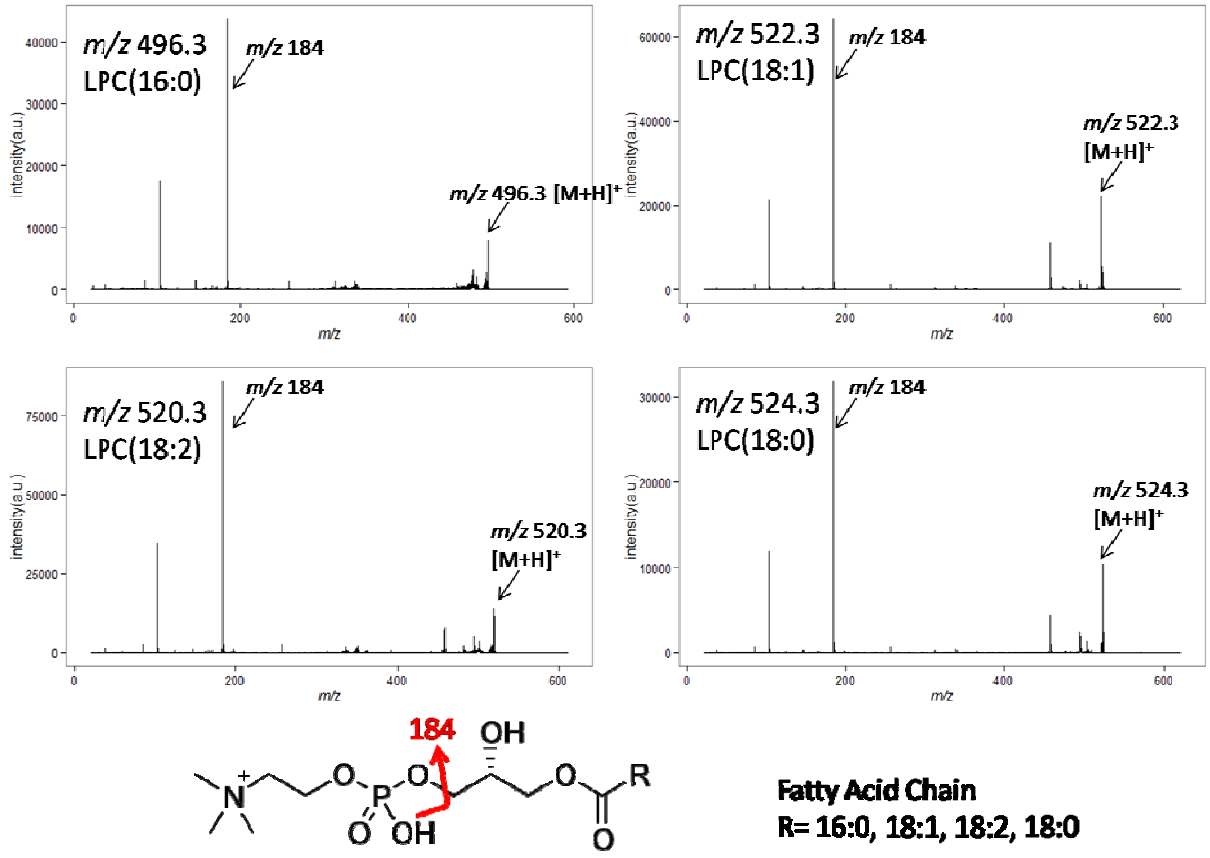


**Chapter 2 Supplemental Figure 5. MALDI MS/MS of 4 lysophosphotidylcholine signals**

Each spectrum displays *m/z* 184, the signal coming from the characteristic loss of the phosphatidylcholine head group. Identification was then performed through LIPID MAPS based on the molecular ion's mass and the lipid class given by the head group. Fragmentation pathways are proposed on a generalized structure.

# Supplemental methods for Chapter 3

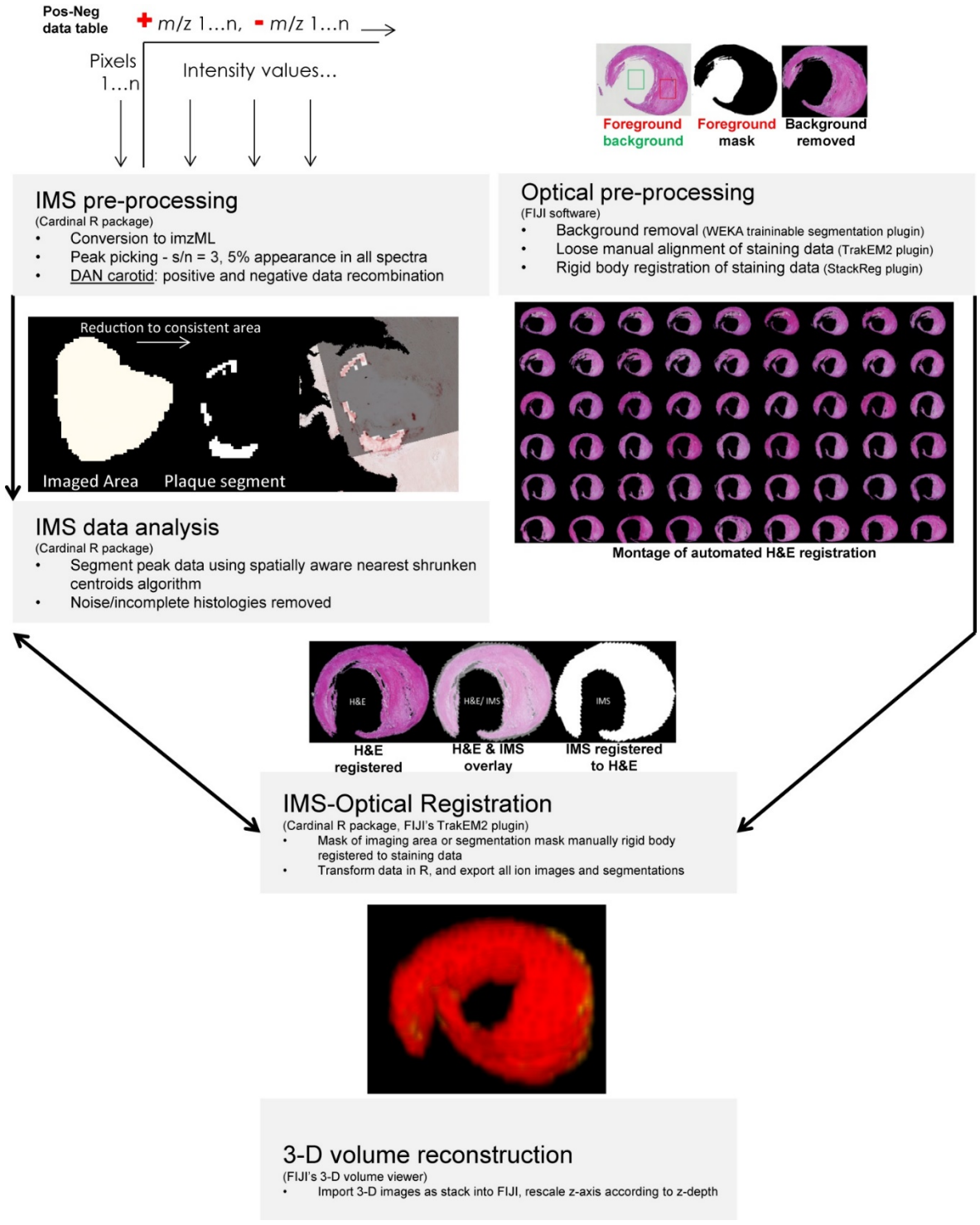


**Chapter 3: Supplemental Methods Figure 1. Outline of the workflow used in 3D reconstruction.** Softwares, plugins, and R packages are listed in parentheses.

## Detailed description of the methods and software employed in 3D IMS reconstruction.

*Multimodal 3D IMS of atherosclerotic plaques sample preparation and data acquisition*

Fresh-frozen artery tissue used in the 3D IMS experiments required embedding for sectioning as the tube-like samples prevents mounting of the tissue with a drop of media. We used OCT to mitigate this problem; embedding using OTC aids in stabilizing the cutting process but introduces signal artifacts as polymer peaks. These were however later useful during data analysis in determining the borders of the imaged tissue.

Analysis of the mouse heart ascending aortas was focused at the heart's aortic valve and roots. 3D IMS was performed on two separate mouse hearts, with one designated for silver-assisted LDI and another for DAN positive/negative MALDI analysis. The small feature size of the mouse ascending aortal roots required imaging resolution that did not allow for dual DAN positive/negative ionization IMS on a single section with the laser focus (~30 μm in "small" setting) of our system. Positive and negative ionization IMS acquisitions were performed using two serial sections with a spatial resolution of 40 μm.

The mouse heart 3D reconstruction for DAN included the analysis if 31 sections resulting in 41,914 and 38,513 imaging pixels in positive and negative mode, respectively. The discrepancy in total pixel number is due to imaging area selections. For the mouse heart, sections were kept and after matrix removal in 100% ethanol of 30 s stained with ORO (colors neutral lipids red, indicates plaque formation) at every 100 μms prior to the aortal plaque in order to build 3D reconstructions of the whole heart volume and embed the IMS data within. Silver-assisted LDI IMS resulted in 117,152 imaging pixels over 64 sections at 30 μm imaging resolution. However in this case, only 31 sections (61,140 pixels) contained plaque and the rest were acquired before the plaque out of prudence. The plaque produced a yellow color after silver sputter

deposition, roughly indicating the area to image (Figure 1). As the plaque was the only mouse heart histology consistently imaged in its entirety, sections without plaque were excluded for 3D reconstruction.

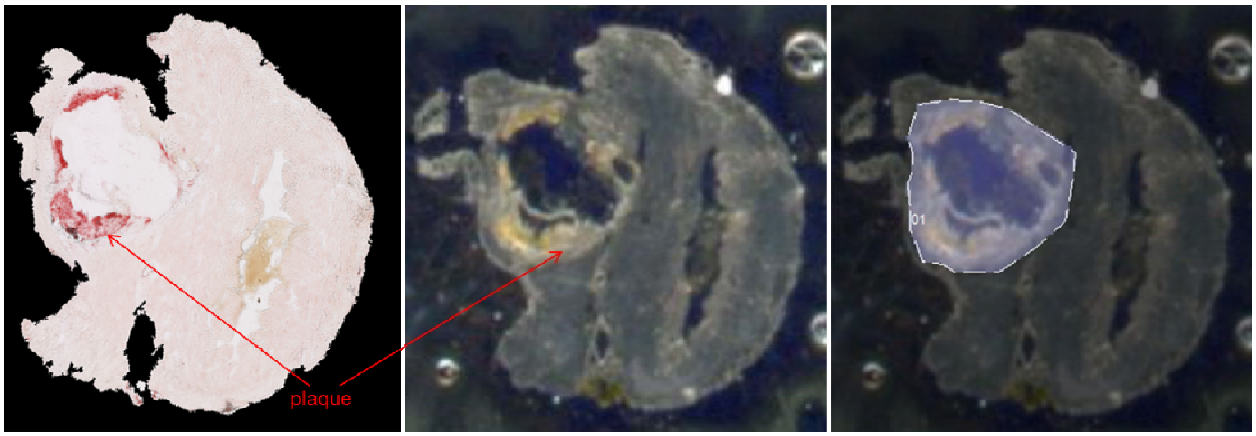


**Chapter 3: Supplemental Methods Figure 2. Appearance of heart tissue after silver sputter deposition.** Appearance of the tissue helped guide selection of areas to be analyzed by IMS.

The larger feature size of the human atherosclerotic tissue allowed IMS resolutions capable of dual positive/negative ionization mode MALDI IMS thus the human carotid sample was sectioned at 100 μm depth intervals. The retained serial sections were designated for DAN positive/negative ionization mode (133 sections, 258,475 pixels in each dataset, 266 sections, 516,950 spectra total) and silver-assisted LDI IMS (130 sections, 323,857 pixels). The first 15 sections of the carotid reconstruction were discarded due to cutting artifacts from calcium deposits, leaving a total length of ~1.18 cm (118 sections, 236,017 pixels). The H&E staining used as the base of alignment for carotid 3D reconstruction was performed directly on the DAN sections.

The entirety of each 3D reconstruction creates large data files with many separate acquisitions. IMS software solutions are limited for multi-sample datasets and 3D datasets. The data was converted to .imzML, a vendor neutral IMS data format, in order to use open-source and command-line capable data analysis tools suitable for multiple sample analysis. In this case, the R package Cardinal loading .imzML data provided simple to use and powerful functions for preprocessing (normalization, peak picking), combination of all data into a common file, and analysis using segmentation by spatially aware shrunken centroids clustering.

*Section alignment for 3D IMS*

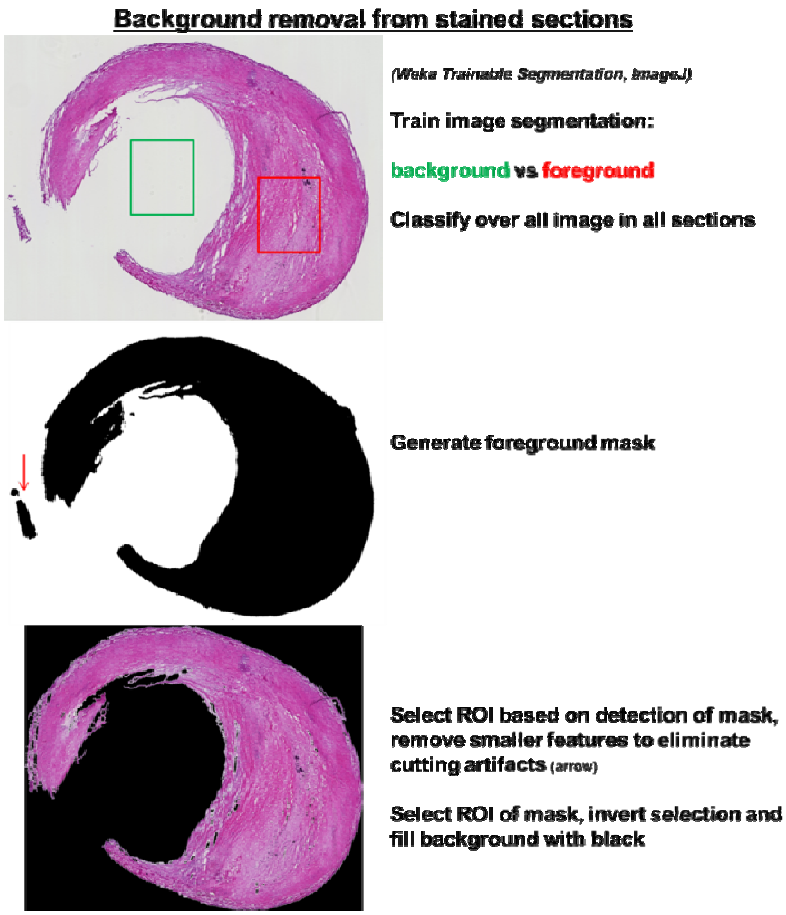


**Chapter 3: Supplemental Methods Figure 3. Background removal of high-resolution slide scans.** 20x slide scans are exported to 1.8 µm/pixel images. Package and software listed in italicized parentheses.

Section alignment is a critical step in visualization of 3D reconstructions. In IMS 3D reconstruction, it is not currently practical to image every section from a tissue block and taking sections for analysis at regular depth intervals is the method most often employed. This method assumes that the histology of the tissue section does not change dramatically between two sections separated by the chosen depth interval. However, this assumption may not hold true for datasets of 3 dimensionally complex samples such as tumors.

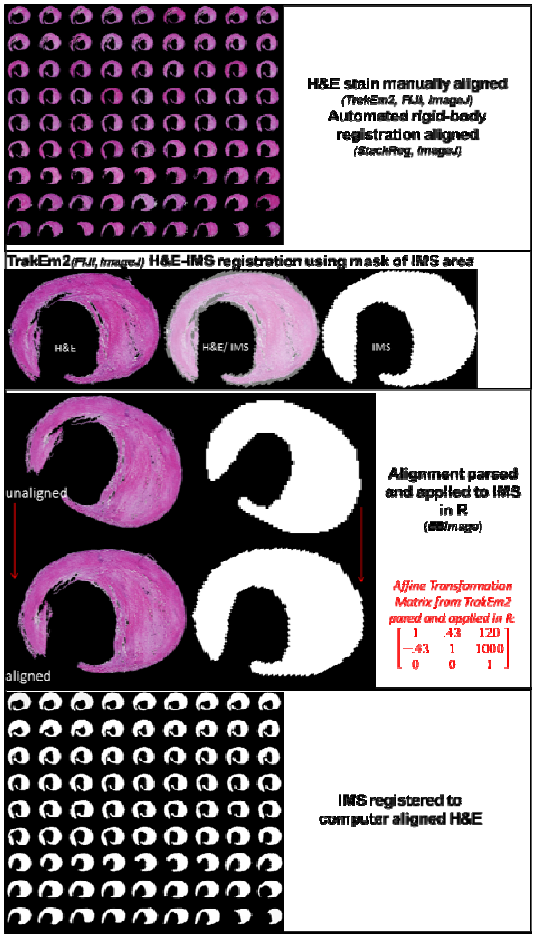


**Chapter 3: Supplemental Methods Figure 4. Alignment of entire IMS data set to histological staining.** Software and package/plugin listed in italicized parentheses.

Due to the use of regular depth intervals, alignment can be frustrating with low resolution IMS data where only gross tissue features are visible and certain tissue patterns are resolution limited. Using a high-resolution scan of a histologically stained section serial to the IMS section or staining of the IMS section itself provides convenient (many highly informative color stainings require less than 10 minutes per slide and are adapted to stain many slides simultaneously) complementary data with greater visual detail for manual alignment. Beyond manual alignment, algorithms for automated registration that propagate through a series of stained images are designed and tested on higher pixel resolution histological staining data. We have used 1.816 µm / pixel (25% reduction of the 20x scan step of the slide scanner employed) RGB staining

data that is first cleared of background using ImageJ's WEKA Trainable Segmentation plugin (Figure 2) then quickly manually aligned using TrakEm2 in FIJI. Finally, the sections having undergone quick manual alignment were computer aligned using a rigid body alignment (x-y translation and rotation) from the StackReg plugin in ImageJ (Figure 3).

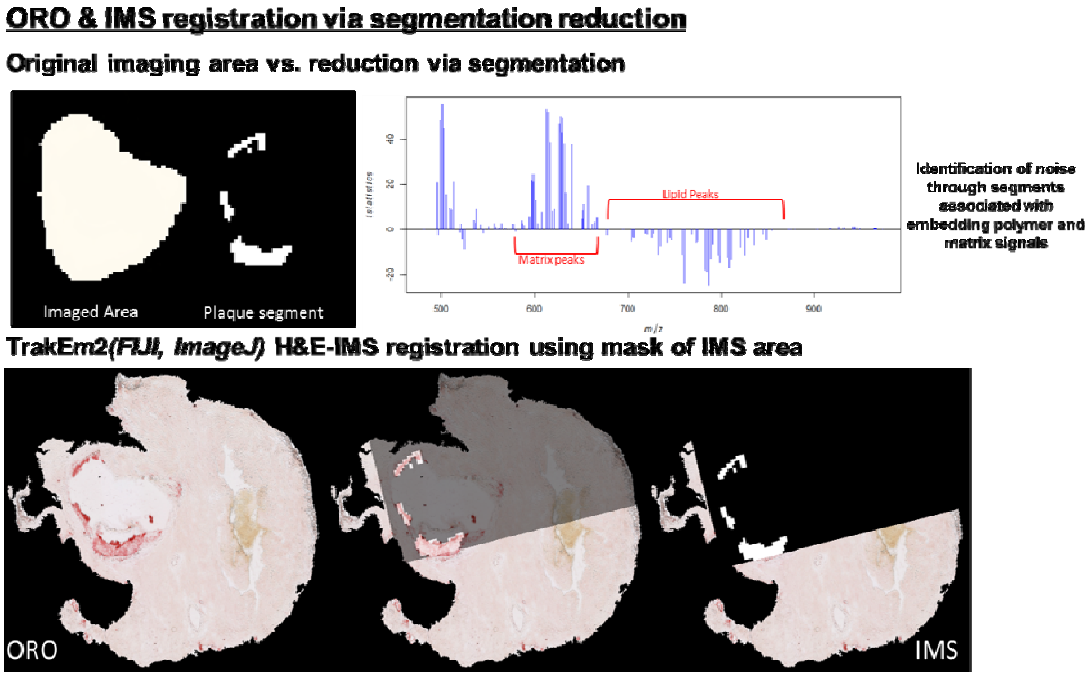


**Chapter 3: Supplemental Methods Figure 5. Alignment for ORO data.** Imaged area is segmented using spatially-aware nearest shrunken centroids clustering to area most closely associated with ORO staining. Noise data and embedding media data is excluded.

Once alignment of the stained sections is completed, IMS data including segmentation and peak data is rescaled to the size of the staining data and is manually registered to the staining data. For the DAN analysis (positive and negative ionization modes) of the human carotid, a mask of the total area imaged was used for registration (Figure 3), whereas the mouse data was registered using a mask of the spatially aware nearest shrunken centroids segmentations observed to most closely resemble the red color of the ORO staining (plaque) (Figure 4). Importantly, mouse data included IMS coordinates within the aorta that yielded only noise,

segmentation of the entire dataset together and reduction to only the plaque area removes non-relevant pixels without error-prone and cumbersome manual selection. Removal of non-relevant or incomplete regions in 3D is an important aspect as the interested researcher may only target certain histologies for 3D reconstruction. Our results prove the basic molecular histology of the section is robust enough to reduce the dataset to its most important features. The human plaque sample did not necessitate a reduction as the images included few noise/polymer signals around the tissue area. The silver assisted LDI IMS data from the human carotid was registered to the aligned H&E data for 3D reconstruction.

# Supplemental figures for Chapter 3

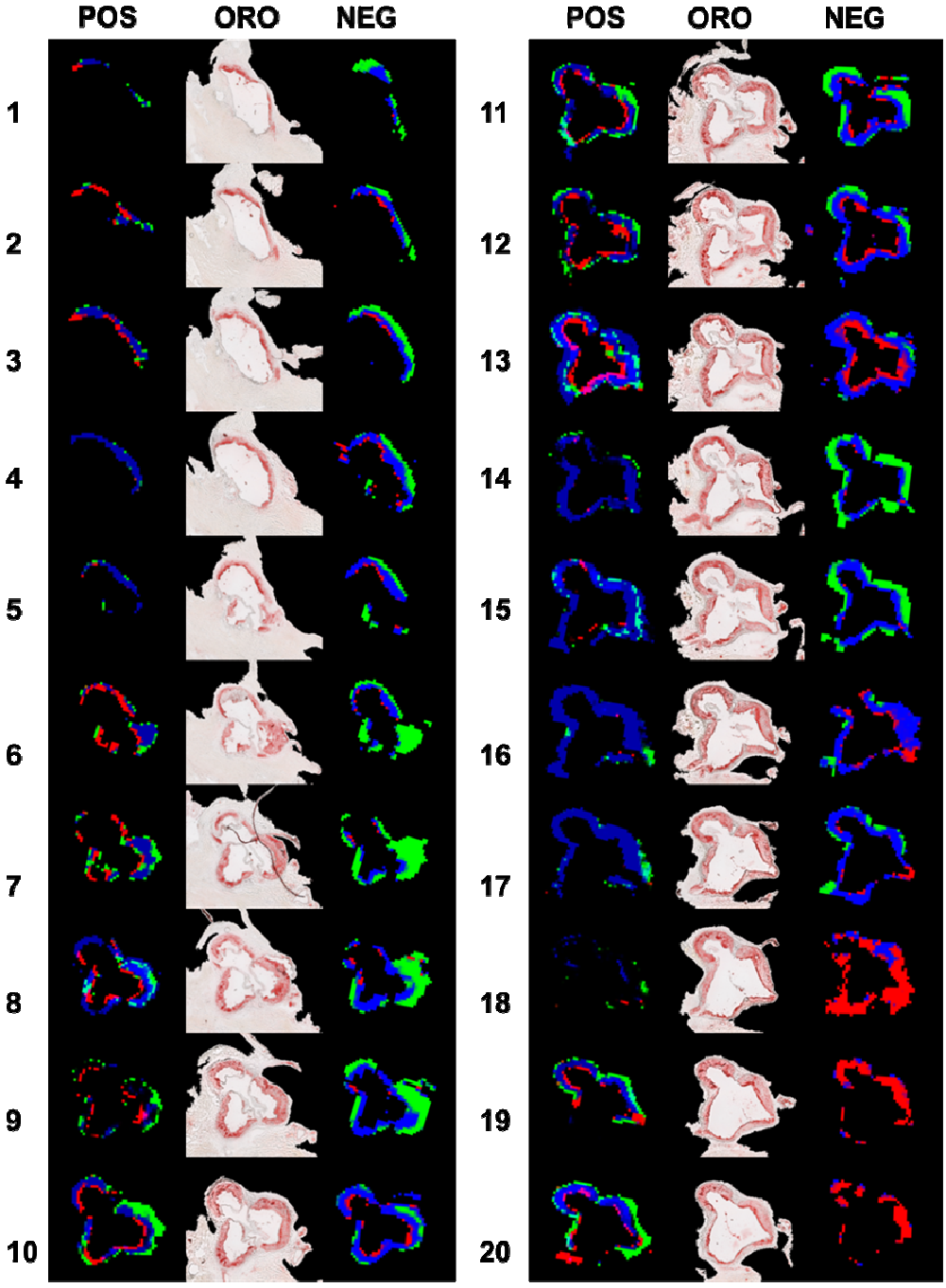


**Chapter 3: Supplemental Figure 1. Positive and negative ionization DAN IMS data spatially aware shrunken centroids segmentation (k=3) of the mouse heart aorta plaque.**

Middle row contains ORO staining data from serial sections at the depth imaged.

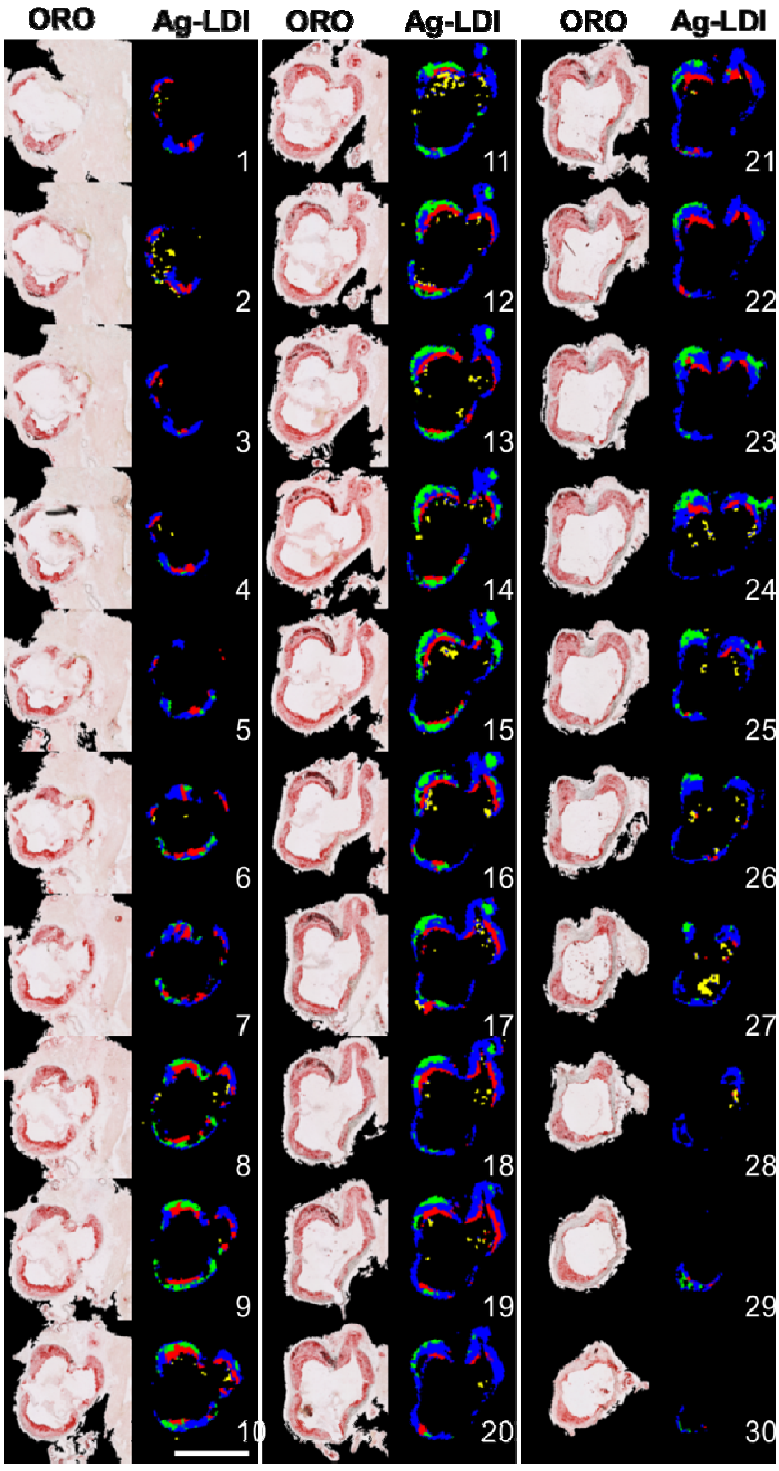


**Chapter 3: Supplemental Figure 2. Silver-assisted LDI IMS data spatially aware shrunken centroids segmentation (k=4) of the mouse heart aorta plaque.** Leftmost rows contain ORO staining data from serial sections at the depth imaged. Scale bar: 1 mm.

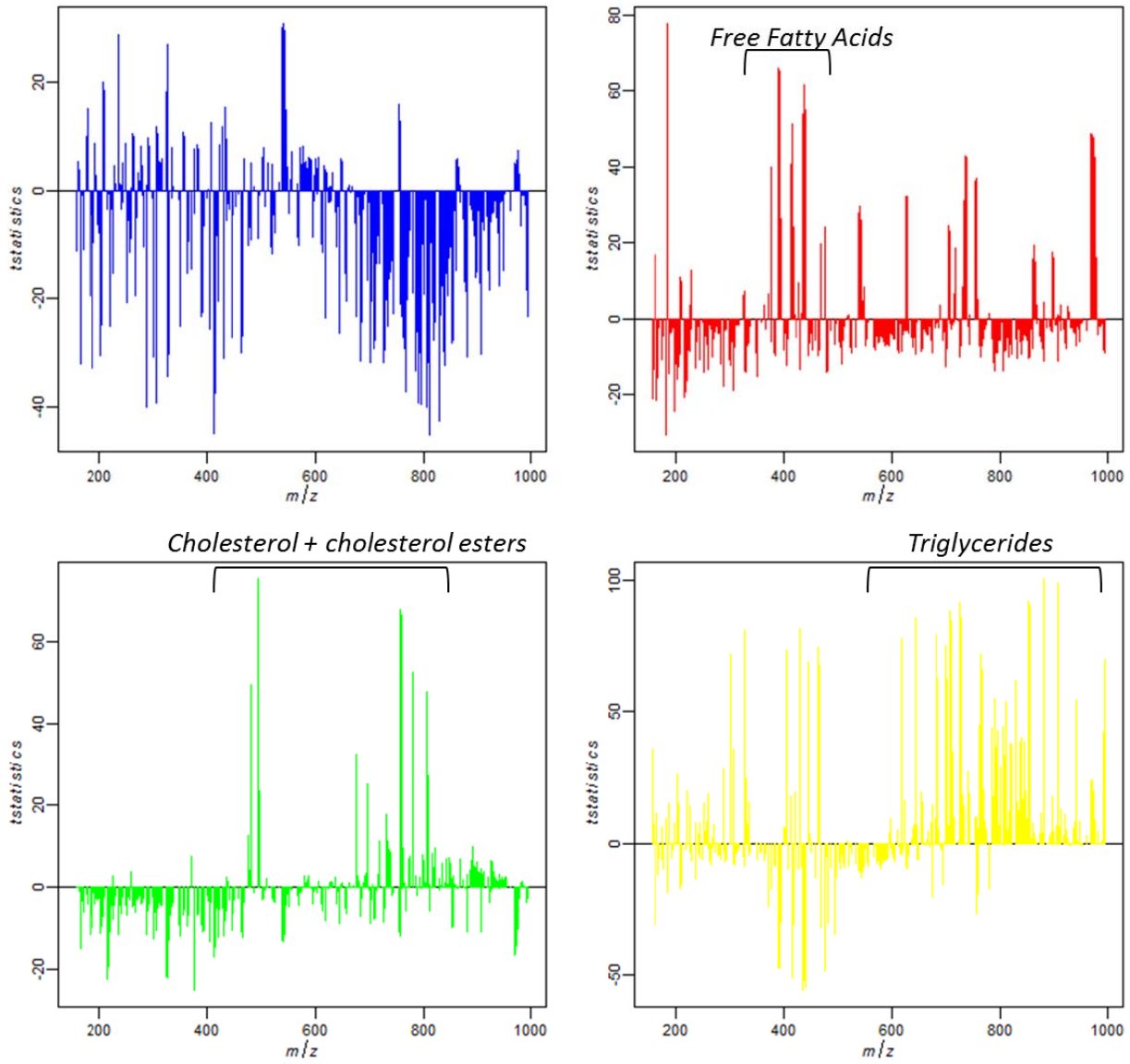


**Chapter 3: Supplemental Figure 3. T-statistics** of **silver-assisted LDI IMS data spatially aware shrunken centroids segmentation (k=4) of the mouse heart aorta plaque.** Positive values indicate association to the segmentation, negative to an anti-correlation to the segmentation. Regional signals are highlighted.

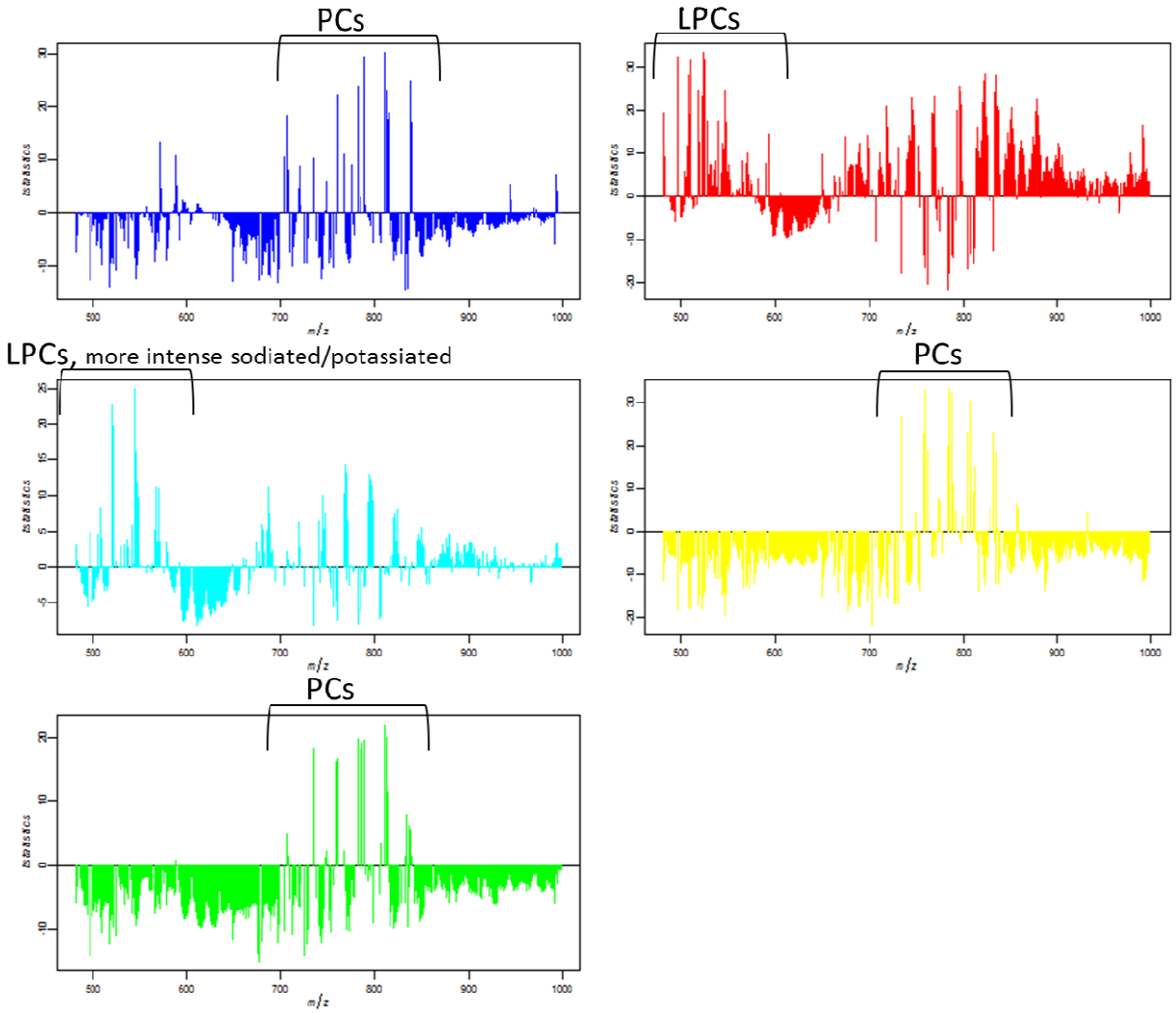


**Chapter 3: Supplemental Figure 4. T-statistics of DAN positive IMS data spatially aware shrunken centroids segmentation (k=8) of the carotid atherosclerotic plaque.** Positive values indicate association to the segmentation, negative to an anti-correlation to the segmentation. Regional signals are highlighted.

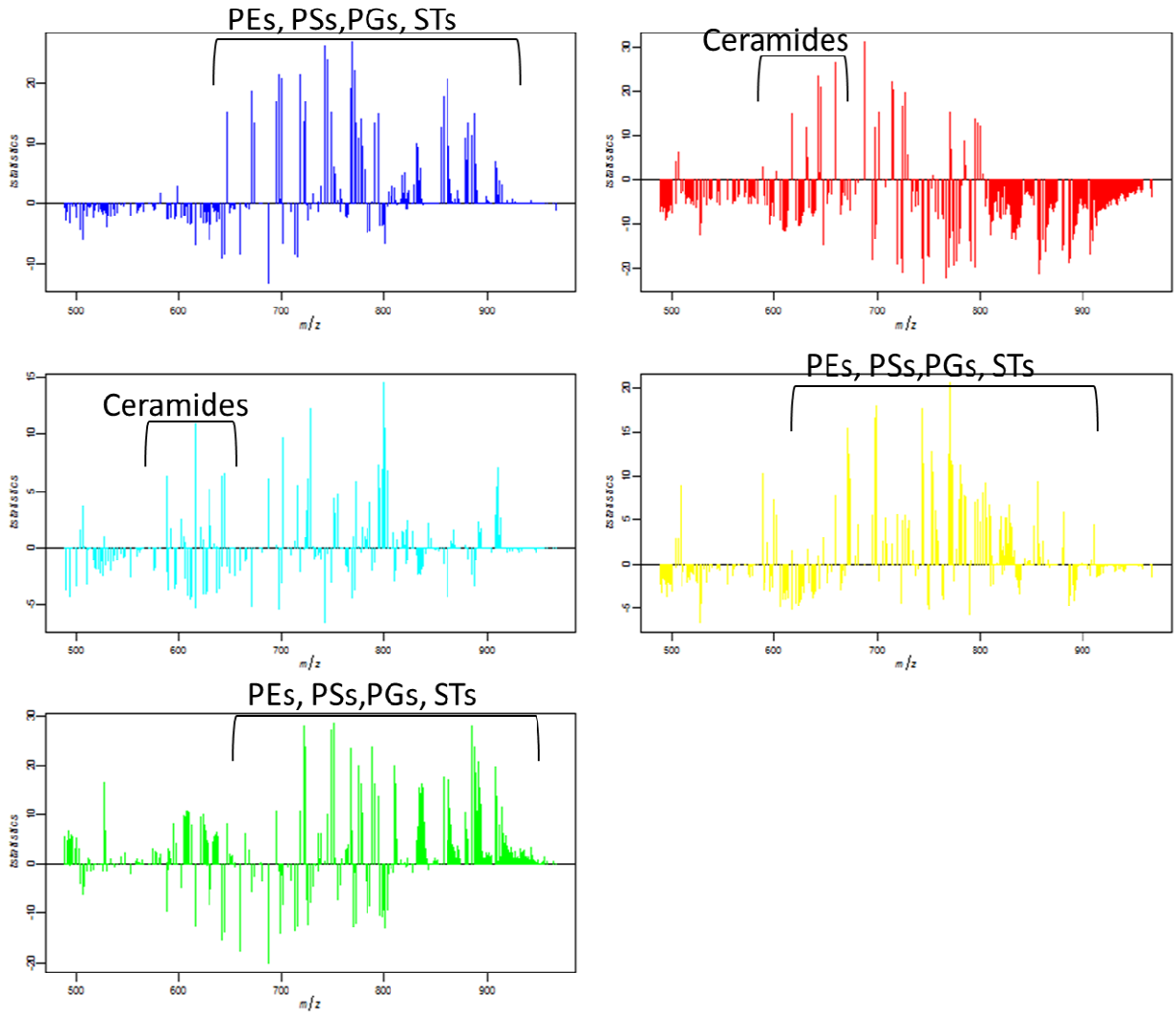


**Chapter 3: Supplemental Figure 5. T-statistics** of **DAN negative IMS data spatially aware shrunken centroids segmentation (k=8) of the carotid atherosclerotic plaque.** Positive values indicate association to the segmentation, negative to an anti-correlation to the segmentation. Regional signals are highlighted. Negative data tends be a mixture of phospholipid classes across the typical mass range.

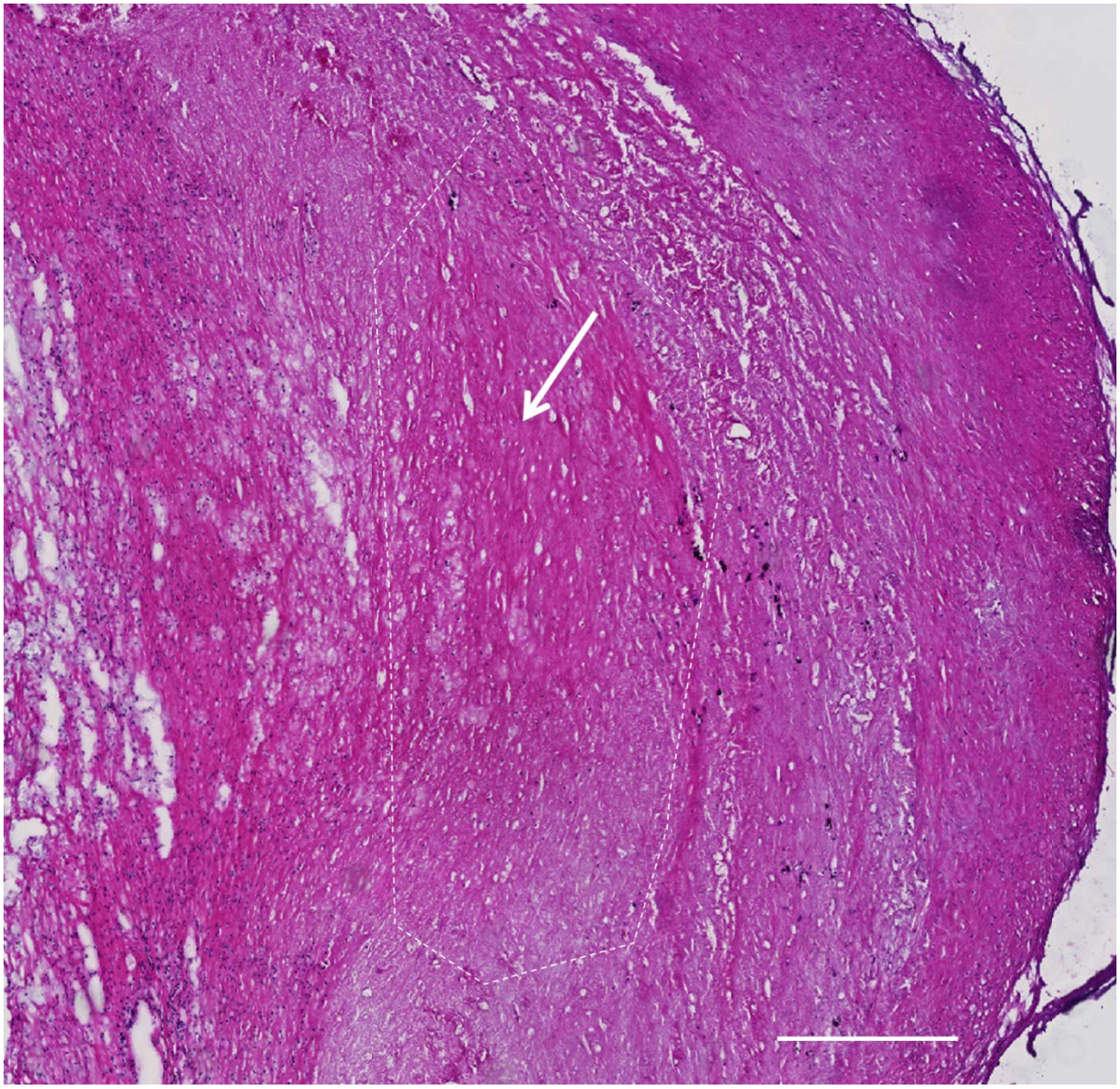

**Chapter 3: Supplemental Figure 6. Zoomed H&E region highlighting dense LPC ion image area.** Arrows point to the central area shown in Fig 4, bottom left. Scale bar: 0.5 mm.

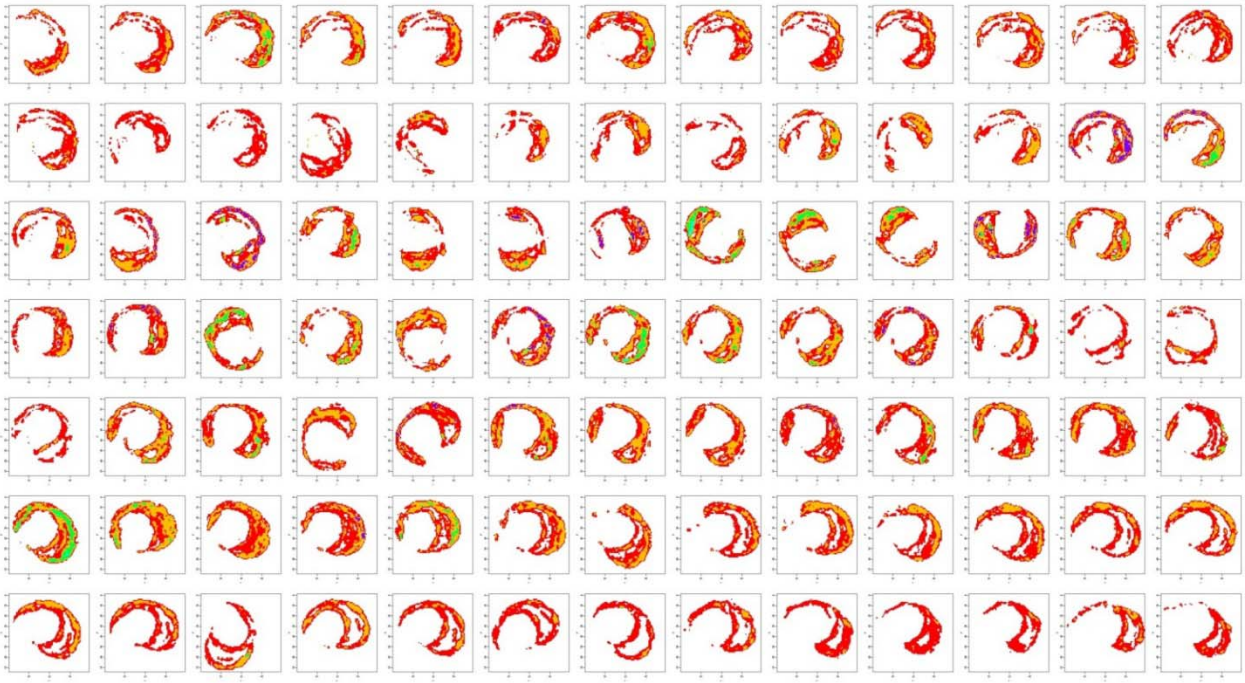

**Chapter 3: Supplemental Figure 7. Unaligned silver data.** Segmentation (k=8) shows inconsistent 3D features.

# Supplemental tables and figures for Chapter 4

| | Training Set | Validation Set |
|---|---|---|
| **Demographics** | | |
| Gender, number of patients (%) | | |
| Male | 5 (41.7) | 26 (68.4) |
| Female | 7 (58.3) | 12 (31.5) |
| Age, median (range) | 62.7 (31-81) | 63.2 (40-81) |
| **Features of the primary tumour** | | |
| Site of primary tumour, number of patients (%) | | |
| Rectum | 4 (33.3) | 14 (36.8) |
| Recto-sigmoid | 4 (33.3) | 5 (13.15) |
| Colon | 4 (33.3) | 11(28.9) |
| Stage of Primary Disease (TNM), number of patients (%) | | |
| T1 | 0 (0) | 1 (2.6) |
| T2 | 0 (0) | 2 (5.2) |
| T3 | 7 (58.3) | 20 (52.6) |
| T4 | 4 (33.3) | 4 (10.4) |
| unknown | 1 (8.3) | 11 (28.9) |
| Lymph node status, number of patients (%) | | |
| No | 3 (25) | 8 (21) |
| N1 | 6 (50) | 10 (26.3) |
| N2 | 2 (16.6) | 7 (18.4) |
| Unknown | 1 (8.3) | 13 (34.2) |
| **Baseline features of the liver metastases** | | |
| Timing of presentation, number of patients (%) | | |
| Synchronous | 12 (100) | 21 (52.5) |
| Metachronous | 0 (0) | 19 (47.5) |
| No. of liver lesions at presentation, number of patients (%) | | |
| Solitary lesion | 7(58.8) | 16(40) |
| Multiple lesions | 5(41.6) | 20(50) |
| Baseline lesion size, median (range)cm | 4.75(0.3-9.2) | 3.34(0.8-10) |
| **Treatment of the liver metastases** | | |
| Preoperative therapy, number of patients (%) | | |
| Chemonaive | 3 (25) | 14 (35) |
| Chemotherapy + bevacizumab | 9 (75) | 26 (65) |

**Chapter 4: Supplemental Table 1. Baseline characteristics of training set (n=12) and validation set (n=40).** NOTE: Validation set consists of 40 lesions from 38 patients, 2 patients underwent staged resection.

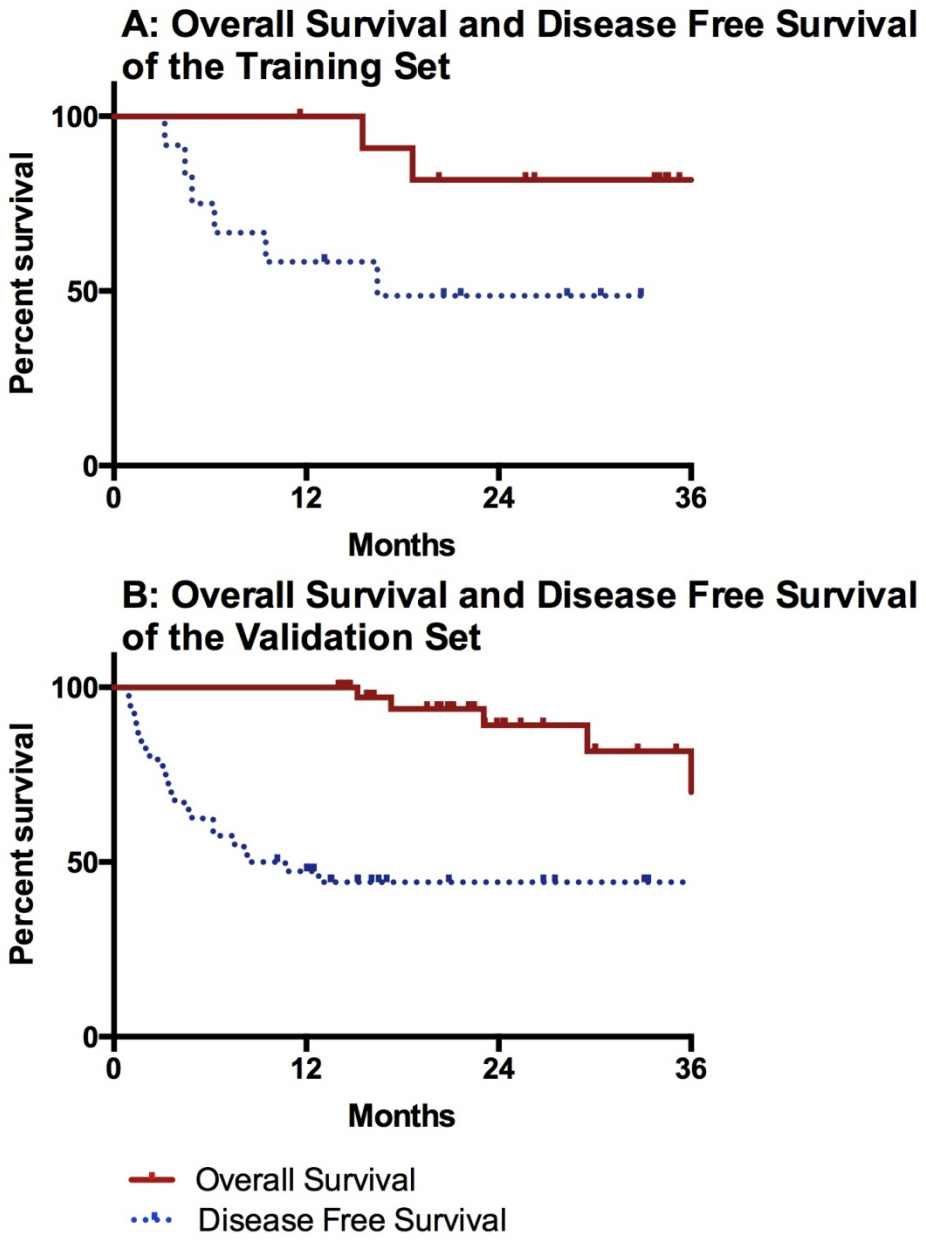


**Chapter 4: Supplemental Figure 1**. **Overall Survival (OS) and Disease Free Survival (DFS).** **A** Training Set: estimated 1-year and 3-year OS were observed at 100% and 81.8% respectively. Estimated 1-year and 3-year DFS were observed at 58.3% and 48.6% respectively. **B** Validation set: estimated 1-year and 3-year OS were observed at 100% and 81.6% respectively. Estimated 1-year and 3-year DFS were observed at 47.3% and 44.2% respectively.

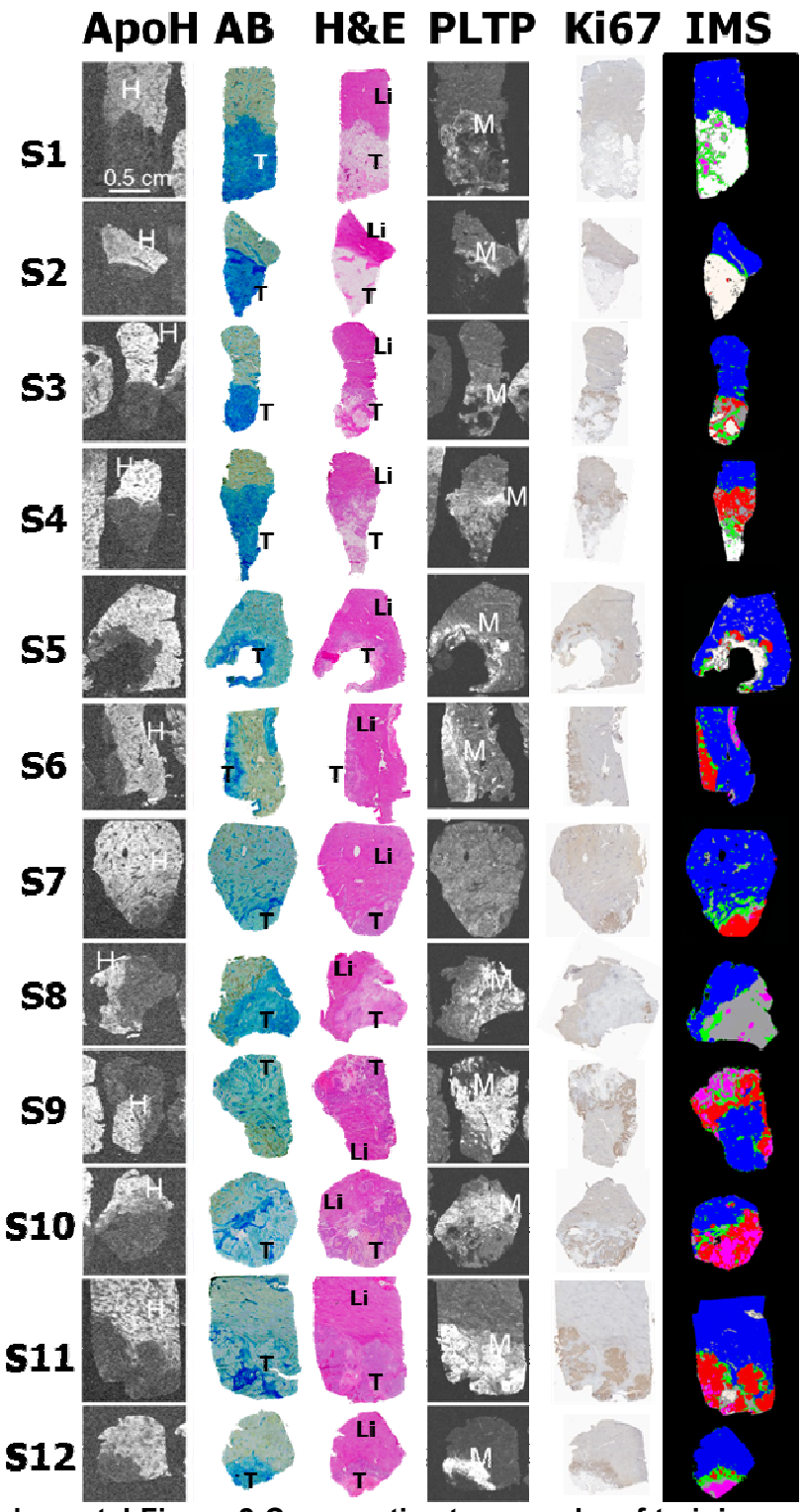


**Chapter 4: Supplemental Figure 2 Comparative topography of training set representative CRCLM resections.** Column 1: x-ray film auto-radiography showing ApoF mRNA hepatocyte-specific in situ hybridization labeling. Column 2: Alcian Blue (AB) staining pattern in tumor

tissue. Column 3: tissue topography with H&E staining. Column 4: x-ray film auto-radiography with macrophage-preferential PLTP mRNA in situ hybridization labeling. Column 5: Hyper-spectral *k-means* clustering Imaging Mass Spectrometry (IMS) data. Abbreviations: H – hepatocyte; Li – liver; M – macrophage; S – selection and T – tumor. Magnification x5.

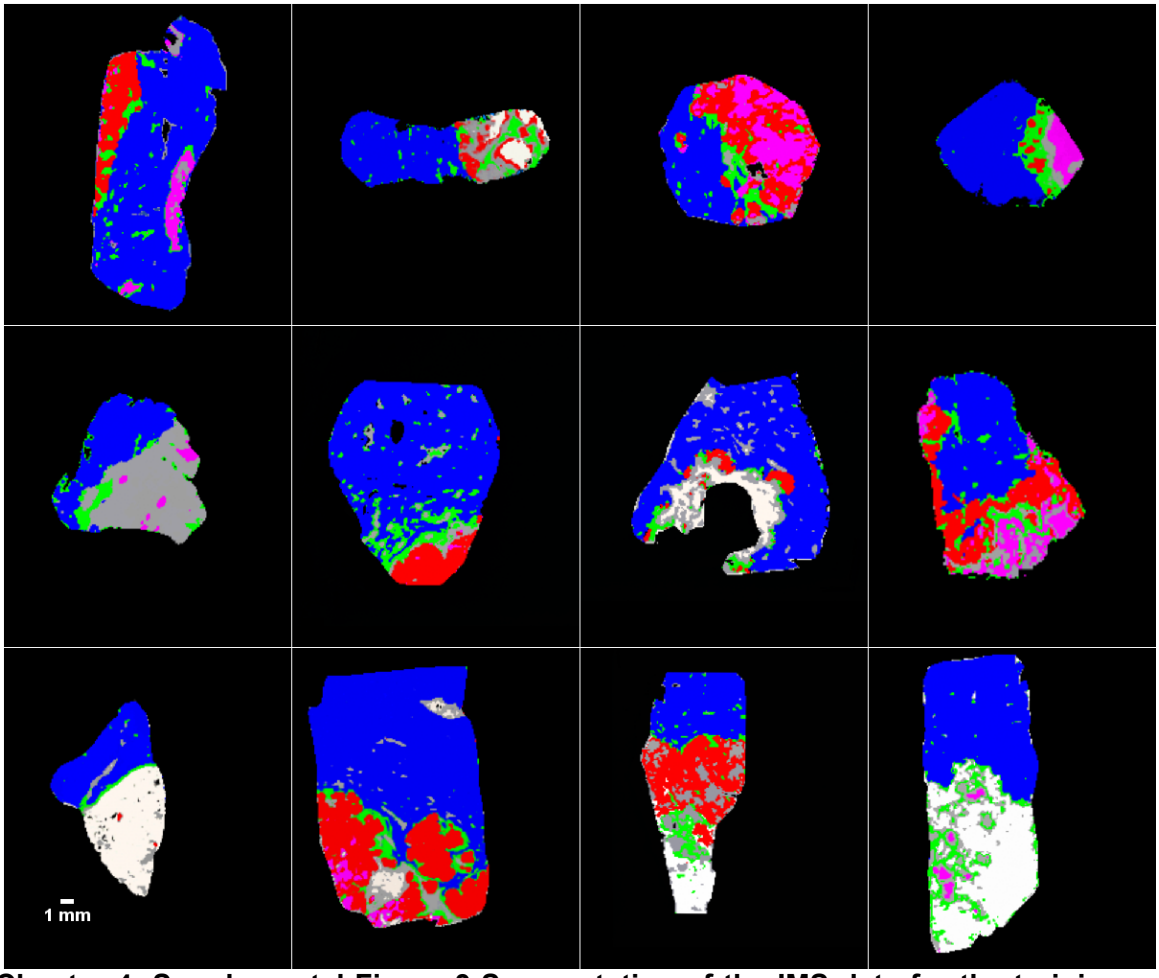


**Chapter 4: Supplemental Figure 3 Segmentation of the IMS data for the training set.** The colors blue, red, purple, green, grey and white represent normal liver, viable tumor, necrosis, inflammation, fibrosis, and mucinous/empty/noise areas in and outside the tumor area, respectively.

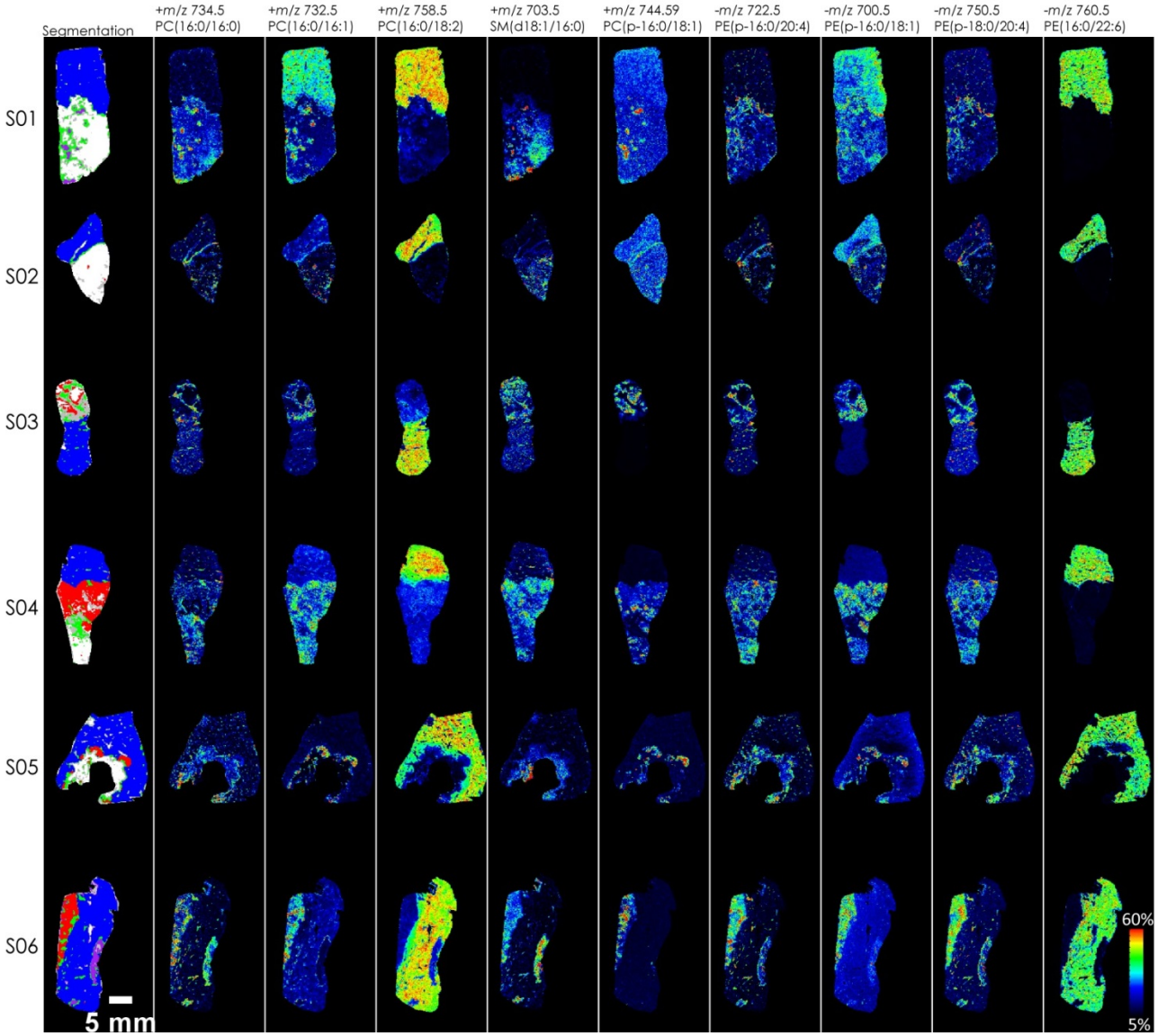


**Chapter 4: Supplemental Figure 4. Subset of ion images of discriminant ions in training set**.

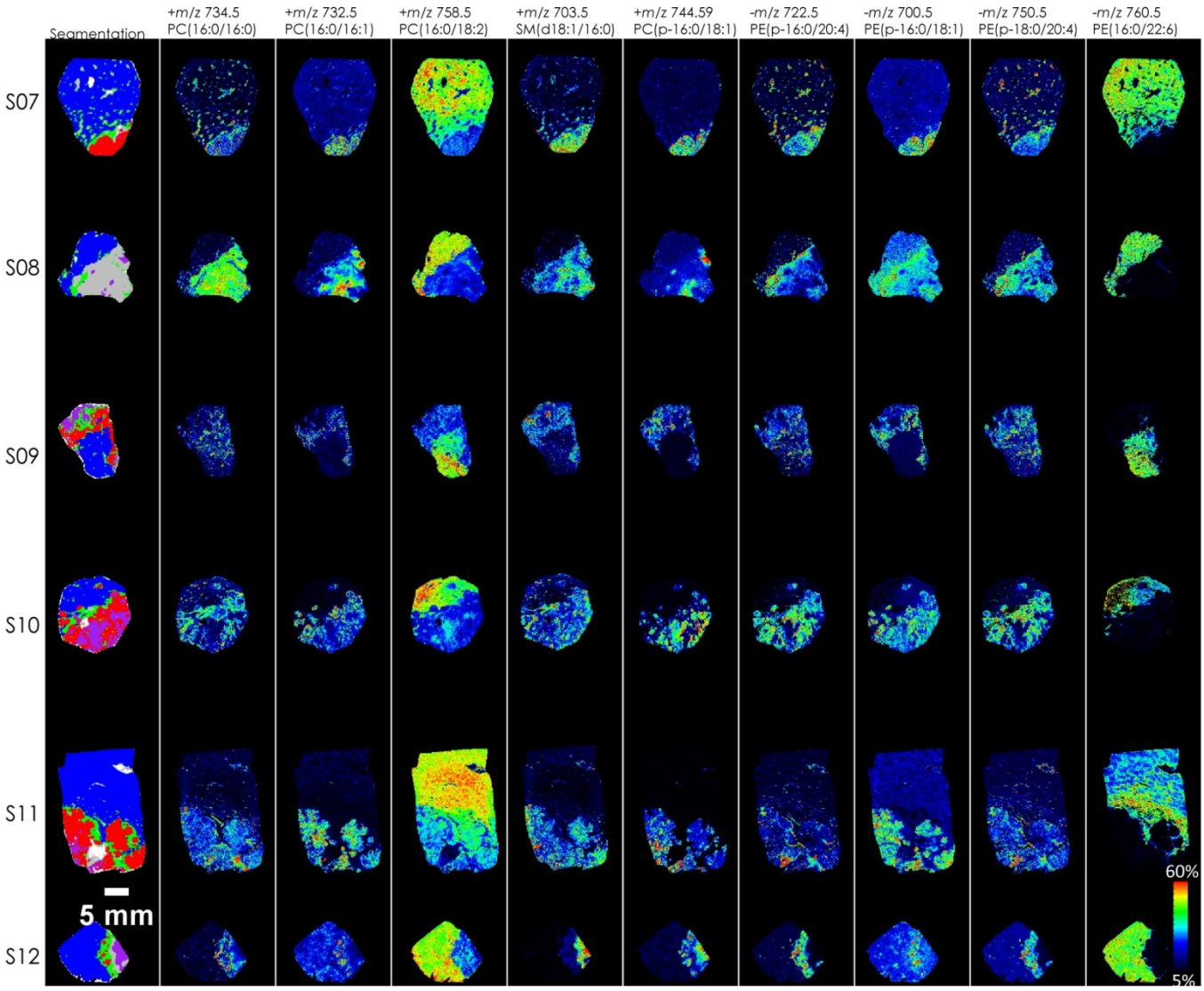


**Subset of ion images of discriminant ions in training set.**

**Chapter 4: Supplemental Figure 5. MS/MS of most discrimiant markers.**

Fatty acid side chain length and number of unsaturations are given, however, side chain position at either *sn-1* or *sn-2* is not known.

**I. Adjacent "Normal" Liver, Negative mode, *m/z* 738.62, PE(16:0/20:4)**

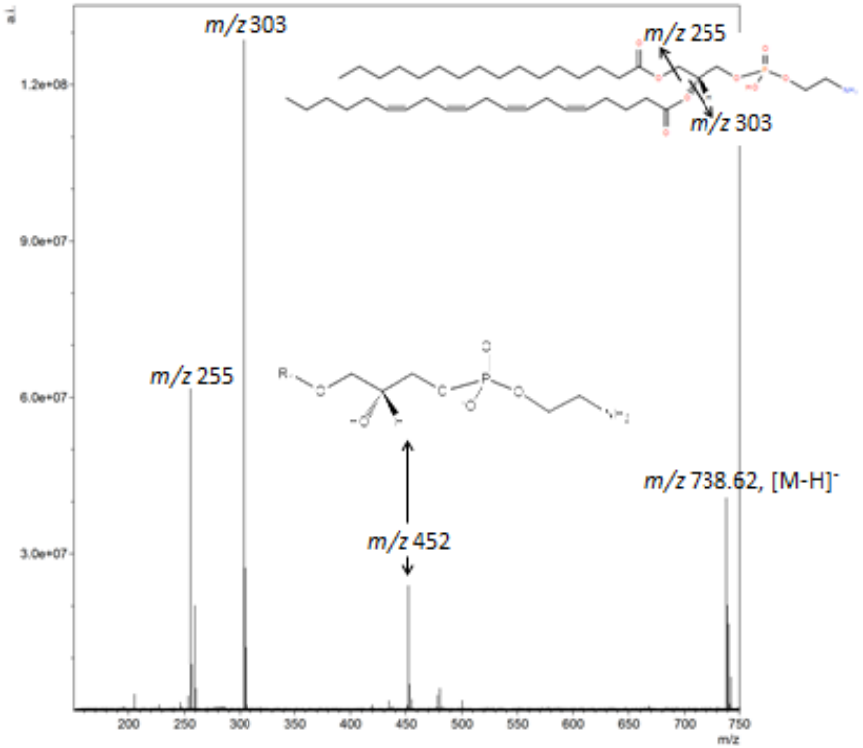


**II. Adjacent "Normal" Liver, Negative mode, *m/z* 762.55, PE(16:0/20:4)**

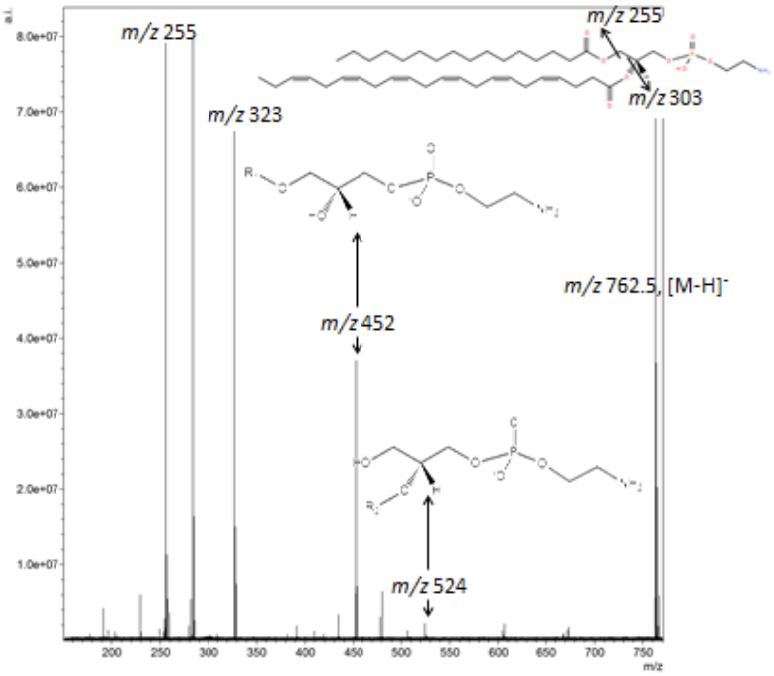


**III. Adjacent "Normal" Liver, Negative mode, *m/z* 885.56, PI(18:0/20:4)**

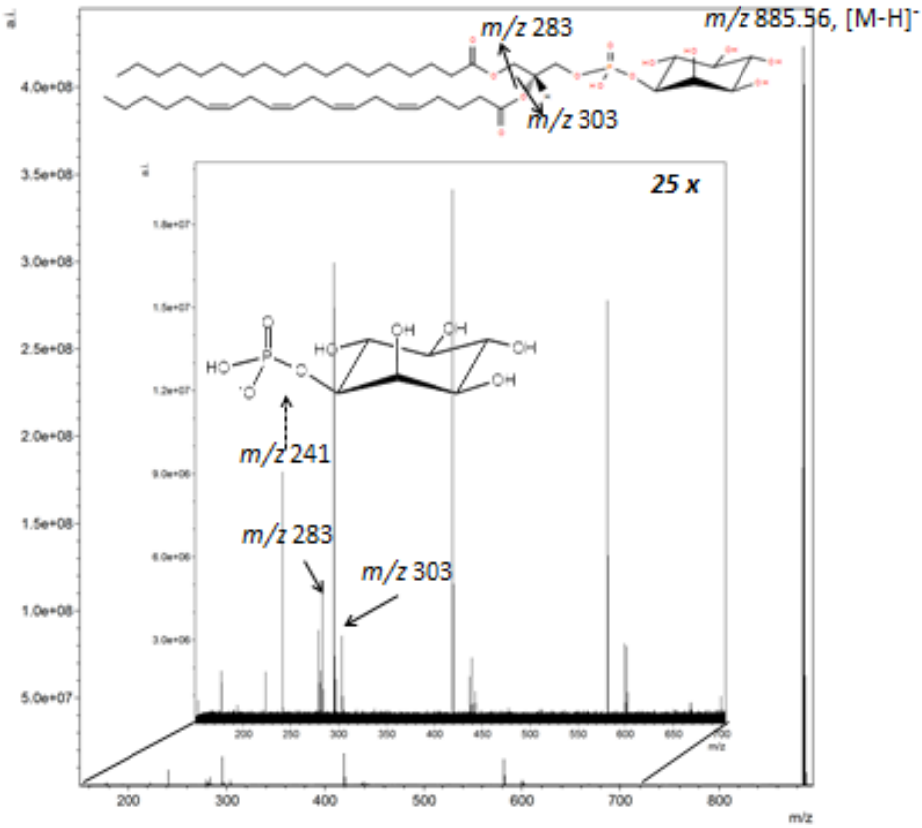


**IV. Adjacent "Normal" Liver, Positive mode, *m/z* 758.57, PC(16:0/18:2)**

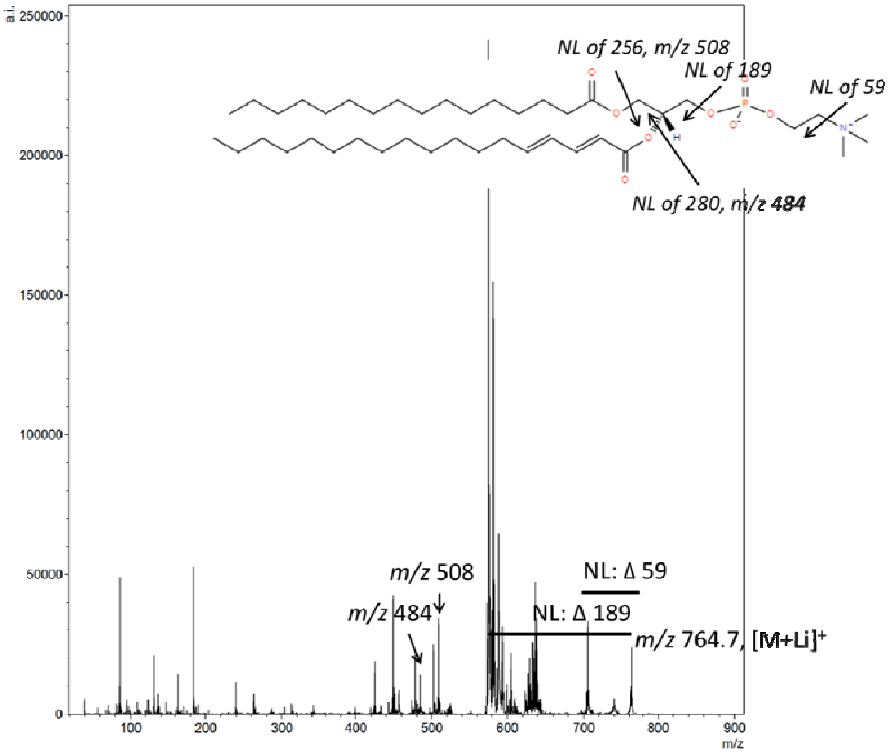


**V. Viable Tumor, Negative mode, *m/z* 698.48, PE(p-16:0/18:2)**

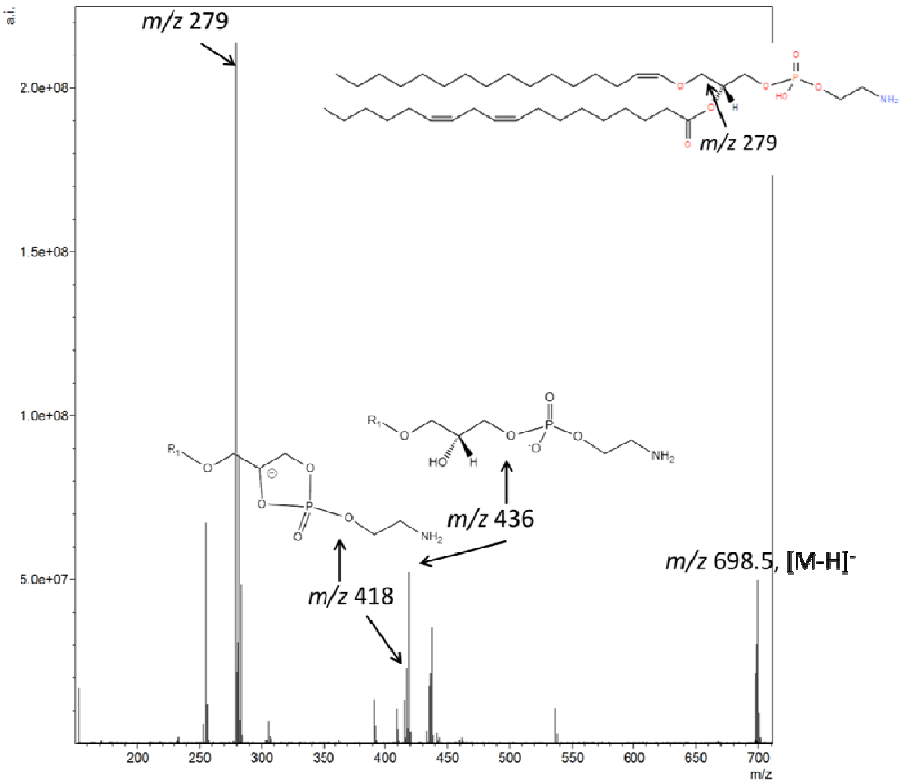


**VI. Viable Tumor, Negative mode, *m/z* 700.51, PE(p-16:0/18:1)**

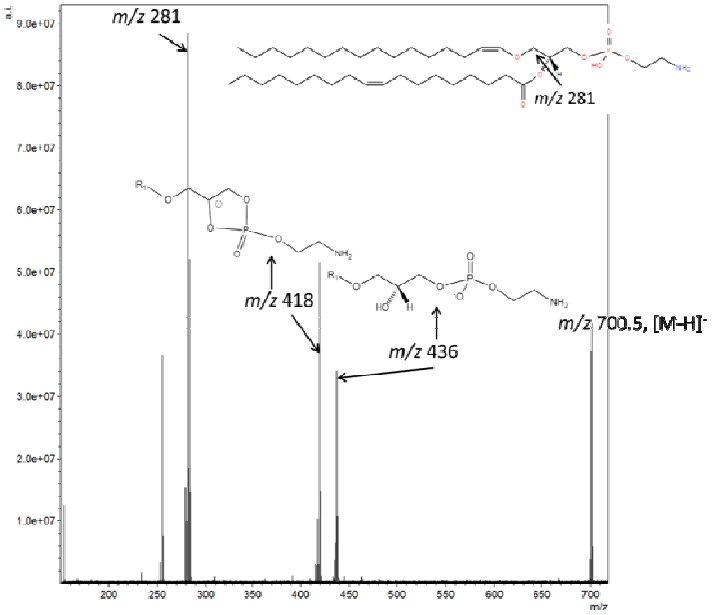


**VII. Viable Tumor, Negative mode, *m/z* 835.51, PE(p-16:0/18:1)**

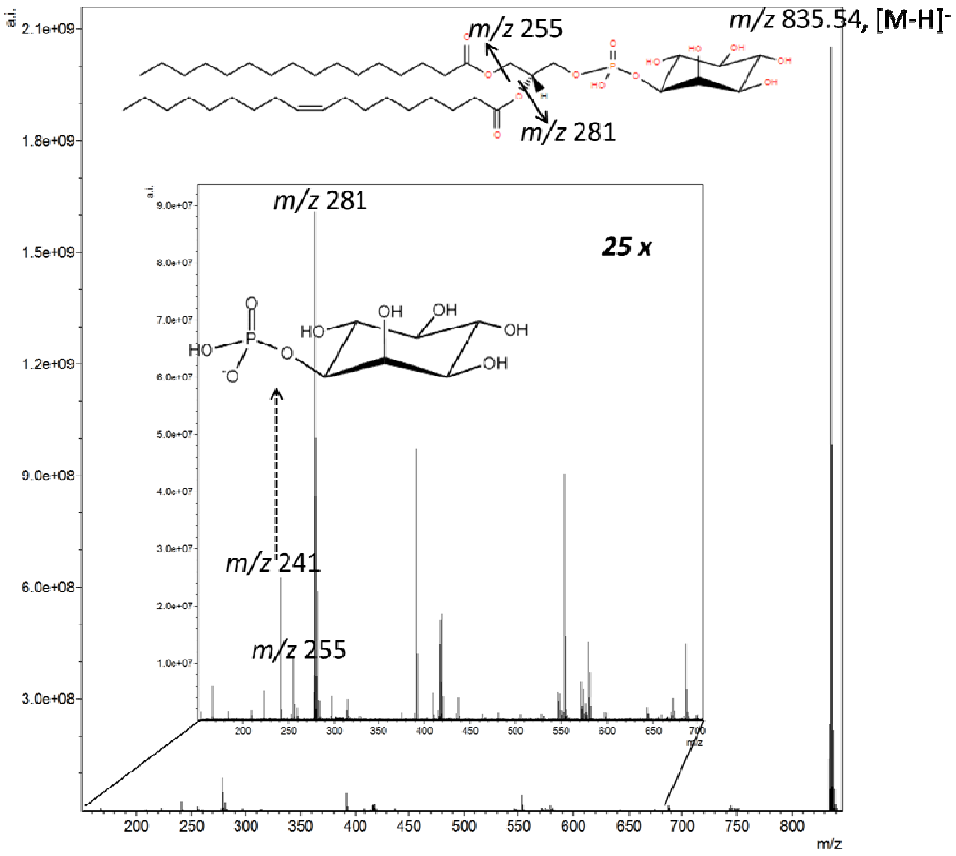


**VIII. Viable Tumor, Positive mode, *m/z* 706.55, PC(14:0/16:0) : Identified through LIPIDMAPS on exact mass**

**IX. Viable Tumor, Positive mode, *m/z* 732.54, PC(16:0/16:1)**

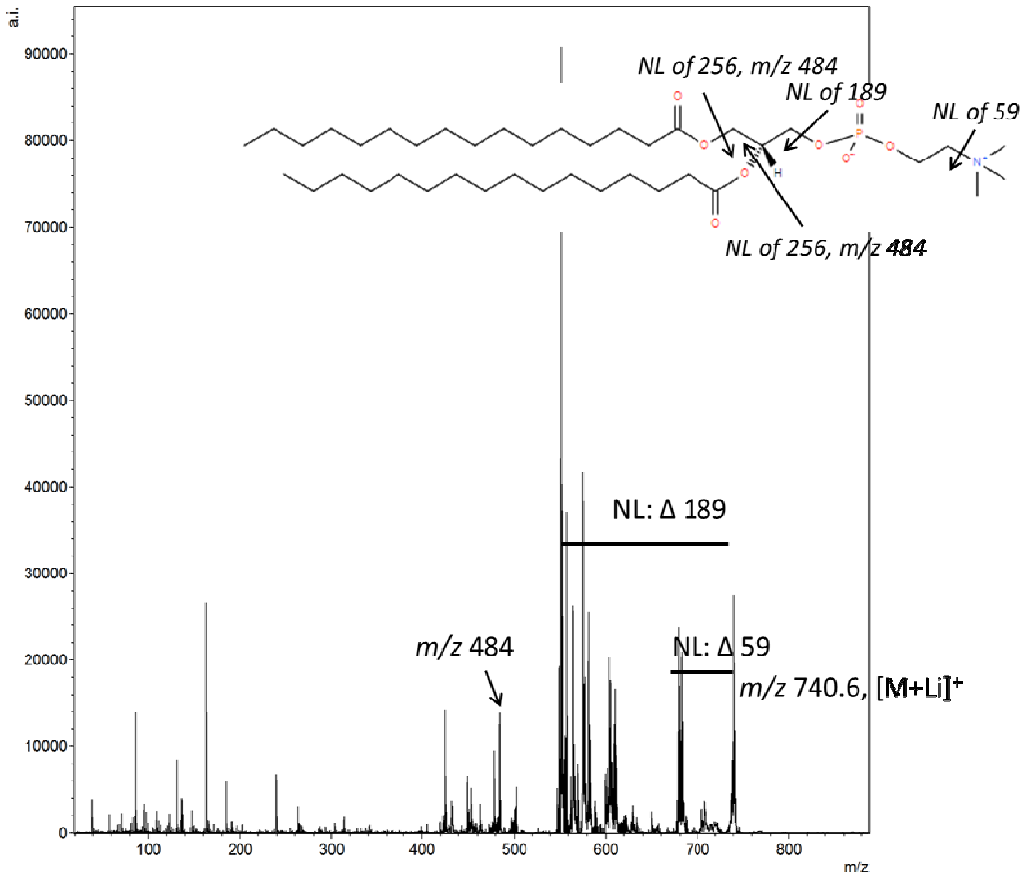


**X. Inflammation, Negative Mode, *m/z* 722.49, PE(p-16:0/ 20:4)**

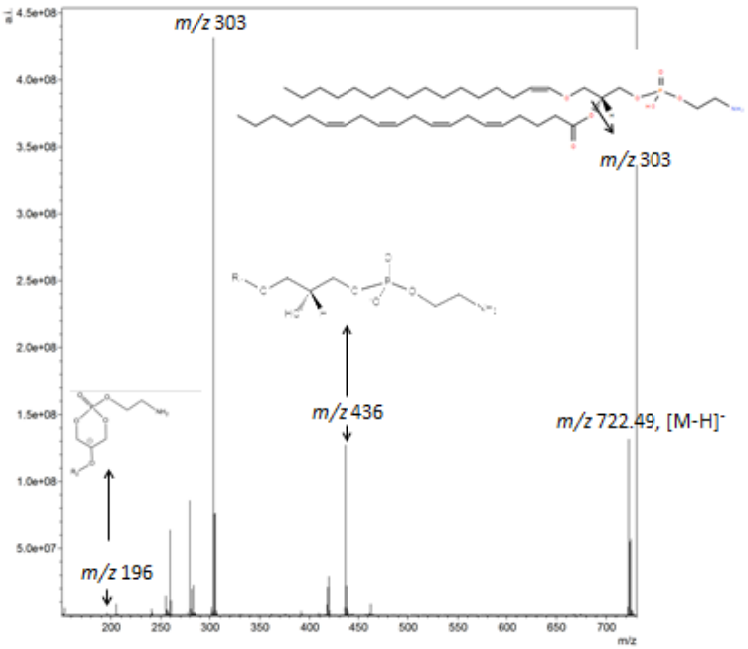

**XI. Inflammation, Negative Mode, *m/z* 750.53, PE(p-18:0/ 20:4)**

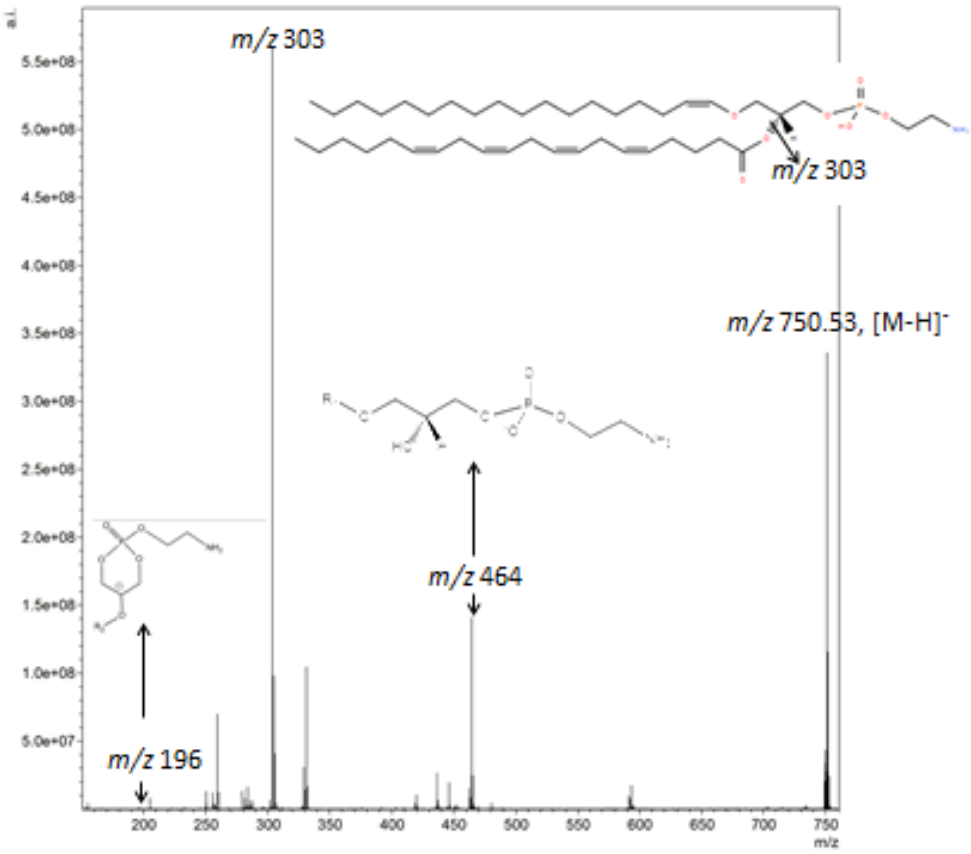


**XII. Inflammation, Positive Mode, *m/z* 734.57, PC(16:0/ 16:0)**

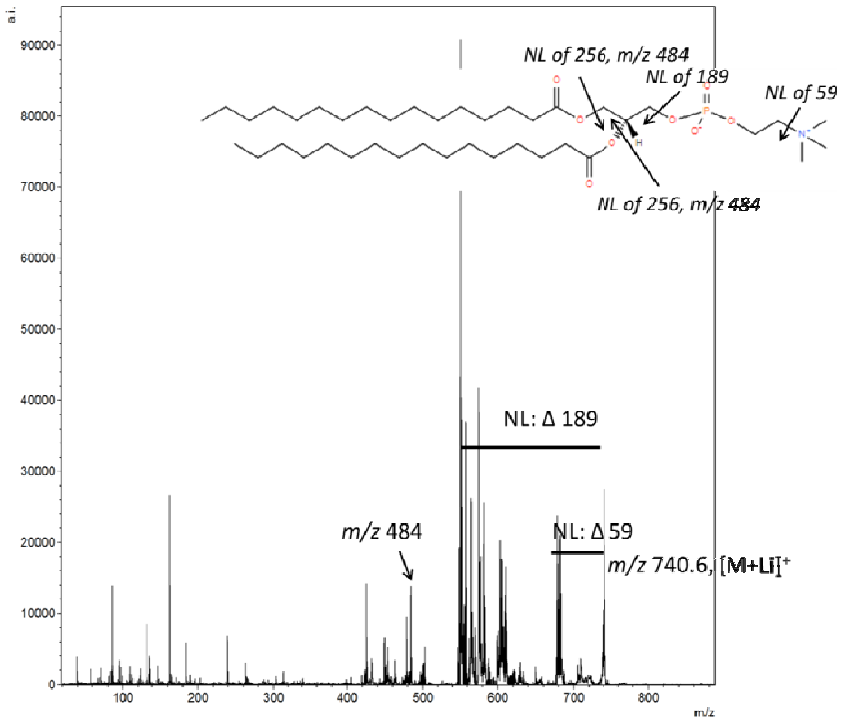

## XIII. Necrosis, Positive Mode, *m/z* 703.57, SM(d18:1/16:0)

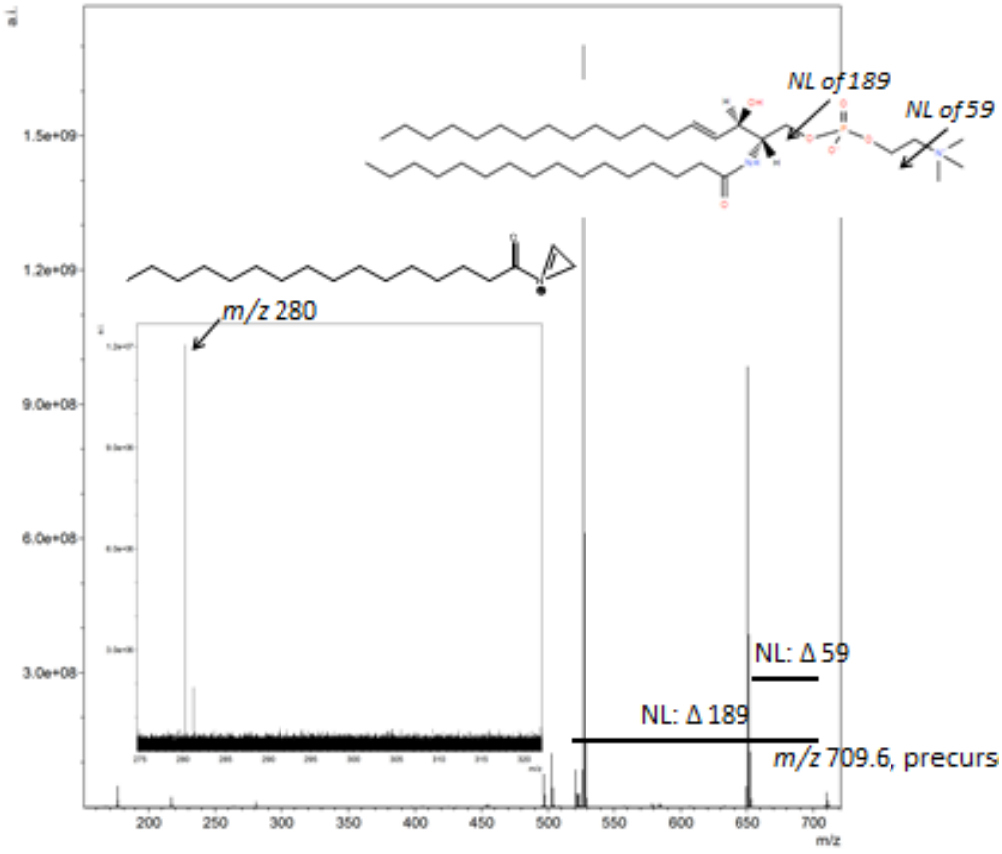

**Chapter 4: Supplemental Figure 6. Profiling and lithiated MS/MS of ions co-localized in areas of CRCLM usual necrosis.**

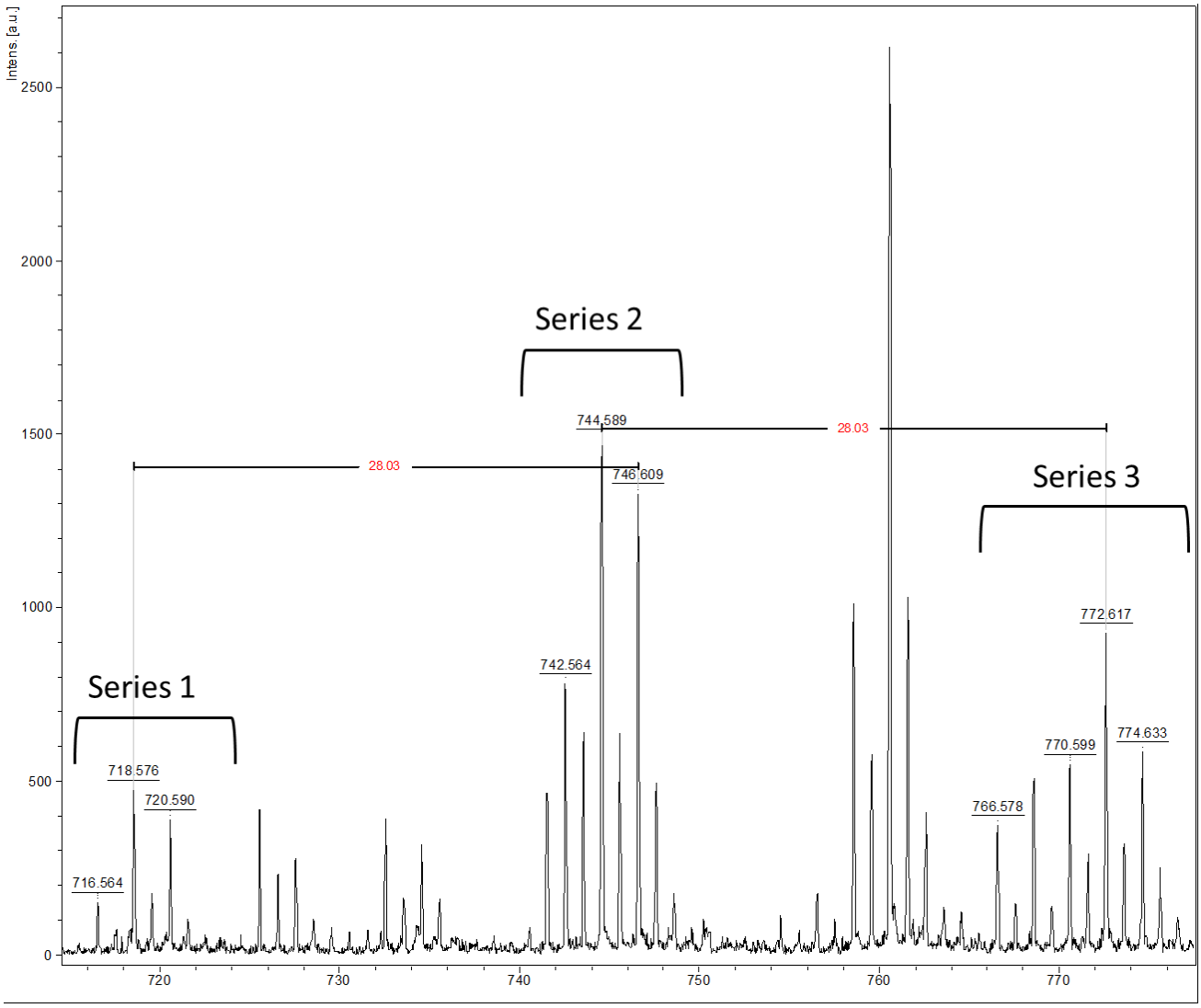


Profile of the three plasmalogen series. Annotations added for 28 Da FA chain elongations between series

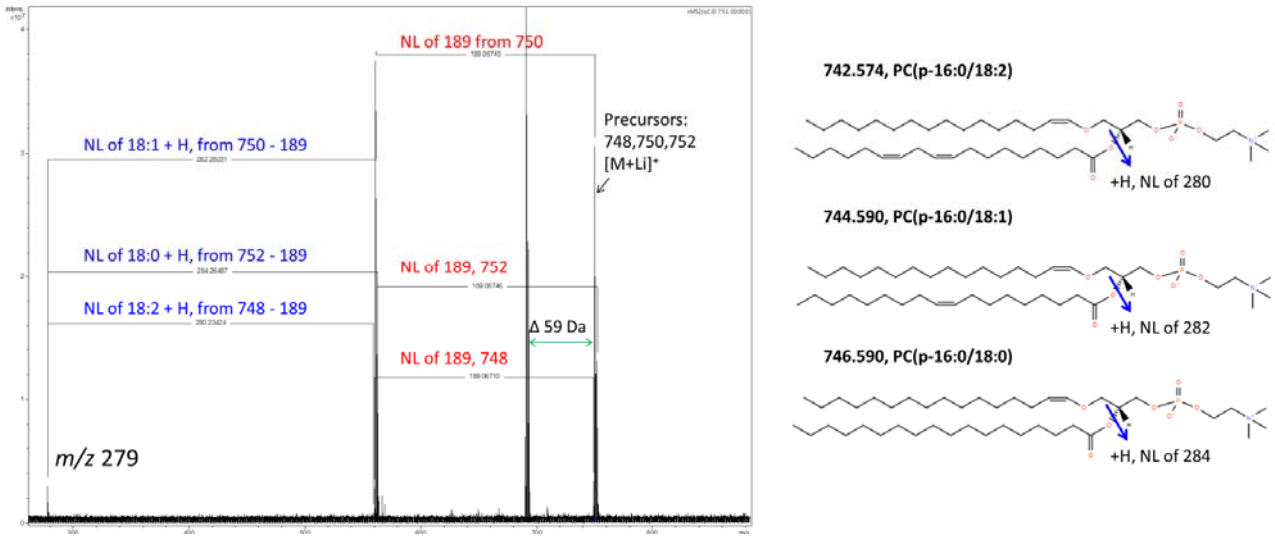


MS/MS of Series 2, isolation window 747.5-753.5. Three precursor ions.

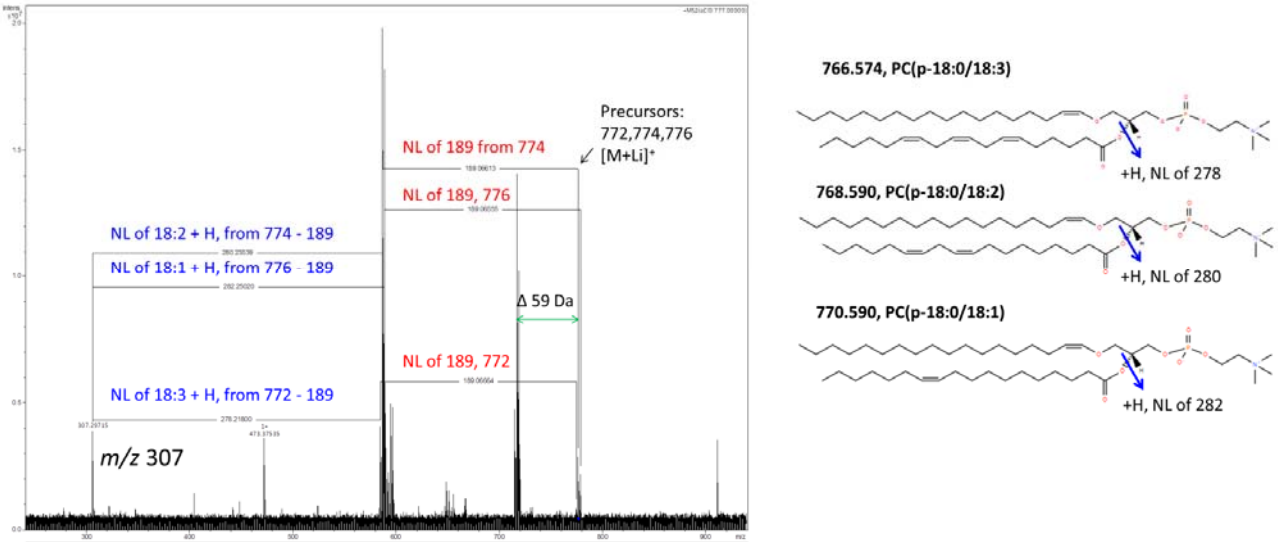


MS/MS of Series 3, isolation window 771.5-777.5. Three precursor ions.

**Chapter 4: Supplemental Figure 7 MS/MS of ceramide species co-localized in areas of CRCLM UN (C16 Ceramide) and ILN(Cer-1-P):**

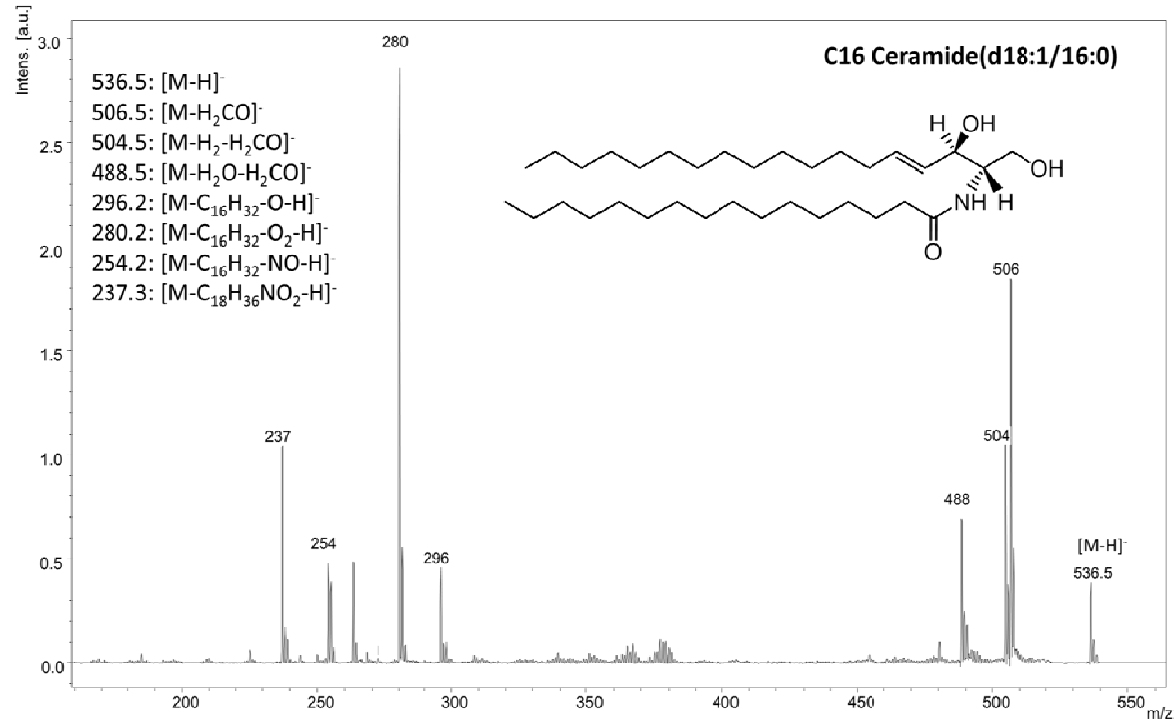


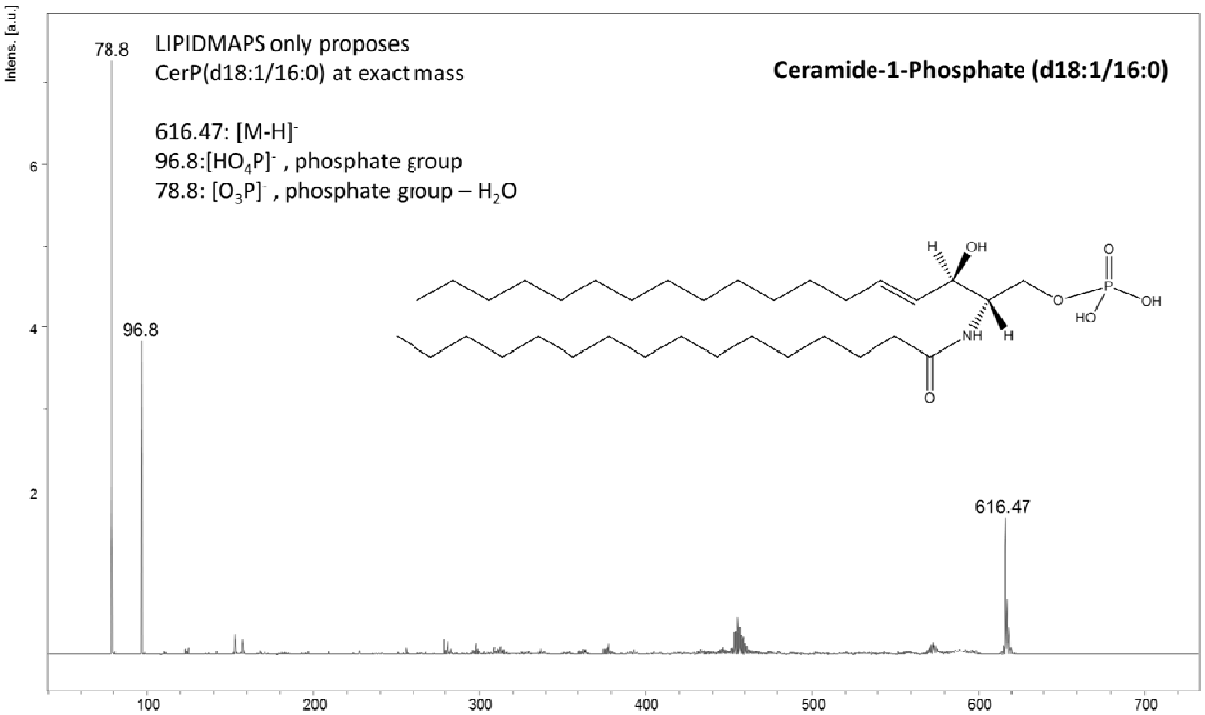


**This MS/MS identifies primarily the very labile phosphate grou. For this mass, Cer-1-P is the only entry in LIPIDMAPS and the Human Metabolome Database**

**Chapter 4: Supplemental Table 2.Pathologists and IMS mTRG gradings for all samples.**

| serial no. | Path1 | Path2 | IMS |
|---|---|---|---|
| 1 | 1 | 2 | 1 |
| 2 | 2 | 2 | 2 |
| 3 | 3 | 3 | 3 |
| 4 | 3 | 5 | 3 |
| 5 | 3 | 3 | 3 |
| 6 | 4 | 4 | 4 |
| 7 | 4 | 5 | 3 |
| 8 | 2 | 2 | 1 |
| 9 | 4 | 4 | 4 |
| 10 | 4 | 5 | 4 |
| 11 | 5 | 4 | 4 |
| 12 | 3 | 4 | 3 |
| 13 | 3 | 3 | 3 |
| 14 | 3 | too small to assess | 3 |
| 15 | 4 | 5 | 3 |
| 16 | 3 | too small to assess | 3 |
| 17 | 4 | 5 | 3 |
| 18 | 4 | 4 | 4 |
| 19 | 1 | too small to assess | 1 |
| 20 | 4 | 3 | 3 |
| 21 | 4 | 4 | 3 |
| 22 | 2 | 1 | 1 |
| 23 | 4 | 4 | 4 |
| 24 | 2 | 1 | 2 |
| 25 | 3 | 5 | 4 |
| 26 | 3 | 3 | 4 |
| 27 | 2 | too small to assess | 3 |
| 28 | 2 | 2 | 2 |
| 29 | 3 | 2 | 2 |
| 30 | 4 | 4 | 3 |
| 31 | 3 | 3 | 3 |
| 32 | 4 | too small to assess | 4 |
| 33 | 3 | 3 | 3 |
| 34 | 1 | 1 | 1 |
| 35 | 3 | 2 | 3 |
| 36 | 3 | 3 | 3 |
| 37 | 4 | 4 | 4 |
| 38 | 4 | 4 | 4 |
| 39 | 4 | 1 | 5 |
| 40 | 3 | 3 | 3 |
| 41 | 4 | 4 | 3 |
| 42 | 4 | 4 | 4 |
| 43 | 4 | 4 | 3 |
| 44 | 4 | 4 | 4 |
| 45 | 4 | 4 | 3 |
| 46 | 4 | 4 | 4 |
| 47 | 2 | 2 | 2 |

| | | | |
|---|---|---|---|
| 48 | 3 | 4 | 4 |
| 49 | 4 | 5 | 4 |
| 50 | 2 | 2 | 2 |
| 51 | 3 | 3 | 2 |
| 52 | 4 | 4 | 4 |

## References


1. Glish, G.L. & Vachet, R.W. The basics of mass spectrometry in the twenty-first century. *Nat Rev Drug Discov* **2**, 140-150 (2003).
2. Ho, C.S.*, et al.* Electrospray ionisation mass spectrometry: principles and clinical applications. *Clin Biochem Rev* **24**, 3-12 (2003).
3. Tanaka, K.*, et al.* Protein and polymer analyses up to m/z 100 000 by laser ionization time-of-flight mass spectrometry. *Rapid Communications in Mass Spectrometry* **2**, 151-153 (1988).
4. Karas, M. & Hillenkamp, F. Laser desorption ionization of proteins with molecular masses exceeding 10,000 daltons. *Anal Chem* **60**, 2299-2301 (1988).
5. Dave, K.A., Headlam, M.J., Wallis, T.P. & Gorman, J.J. Preparation and analysis of proteins and peptides using MALDI TOF/TOF mass spectrometry. *Curr Protoc Protein Sci* **Chapter 16**, Unit 16 13 (2011).
6. Marto, J.A., White, F.M., Seldomridge, S. & Marshall, A.G. Structural characterization of phospholipids by matrix-assisted laser desorption/ionization Fourier transform ion cyclotron resonance mass spectrometry. *Anal Chem* **67**, 3979-3984 (1995).
7. Alterman, M.A., Gogichayeva, N.V. & Kornilayev, B.A. Matrix-assisted laser desorption/ionization time-of-flight mass spectrometry-based amino acid analysis. *Anal Biochem* **335**, 184-191 (2004).
8. Singhal, N., Kumar, M., Kanaujia, P.K. & Virdi, J.S. MALDI-TOF mass spectrometry: an emerging technology for microbial identification and diagnosis. *Front Microbiol* **6**, 791 (2015).
9. Bizzini, A. & Greub, G. Matrix-assisted laser desorption ionization time-of-flight mass spectrometry, a revolution in clinical microbial identification. *Clin Microbiol Infect* **16**, 1614-1619 (2010).
10. Laiko, V.V., Baldwin, M.A. & Burlingame, A.L. Atmospheric pressure matrix-assisted laser desorption/ionization mass spectrometry. *Anal Chem* **72**, 652-657 (2000).
11. Lu, I.C., Lee, C., Lee, Y.T. & Ni, C.K. Ionization Mechanism of Matrix-Assisted Laser Desorption/Ionization. *Annu Rev Anal Chem (Palo Alto Calif)* **8**, 21-39 (2015).
12. Knochenmuss, R. Ion formation mechanisms in UV-MALDI. *Analyst* **131**, 966-986 (2006).
13. Guenther, S., Koestler, M., Schulz, O. & Spengler, B. Laser spot size and laser power dependence of ion formation in high resolution MALDI imaging. *International Journal of Mass Spectrometry* **294**, 7-15 (2010).
14. Chen, X., Carroll, J.A. & Beavis, R.C. Near-ultraviolet-induced matrix-assisted laser desorption/ionization as a function of wavelength. *Journal of the American Society for Mass Spectrometry* **9**, 885-891 (1998).
15. Mamyrin, B.A. Time-of-flight mass spectrometry (concepts, achievements, and prospects). *International Journal of Mass Spectrometry* **206**, 251-266 (2001).
16. Brown, R.S. & Lennon, J.J. Mass resolution improvement by incorporation of pulsed ion extraction in a matrix-assisted laser desorption/ionization linear time-of-flight mass spectrometer. *Anal Chem* **67**, 1998-2003 (1995).
17. Vestal, M.L., Juhasz, P. & Martin, S.A. Delayed extraction matrix-assisted laser desorption time-of-flight mass spectrometry. *Rapid Communications in Mass Spectrometry* **9**, 1044-1050 (1995).
18. Perkins, D.N., Pappin, D.J., Creasy, D.M. & Cottrell, J.S. Probability-based protein identification by searching sequence databases using mass spectrometry data. *Electrophoresis* **20**, 3551-3567 (1999).

19. *NIST Chemistry WebBook, NIST Standard Reference Database Number 69*, (National Institute of Standards and Technology, 2005).
20. Spengler, B. Post-source decay analysis in matrix-assisted laser desorption/ionization mass spectrometry of biomolecules. *Journal of Mass Spectrometry* **32**, 1019-1036 (1997).
21. Marshall, A.G. & Hendrickson, C.L. Fourier transform ion cyclotron resonance detection: principles and experimental configurations. *International Journal of Mass Spectrometry* **215**, 59-75 (2002).
22. McKenna, A.M.*, et al.* Unprecedented Ultrahigh Resolution FT-ICR Mass Spectrometry and Parts-Per-Billion Mass Accuracy Enable Direct Characterization of Nickel and Vanadyl Porphyrins in Petroleum from Natural Seeps. *Energy & Fuels* **28**, 2454-2464 (2014).
23. Marshall, A.G., Hendrickson, C.L. & Jackson, G.S. Fourier transform ion cyclotron resonance mass spectrometry: a primer. *Mass Spectrom Rev* **17**, 1-35 (1998).
24. Stoll, N., Schmidt, E. & Thurow, K. Isotope Pattern Evaluation for the Reduction of Elemental Compositions Assigned to High-Resolution Mass Spectral Data from Electrospray Ionization Fourier Transform Ion Cyclotron Resonance Mass Spectrometry. *Journal of the American Society for Mass Spectrometry* **17**, 1692-1699 (2006).
25. Dodds, E.D., German, J.B. & Lebrilla, C.B. Enabling MALDI-FTICR-MS/MS for high-performance proteomics through combination of infrared and collisional activation. *Anal Chem* **79**, 9547-9556 (2007).
26. Thomas, A., Patterson, N.H., Dufresne, M. & Chaurand, P. (MA)LDI MS Imaging at High Specificity and Sensitivity. in *Advances in MALDI and Laser-Induced Soft Ionization Mass Spectrometry* (ed. Cramer, R.) 129-147 (Springer International Publishing, Cham, 2016).
27. Takats, Z., Wiseman, J.M. & Cooks, R.G. Ambient mass spectrometry using desorption electrospray ionization (DESI): instrumentation, mechanisms and applications in forensics, chemistry, and biology. *J Mass Spectrom* **40**, 1261-1275 (2005).
28. Chaurand, P., Schwartz, S.A., Reyzer, M.L. & Caprioli, R.M. Imaging mass spectrometry: principles and potentials. *Toxicologic pathology* **33**, 92-101 (2005).
29. Chaurand, P. Imaging mass spectrometry of thin tissue sections: a decade of collective efforts. *Journal of proteomics* **75**, 4883-4892 (2012).
30. Fujimura, Y. & Miura, D. MALDI Mass Spectrometry Imaging for Visualizing In Situ Metabolism of Endogenous Metabolites and Dietary Phytochemicals. *Metabolites* **4**, 319-346 (2014).
31. Senoner, M. & Unger, W.E.S. SIMS imaging of the nanoworld: applications in science and technology. *Journal of Analytical Atomic Spectrometry* **27**, 1050-1068 (2012).
32. Laskin, J., Heath, B.S., Roach, P.J., Cazares, L. & Semmes, O.J. Tissue Imaging Using Nanospray Desorption Electrospray Ionization Mass Spectrometry. *Analytical Chemistry* **84**, 141-148 (2012).
33. Nemes, P. & Vertes, A. Laser ablation electrospray ionization for atmospheric pressure, in vivo, and imaging mass spectrometry. *Anal Chem* **79**, 8098-8106 (2007).
34. Zhang, Y., Hong, H. & Cai, W. Imaging with Raman spectroscopy. *Curr Pharm Biotechnol* **11**, 654-661 (2010).
35. de Matos, L.L., Trufelli, D.C., de Matos, M.G.L. & da Silva Pinhal, M.A. Immunohistochemistry as an Important Tool in Biomarkers Detection and Clinical Practice. *Biomarker Insights* **5**, 9-20 (2010).
36. Maier, S.K.*, et al.* Comprehensive identification of proteins from MALDI imaging. *Mol Cell Proteomics* **12**, 2901-2910 (2013).

37. Nicklay, J.J., Harris, G.A., Schey, K.L. & Caprioli, R.M. MALDI Imaging and in Situ Identification of Integral Membrane Proteins from Rat Brain Tissue Sections. *Analytical Chemistry* **85**, 7191-7196 (2013).
38. Stauber, J.*, et al.* On-tissue protein identification and imaging by MALDI-ion mobility mass spectrometry. *J Am Soc Mass Spectrom* **21**, 338-347 (2010).
39. Trim, P.J. & Snel, M.F. Small molecule MALDI MS imaging: Current technologies and future challenges. *Methods* (2016).
40. Rizk, A.*, et al.* Segmentation and quantification of subcellular structures in fluorescence microscopy images using Squassh. *Nat Protoc* **9**, 586-596 (2014).
41. Chaurand, P., Schriver, K.E. & Caprioli, R.M. Instrument design and characterization for high resolution MALDI-MS imaging of tissue sections. *Journal of mass spectrometry : JMS* **42**, 476-489 (2007).
42. Castellino, S., Groseclose, M.R. & Wagner, D. MALDI imaging mass spectrometry: bridging biology and chemistry in drug development. *Bioanalysis* **3**, 2427-2441 (2011).
43. Burrell, M., Earnshaw, C. & Clench, M. Imaging Matrix Assisted Laser Desorption Ionization Mass Spectrometry: a technique to map plant metabolites within tissues at high spatial resolution. *J Exp Bot* **58**, 757-763 (2007).
44. Vrkoslav, V., Muck, A., Cvacka, J. & Svatos, A. MALDI imaging of neutral cuticular lipids in insects and plants. *J Am Soc Mass Spectrom* **21**, 220-231 (2010).
45. Franceschi, P., Dong, Y., Strupat, K., Vrhovsek, U. & Mattivi, F. Combining intensity correlation analysis and MALDI imaging to study the distribution of flavonols and dihydrochalcones in Golden Delicious apples. *J Exp Bot* **63**, 1123-1133 (2012).
46. Horn, P.J.*, et al.* Spatial Mapping of Lipids at Cellular Resolution in Embryos of Cotton. *The Plant Cell* **24**, 622-636 (2012).
47. Bjarnholt, N., Li, B., D'Alvise, J. & Janfelt, C. Mass spectrometry imaging of plant metabolites--principles and possibilities. *Natural product reports* **31**, 818-837 (2014).
48. Urban, P.L., Chang, C.H., Wu, J.T. & Chen, Y.C. Microscale MALDI imaging of outer-layer lipids in intact egg chambers from Drosophila melanogaster. *Anal Chem* **83**, 3918-3925 (2011).
49. Yew, J.Y., Soltwisch, J., Pirkl, A. & Dreisewerd, K. Direct laser desorption ionization of endogenous and exogenous compounds from insect cuticles: practical and methodologic aspects. *J Am Soc Mass Spectrom* **22**, 1273-1284 (2011).
50. Niehoff, A.C.*, et al.* Analysis of Drosophila lipids by matrix-assisted laser desorption/ionization mass spectrometric imaging. *Anal Chem* **86**, 11086-11092 (2014).
51. Pratavieira, M.*, et al.* MALDI imaging analysis of neuropeptides in the Africanized honeybee (Apis mellifera) brain: effect of ontogeny. *J Proteome Res* **13**, 3054-3064 (2014).
52. Bhandari, D.R., Schott, M., Rompp, A., Vilcinskas, A. & Spengler, B. Metabolite localization by atmospheric pressure high-resolution scanning microprobe matrix-assisted laser desorption/ionization mass spectrometry imaging in whole-body sections and individual organs of the rove beetle Paederus riparius. *Analytical and bioanalytical chemistry* **407**, 2189-2201 (2015).
53. Khalil, S.M., Rompp, A., Pretzel, J., Becker, K. & Spengler, B. Phospholipid Topography of Whole-Body Sections of the Anopheles stephensi Mosquito, Characterized by High-Resolution Atmospheric-Pressure Scanning Microprobe Matrix-Assisted Laser Desorption/Ionization Mass Spectrometry Imaging. *Anal Chem* **87**, 11309-11316 (2015).
54. Groseclose, M.R., Massion, P.P., Chaurand, P. & Caprioli, R.M. High-throughput proteomic analysis of formalin-fixed paraffin-embedded tissue microarrays using MALDI imaging mass spectrometry. *Proteomics* **8**, 3715-3724 (2008).
55. Ergin, B.*, et al.* Proteomic analysis of PAXgene-fixed tissues. *J Proteome Res* **9**, 5188-5196 (2010).

56. Oetjen, J.*, et al.* MRI-compatible pipeline for three-dimensional MALDI imaging mass spectrometry using PAXgene fixation. *Journal of proteomics* **90**, 52-60 (2013).
57. Steiner, C.*, et al.* Applications of mass spectrometry for quantitative protein analysis in formalin-fixed paraffin-embedded tissues. *Proteomics* **14**, 441-451 (2014).
58. Powers, T.W.*, et al.* Matrix assisted laser desorption ionization imaging mass spectrometry workflow for spatial profiling analysis of N-linked glycan expression in tissues. *Anal Chem* **85**, 9799-9806 (2013).
59. Wisztorski, M., Franck, J., Salzet, M. & Fournier, I. MALDI direct analysis and imaging of frozen versus FFPE tissues: what strategy for which sample? *Methods Mol Biol* **656**, 303-322 (2010).
60. Baenke, F., Peck, B., Miess, H. & Schulze, A. Hooked on fat: the role of lipid synthesis in cancer metabolism and tumour development. *Dis Model Mech* **6**, 1353-1363 (2013).
61. Krauss, R.M. Lipids and lipoproteins in patients with type 2 diabetes. *Diabetes Care* **27**, 1496-1504 (2004).
62. Wenk, M.R. The emerging field of lipidomics. *Nature reviews. Drug discovery* **4**, 594-610 (2005).
63. Shevchenko, A. & Simons, K. Lipidomics: coming to grips with lipid diversity. *Nat Rev Mol Cell Biol* **11**, 593-598 (2010).
64. Dufresne, M., Thomas, A., Breault-Turcot, J., Masson, J.F. & Chaurand, P. Silver-assisted laser desorption ionization for high spatial resolution imaging mass spectrometry of olefins from thin tissue sections. *Anal Chem* **85**, 3318-3324 (2013).
65. Dufresne, M., Masson, J.F. & Chaurand, P. Gold assisted laser desorption ionization for enhanced imaging mass spectrometry of triacylglycerols from thin tissue sections. *Anal Chem* **Accepted**(2016).
66. Jackson, S.N., Wang, H.Y. & Woods, A.S. Direct profiling of lipid distribution in brain tissue using MALDI-TOFMS. *Analytical chemistry* **77**, 4523-4527 (2005).
67. Jones, E.E.*, et al.* On-tissue localization of ceramides and other sphingolipids by MALDI mass spectrometry imaging. *Analytical chemistry* **86**, 8303-8311 (2014).
68. Cobice, D.F.*, et al.* Mass spectrometry imaging for dissecting steroid intracrinology within target tissues. *Anal Chem* **85**, 11576-11584 (2013).
69. Shih, C.J., Chen, P.Y., Liaw, C.C., Lai, Y.M. & Yang, Y.L. Bringing microbial interactions to light using imaging mass spectrometry. *Natural product reports* **31**, 739-755 (2014).
70. Wills, R.H., Tosin, M. & O'Connor, P.B. Structural characterization of polyketides using high mass accuracy tandem mass spectrometry. *Anal Chem* **84**, 8863-8870 (2012).
71. Martano, C., Mugoni, V., Dal Bello, F., Santoro, M.M. & Medana, C. Rapid high performance liquid chromatography-high resolution mass spectrometry methodology for multiple prenol lipids analysis in zebrafish embryos. *J Chromatogr A* **1412**, 59-66 (2015).
72. Thomas, M.C.*, et al.* Elucidation of double bond position in unsaturated lipids by ozone electrospray ionization mass spectrometry. *Anal Chem* **79**, 5013-5022 (2007).
73. Hsu, F.F. & Turk, J. Elucidation of the double-bond position of long-chain unsaturated fatty acids by multiple-stage linear ion-trap mass spectrometry with electrospray ionization. *J Am Soc Mass Spectrom* **19**, 1673-1680 (2008).
74. Castro-Perez, J.*, et al.* Localization of fatty acyl and double bond positions in phosphatidylcholines using a dual stage CID fragmentation coupled with ion mobility mass spectrometry. *J Am Soc Mass Spectrom* **22**, 1552-1567 (2011).
75. Jones, J.W., Thompson, C.J., Carter, C.L. & Kane, M.A. Electron-induced dissociation (EID) for structure characterization of glycerophosphatidylcholine: determination of double-bond positions and localization of acyl chains. *J Mass Spectrom* **50**, 1327-1339 (2015).

76. Rivera, R. & Chun, J. Biological effects of lysophospholipids. in *Reviews of Physiology Biochemistry and Pharmacology* 25-46 (Springer Berlin Heidelberg, Berlin, Heidelberg, 2008).
77. Ariga, T., Jarvis, W.D. & Yu, R.K. Role of sphingolipid-mediated cell death in neurodegenerative diseases. *J Lipid Res* **39**, 1-16 (1998).
78. Hannun, Y.A. & Obeid, L.M. The Ceramide-centric universe of lipid-mediated cell regulation: stress encounters of the lipid kind. *J Biol Chem* **277**, 25847-25850 (2002).
79. Ogretmen, B. & Hannun, Y.A. Biologically active sphingolipids in cancer pathogenesis and treatment. *Nat Rev Cancer* **4**, 604-616 (2004).
80. Zheng, W.*, et al.* Ceramides and other bioactive sphingolipid backbones in health and disease: lipidomic analysis, metabolism and roles in membrane structure, dynamics, signaling and autophagy. *Biochim Biophys Acta* **1758**, 1864-1884 (2006).
81. Pralhada Rao, R.*, et al.* Sphingolipid metabolic pathway: an overview of major roles played in human diseases. *J Lipids* **2013**, 178910 (2013).
82. Ahmadian, M., Duncan, R.E., Jaworski, K., Sarkadi-Nagy, E. & Sul, H.S. Triacylglycerol metabolism in adipose tissue. *Future Lipidol* **2**, 229-237 (2007).
83. Brasaemle, D.L. & Wolins, N.E. Packaging of fat: an evolving model of lipid droplet assembly and expansion. *J Biol Chem* **287**, 2273-2279 (2012).
84. Harkewicz, R. & Dennis, E.A. Applications of mass spectrometry to lipids and membranes. *Annu Rev Biochem* **80**, 301-325 (2011).
85. Hankin, J.A., Barkley, R.M. & Murphy, R.C. Sublimation as a method of matrix application for mass spectrometric imaging. *Journal of the American Society for Mass Spectrometry* **18**, 1646-1652 (2007).
86. Yang, J. & Caprioli, R.M. Matrix sublimation/recrystallization for imaging proteins by mass spectrometry at high spatial resolution. *Anal Chem* **83**, 5728-5734 (2011).
87. Angel, P.M., Spraggins, J.M., Baldwin, H.S. & Caprioli, R. Enhanced sensitivity for high spatial resolution lipid analysis by negative ion mode matrix assisted laser desorption ionization imaging mass spectrometry. *Analytical chemistry* **84**, 1557-1564 (2012).
88. Zavalin, A.*, et al.* Direct imaging of single cells and tissue at sub-cellular spatial resolution using transmission geometry MALDI MS. *J Mass Spectrom* **47**, 1473-1481 (2012).
89. Thomas, A., Charbonneau, J.L., Fournaise, E. & Chaurand, P. Sublimation of new matrix candidates for high spatial resolution imaging mass spectrometry of lipids: enhanced information in both positive and negative polarities after 1,5-diaminonapthalene deposition. *Analytical chemistry* **84**, 2048-2054 (2012).
90. Thomas, A.*, et al.* Histology-driven data mining of lipid signatures from multiple imaging mass spectrometry analyses: application to human colorectal cancer liver metastasis biopsies. *Analytical chemistry* **85**, 2860-2866 (2013).
91. Hsu, F.F. & Turk, J. Electrospray ionization/tandem quadrupole mass spectrometric studies on phosphatidylcholines: the fragmentation processes. *Journal of the American Society for Mass Spectrometry* **14**, 352-363 (2003).
92. Paglia, G., Kliman, M., Claude, E., Geromanos, S. & Astarita, G. Applications of ion-mobility mass spectrometry for lipid analysis. *Analytical and bioanalytical chemistry* **407**, 4995-5007 (2015).
93. Schone, C., Hofler, H. & Walch, A. MALDI imaging mass spectrometry in cancer research: combining proteomic profiling and histological evaluation. *Clinical biochemistry* **46**, 539-545 (2013).
94. Merlos Rodrigo, M.A.*, et al.* MALDI-TOF MS as evolving cancer diagnostic tool: A review. *Journal of Pharmaceutical and Biomedical Analysis* **95**, 245-255 (2014).
95. Djidja, M.C.*, et al.* Novel molecular tumour classification using MALDI-mass spectrometry imaging of tissue micro-array. *Anal Bioanal Chem* **397**, 587-601 (2010).

96. Rauser, S.*, et al.* Classification of HER2 receptor status in breast cancer tissues by MALDI imaging mass spectrometry. *J Proteome Res* **9**, 1854-1863 (2010).
97. Meding, S.*, et al.* Tumor classification of six common cancer types based on proteomic profiling by MALDI imaging. *J Proteome Res* **11**, 1996-2003 (2012).
98. Casadonte, R.*, et al.* Imaging mass spectrometry to discriminate breast from pancreatic cancer metastasis in formalin-fixed paraffin-embedded tissues. *Proteomics* **14**, 956-964 (2014).
99. Kriegsmann, J., Kriegsmann, M. & Casadonte, R. MALDI TOF imaging mass spectrometry in clinical pathology: a valuable tool for cancer diagnostics (review). *International journal of oncology* **46**, 893-906 (2015).
100. Schwamborn, K. & Caprioli, R.M. Molecular imaging by mass spectrometry--looking beyond classical histology. *Nature reviews. Cancer* **10**, 639-646 (2010).
101. Aichler, M. & Walch, A. MALDI Imaging mass spectrometry: current frontiers and perspectives in pathology research and practice. *Laboratory investigation; a journal of technical methods and pathology* **95**, 422-431 (2015).
102. Hanrieder, J., Ljungdahl, A. & Andersson, M. MALDI imaging mass spectrometry of neuropeptides in Parkinson's disease. *J Vis Exp* (2012).
103. Lalowski, M.*, et al.* Imaging mass spectrometry: a new tool for kidney disease investigations. *Nephrol Dial Transplant* **28**, 1648-1656 (2013).
104. Anderson, D.M.*, et al.* High resolution MALDI imaging mass spectrometry of retinal tissue lipids. *Journal of the American Society for Mass Spectrometry* **25**, 1394-1403 (2014).
105. Hong, J.H.*, et al.* Global changes of phospholipids identified by MALDI imaging mass spectrometry in a mouse model of Alzheimer's disease. *J Lipid Res* **57**, 36-45 (2016).
106. Liu, L.*, et al.* Global, regional, and national causes of child mortality: an updated systematic analysis for 2010 with time trends since 2000. *Lancet* **379**, 2151-2161 (2012).
107. Tabas, I., Williams, K.J. & Boren, J. Subendothelial lipoprotein retention as the initiating process in atherosclerosis: update and therapeutic implications. *Circulation* **116**, 1832-1844 (2007).
108. Tabas, I. Macrophage death and defective inflammation resolution in atherosclerosis. *Nat Rev Immunol* **10**, 36-46 (2010).
109. Libby, P., Ridker, P.M. & Hansson, G.K. Progress and challenges in translating the biology of atherosclerosis. *Nature* **473**, 317-325 (2011).
110. Finn, A.V., Nakano, M., Narula, J., Kolodgie, F.D. & Virmani, R. Concept of vulnerable/unstable plaque. *Arterioscler Thromb Vasc Biol* **30**, 1282-1292 (2010).
111. Joseph, A., Ackerman, D., Talley, J.D., Johnstone, J. & Kupersmith, J. Manifestations of coronary atherosclerosis in young trauma victims--an autopsy study. *J Am Coll Cardiol* **22**, 459-467 (1993).
112. Thomas, A.*, et al.* Mass spectrometry for the evaluation of cardiovascular diseases based on proteomics and lipidomics. *Thrombosis and haemostasis* **106**, 20-33 (2011).
113. Stewart, B.W., Wild, C., International Agency for Research on Cancer & World Health Organization. *World cancer report 2014*.
114. Baize, N.*, et al.* Long-term survival of patients downstaged by oxaliplatin and 5-fluorouracil combination followed by rescue surgery for unresectable colorectal liver metastases. *Gastroenterol Clin Biol* **30**, 1349-1353 (2006).
115. Lam, V.W.*, et al.* A systematic review of clinical response and survival outcomes of downsizing systemic chemotherapy and rescue liver surgery in patients with initially unresectable colorectal liver metastases. *Ann Surg Oncol* **19**, 1292-1301 (2012).
116. Paschos, K.A., Majeed, A.W. & Bird, N.C. Natural history of hepatic metastases from colorectal cancer--pathobiological pathways with clinical significance. *World J Gastroenterol* **20**, 3719-3737 (2014).

117. Rejniak, K.A. Investigating dynamical deformations of tumor cells in circulation: predictions from a theoretical model. *Front Oncol* **2**, 111 (2012).
118. Gout, S. & Huot, J. Role of cancer microenvironment in metastasis: focus on colon cancer. *Cancer Microenviron* **1**, 69-83 (2008).
119. Yan, G., Li, L., Zhu, B. & Li, Y. Lipidome in colorectal cancer. *Oncotarget* (2016).
120. Ogrinc Potočnik, N., Porta, T., Becker, M., Heeren, R.M.A. & Ellis, S.R. Use of advantageous, volatile matrices enabled by next-generation high-speed matrix-assisted laser desorption/ionization time-of-flight imaging employing a scanning laser beam. *Rapid Communications in Mass Spectrometry* **29**, 2195-2203 (2015).
121. Schramm, T.*, et al.* imzML--a common data format for the flexible exchange and processing of mass spectrometry imaging data. *Journal of proteomics* **75**, 5106-5110 (2012).
122. Rompp, A.*, et al.* imzML: Imaging Mass Spectrometry Markup Language: A common data format for mass spectrometry imaging. *Methods in molecular biology* **696**, 205-224 (2011).
123. Rompp, A.*, et al.* A public repository for mass spectrometry imaging data. *Analytical and bioanalytical chemistry* **407**, 2027-2033 (2015).
124. McDonnell, L.A.*, et al.* Discussion point: reporting guidelines for mass spectrometry imaging. *Analytical and bioanalytical chemistry* **407**, 2035-2045 (2015).
125. Race, A.M. & Bunch, J. Optimisation of colour schemes to accurately display mass spectrometry imaging data based on human colour perception. *Analytical and bioanalytical chemistry* **407**, 2047-2054 (2015).
126. Palmer, A.*, et al.* Using collective expert judgements to evaluate quality measures of mass spectrometry images. *Bioinformatics* **31**, i375-i384 (2015).
127. Dilbeck, C.W. & Finlayson-Pitts, B.J. Hydroxyl radical oxidation of phospholipid-coated NaCl particles. *Phys Chem Chem Phys* **15**, 9833-9844 (2013).
128. Niki, E., Yoshida, Y., Saito, Y. & Noguchi, N. Lipid peroxidation: mechanisms, inhibition, and biological effects. *Biochem Biophys Res Commun* **338**, 668-676 (2005).
129. Watrous, J.D.*, et al.* Microbial metabolic exchange in 3D. *ISME J* **7**, 770-780 (2013).
130. Fornai, L.*, et al.* Three-dimensional molecular reconstruction of rat heart with mass spectrometry imaging. *Analytical and bioanalytical chemistry* **404**, 2927-2938 (2012).
131. Attia, A.S.*, et al.* Monitoring the inflammatory response to infection through the integration of MALDI IMS and MRI. *Cell Host Microbe* **11**, 664-673 (2012).
132. Jones, E.A.*, et al.* Imaging mass spectrometry to visualize biomolecule distributions in mouse brain tissue following hemispheric cortical spreading depression. *J Proteomics* **75**, 5027-5035 (2012).
133. Oetjen, J.*, et al.* Benchmark datasets for 3D MALDI- and DESI-imaging mass spectrometry. *Gigascience* **4**, 20 (2015).
134. Gibb, S. & Strimmer, K. MALDIquant: a versatile R package for the analysis of mass spectrometry data. *Bioinformatics* **28**, 2270-2271 (2012).
135. Robichaud, G., Garrard, K.P., Barry, J.A. & Muddiman, D.C. MSiReader: an open-source interface to view and analyze high resolving power MS imaging files on Matlab platform. *J Am Soc Mass Spectrom* **24**, 718-721 (2013).
136. Bemis, K.D.*, et al.* Cardinal: an R package for statistical analysis of mass spectrometry-based imaging experiments. *Bioinformatics* **31**, 2418-2420 (2015).
137. Crecelius, A.C.*, et al.* Three-dimensional visualization of protein expression in mouse brain structures using imaging mass spectrometry. *Journal of the American Society for Mass Spectrometry* **16**, 1093-1099 (2005).
138. Parry, P.V. & Engh, J.A. Ambient mass spectrometry for the intraoperative molecular diagnosis of human brain tumors. *Neurosurgery* **72**, N17-18 (2013).

139. Thiele, H.*, et al.* 2D and 3D MALDI-imaging: conceptual strategies for visualization and data mining. *Biochim Biophys Acta* **1844**, 117-137 (2014).
140. Jones, E.A.*, et al.* Multiple statistical analysis techniques corroborate intratumor heterogeneity in imaging mass spectrometry datasets of myxofibrosarcoma. *PLoS One* **6**, e24913 (2011).
141. Alexandrov, T.*, et al.* Spatial segmentation of imaging mass spectrometry data with edge-preserving image denoising and clustering. *J Proteome Res* **9**, 6535-6546 (2010).
142. Krasny, L.*, et al.* Spatial segmentation of MALDI FT-ICR MSI data: a powerful tool to explore the head and neck tumor in situ lipidome. *J Am Soc Mass Spectrom* **26**, 36-43 (2015).
143. Jones, E.A., Deininger, S.O., Hogendoorn, P.C., Deelder, A.M. & McDonnell, L.A. Imaging mass spectrometry statistical analysis. *Journal of proteomics* **75**, 4962-4989 (2012).
144. Alexandrov, T. & Kobarg, J.H. Efficient spatial segmentation of large imaging mass spectrometry datasets with spatially aware clustering. *Bioinformatics* **27**, i230-238 (2011).
145. Van de Plas, R., Yang, J., Spraggins, J. & Caprioli, R.M. Image fusion of mass spectrometry and microscopy: a multimodality paradigm for molecular tissue mapping. *Nature methods* **12**, 366-372 (2015).
146. Mirnezami, R.*, et al.* Chemical mapping of the colorectal cancer microenvironment via MALDI imaging mass spectrometry (MALDI-MSI) reveals novel cancer-associated field effects. *Mol Oncol* **8**, 39-49 (2014).
147. Cornett, D.S., Reyzer, M.L., Chaurand, P. & Caprioli, R.M. MALDI imaging mass spectrometry: molecular snapshots of biochemical systems. *Nature methods* **4**, 828-833 (2007).
148. Chaurand, P., Norris, J.L., Cornett, D.S., Mobley, J.A. & Caprioli, R.M. New developments in profiling and imaging of proteins from tissue sections by MALDI mass spectrometry. *Journal of proteome research* **5**, 2889-2900 (2006).
149. Groseclose, M.R., Andersson, M., Hardesty, W.M. & Caprioli, R.M. Identification of proteins directly from tissue: in situ tryptic digestions coupled with imaging mass spectrometry. *Journal of mass spectrometry : JMS* **42**, 254-262 (2007).
150. Stoeckli, M., Staab, D. & Schweitzer, A. Compound and metabolite distribution measured by MALDI mass spectrometric imaging in whole-body tissue sections. *International Journal of Mass Spectrometry* **260**, 195-202 (2007).
151. Murphy, R.C., Hankin, J.A. & Barkley, R.M. Imaging of lipid species by MALDI mass spectrometry. *Journal of lipid research* **50 Suppl**, S317-322 (2009).
152. Sparvero, L.J.*, et al.* Mapping of phospholipids by MALDI imaging (MALDI-MSI): realities and expectations. *Chem Phys Lipids* **165**, 545-562 (2012).
153. Berry, K.A.*, et al.* MALDI imaging of lipid biochemistry in tissues by mass spectrometry. *Chemical reviews* **111**, 6491-6512 (2011).
154. Yang, J., Chaurand, P., Norris, J.L., Porter, N.A. & Caprioli, R.M. Activity-based probes linked with laser-cleavable mass tags for signal amplification in imaging mass spectrometry: analysis of serine hydrolase enzymes in mammalian tissue. *Analytical chemistry* **84**, 3689-3695 (2012).
155. Trim, P.J.*, et al.* Instrumentation and software for mass spectrometry imaging--making the most of what you've got. *J Proteomics* **75**, 4931-4940 (2012).
156. Hankin, J.A.*, et al.* MALDI mass spectrometric imaging of lipids in rat brain injury models. *J Am Soc Mass Spectrom* **22**, 1014-1021 (2011).
157. Whitehead, S.N.*, et al.* Imaging mass spectrometry detection of gangliosides species in the mouse brain following transient focal cerebral ischemia and long-term recovery. *PLoS One* **6**, e20808 (2011).

158. Menger, R.F.*, et al.* MALDI mass spectrometric imaging of cardiac tissue following myocardial infarction in a rat coronary artery ligation model. *Anal Chem* **84**, 1117-1125 (2012).
159. Ruh, H.*, et al.* MALDI imaging MS reveals candidate lipid markers of polycystic kidney disease. *J Lipid Res* **54**, 2785-2794 (2013).
160. Hart, P.J., Francese, S., Claude, E., Woodroofe, M.N. & Clench, M.R. MALDI-MS imaging of lipids in ex vivo human skin. *Anal Bioanal Chem* **401**, 115-125 (2011).
161. Deininger, S.O.*, et al.* Normalization in MALDI-TOF imaging datasets of proteins: practical considerations. *Anal Bioanal Chem* **401**, 167-181 (2011).
162. Fonville, J.M.*, et al.* Robust data processing and normalization strategy for MALDI mass spectrometric imaging. *Anal Chem* **84**, 1310-1319 (2012).
163. Seeley, E.H., Oppenheimer, S.R., Mi, D., Chaurand, P. & Caprioli, R.M. Enhancement of protein sensitivity for MALDI imaging mass spectrometry after chemical treatment of tissue sections. *Journal of the American Society for Mass Spectrometry* **19**, 1069-1077 (2008).
164. Goodwin, R.J., Dungworth, J.C., Cobb, S.R. & Pitt, A.R. Time-dependent evolution of tissue markers by MALDI-MS imaging. *Proteomics* **8**, 3801-3808 (2008).
165. Ferguson, L., Bradshaw, R., Wolstenholme, R., Clench, M. & Francese, S. Two-step matrix application for the enhancement and imaging of latent fingermarks. *Anal Chem* **83**, 5585-5591 (2011).
166. Goodwin, R.J. Sample preparation for mass spectrometry imaging: small mistakes can lead to big consequences. *Journal of proteomics* **75**, 4893-4911 (2012).
167. Chaurand, P.*, et al.* Integrating histology and imaging mass spectrometry. *Analytical chemistry* **76**, 1145-1155 (2004).
168. Harrison, K.A.*, et al.* Analysis of oxidized glycerophosphocholine lipids using electrospray ionization mass spectrometry and microderivatization techniques. *Journal of Mass Spectrometry* **35**, 224-236 (2000).
169. Domingues, M.R., Reis, A. & Domingues, P. Mass spectrometry analysis of oxidized phospholipids. *Chem Phys Lipids* **156**, 1-12 (2008).
170. Stübiger, G.*, et al.* Analysis of Oxidized Phospholipids by MALDI Mass Spectrometry Using 6-Aza-2-thiothymine Together with Matrix Additives and Disposable Target Surfaces. *Anal Chem* **82**, 5502-5510 (2010).
171. Stutts, W.L., Menger, R.F., Kiss, A., Heeren, R.M. & Yost, R.A. Characterization of Phosphatidylcholine Oxidation Products by MALDI MS(n.). *Anal Chem* **85**, 11410-11419 (2013).
172. Sparvero, L.J.*, et al.* Mass-spectrometry based oxidative lipidomics and lipid imaging: applications in traumatic brain injury. *Journal of Neurochemistry* **115**, 1322-1336 (2010).
173. Rivera, R. & Chun, J. Biological effects of lysophospholipids. *Reviews of physiology, biochemistry and pharmacology* **160**, 25-46 (2008).
174. Heiskanen, L.A., Suoniemi, M., Ta, H.X., Tarasov, K. & Ekroos, K. Long-term performance and stability of molecular shotgun lipidomic analysis of human plasma samples. *Anal Chem* **85**, 8757-8763 (2013).
175. Wang, X.*, et al.* Hydroxyflavones as a New Family of Matrices for MALDI Tissue Imaging. *Anal Chem* **85**, 7566-7573 (2013).
176. Goodwin, R.J.A.*, et al.* Conductive carbon tape used for support and mounting of both whole animal and fragile heat-treated tissue sections for MALDI MS imaging and quantitation. *J Proteomics* **75**, 4912-4920 (2012).
177. Dyer, J.M.*, et al.* Spatial and temporal mass spectrometric profiling and imaging of lipid degradation in bovine M. longissimus dorsi lumborum. *Journal of Food Composition and Analysis* **33**, 203-209 (2014).

178. Stoeckli, M., Chaurand, P., Hallahan, D.E. & Caprioli, R.M. Imaging mass spectrometry: a new technology for the analysis of protein expression in mammalian tissues. *Nature medicine* **7**, 493-496 (2001).
179. Norris, J.L. & Caprioli, R.M. Analysis of tissue specimens by matrix-assisted laser desorption/ionization imaging mass spectrometry in biological and clinical research. *Chemical reviews* **113**, 2309-2342 (2013).
180. Seeley, E.H. & Caprioli, R.M. 3D Imaging by Mass Spectrometry: A New Frontier. *Analytical chemistry* **84**, 2105-2110 (2012).
181. Andersson, M., Groseclose, M.R., Deutch, A.Y. & Caprioli, R.M. Imaging mass spectrometry of proteins and peptides: 3D volume reconstruction. *Nature methods* **5**, 101-108 (2008).
182. Palmer, A.D. & Alexandrov, T. Serial 3D Imaging Mass Spectrometry at Its Tipping Point. *Analytical chemistry* **87**, 4055-4062 (2015).
183. Xiong, X.*, et al.* Data processing for 3D mass spectrometry imaging. *Journal of the American Society for Mass Spectrometry* **23**, 1147-1156 (2012).
184. Trede, D.*, et al.* Exploring three-dimensional matrix-assisted laser desorption/ionization imaging mass spectrometry data: three-dimensional spatial segmentation of mouse kidney. *Anal Chem* **84**, 6079-6087 (2012).
185. Streicher, J., Weninger, W.J. & Muller, G.B. External marker-based automatic congruencing: a new method of 3D reconstruction from serial sections. *The Anatomical record* **248**, 583-602 (1997).
186. Attia, A.S.*, et al.* Monitoring the Inflammatory Response to Infection through the Integration of MALDI IMS and MRI. *Cell Host Microbe* **11**, 664-673 (2012).
187. Spraggins, J.M. & Caprioli, R.M. High-speed MALDI-TOF imaging mass spectrometry: rapid ion image acquisition and considerations for next generation instrumentation. *Journal of the American Society for Mass Spectrometry* **22**, 1022-1031 (2011).
188. Watrous, J.D. & Dorrestein, P.C. Imaging mass spectrometry in microbiology. *Nature reviews. Microbiology* **9**, 683-694 (2011).
189. Ahlf Wheatcraft, D.R., Liu, X. & Hummon, A.B. Sample preparation strategies for mass spectrometry imaging of 3D cell culture models. *J Vis Exp* (2014).
190. Mortality, G.B.D. & Causes of Death, C. Global, regional, and national age-sex specific all-cause and cause-specific mortality for 240 causes of death, 1990-2013: a systematic analysis for the Global Burden of Disease Study 2013. *Lancet* **385**, 117-171 (2015).
191. Roth, G.A.*, et al.* Estimates of Global and Regional Premature Cardiovascular Mortality in 2025. *Circulation* **132**, 1270-1282 (2015).
192. VanderLaan, P.A., Reardon, C.A. & Getz, G.S. Site specificity of atherosclerosis: site-selective responses to atherosclerotic modulators. *Arteriosclerosis, thrombosis, and vascular biology* **24**, 12-22 (2004).
193. Shah, P.K. Inflammation and plaque vulnerability. *Cardiovascular drugs and therapy / sponsored by the International Society of Cardiovascular Pharmacotherapy* **23**, 31-40 (2009).
194. Malmberg, P.*, et al.* Localization of lipids in the aortic wall with imaging TOF-SIMS. *Biochimica et biophysica acta* **1771**, 185-195 (2007).
195. Mas, S.*, et al.* Lipid cartography of atherosclerotic plaque by cluster-TOF-SIMS imaging. *The Analyst* **132**, 24-26 (2007).
196. Lee, E.S., Shon, H.K., Lee, T.G., Kim, S.H. & Moon, D.W. The regional ratio of cholesteryl palmitate to cholesteryl oleate measured by ToF-SIMS as a key parameter of atherosclerosis. *Atherosclerosis* **226**, 378-384 (2013).
197. Lehti, S.*, et al.* Spatial Distributions of Lipids in Atherosclerosis of Human Coronary Arteries Studied by Time-of-Flight Secondary Ion Mass Spectrometry. *American Journal of Pathology* **185**, 1216-1233 (2015).

198. Zaima, N.*, et al.* Imaging mass spectrometry-based histopathologic examination of atherosclerotic lesions. *Atherosclerosis* **217**, 427-432 (2011).
199. Castro-Perez, J.*, et al.* In vivo isotopically labeled atherosclerotic aorta plaques in ApoE KO mice and molecular profiling by matrix-assisted laser desorption/ionization mass spectrometric imaging. *Rapid Commun Mass Sp* **28**, 2471-2479 (2014).
200. Martin-Lorenzo, M.*, et al.* Molecular anatomy of ascending aorta in atherosclerosis by MS Imaging: Specific lipid and protein patterns reflect pathology. *Journal of proteomics* **126**, 245-251 (2015).
201. Dufresne, M., Thomas, A., Breault-Turcot, J., Masson, J.-F. & Chaurand, P. Silver-Assisted Laser Desorption Ionization For High Spatial Resolution Imaging Mass Spectrometry of Olefins from Thin Tissue Sections. *Analytical chemistry* **85**, 3318-3324 (2013).
202. Bemis, K.D.*, et al.* Cardinal: an R package for statistical analysis of mass spectrometry-based imaging experiments. *Bioinformatics* (2015).
203. Fahy, E., Sud, M., Cotter, D. & Subramaniam, S. LIPID MAPS online tools for lipid research. *Nucleic acids research* **35**, W606-612 (2007).
204. Thevenaz, P., Ruttimann, U.E. & Unser, M. A pyramid approach to subpixel registration based on intensity. *IEEE transactions on image processing : a publication of the IEEE Signal Processing Society* **7**, 27-41 (1998).
205. Schindelin, J.*, et al.* Fiji: an open-source platform for biological-image analysis. *Nature methods* **9**, 676-682 (2012).
206. Pau, G., Fuchs, F., Sklyar, O., Boutros, M. & Huber, W. EBImage--an R package for image processing with applications to cellular phenotypes. *Bioinformatics* **26**, 979-981 (2010).
207. Schmitz, G. & Ruebsaamen, K. Metabolism and atherogenic disease association of lysophosphatidylcholine. *Atherosclerosis* **208**, 10-18 (2010).
208. Matsumoto, T., Kobayashi, T. & Kamata, K. Role of lysophosphatidylcholine (LPC) in atherosclerosis. *Current medicinal chemistry* **14**, 3209-3220 (2007).
209. Brott, T.G.*, et al.* 2011 ASA/ACCF/AHA/AANN/AANS/ACR/ASNR/CNS/SAIP/SCAI/SIR/SNIS/SVM/SVS guideline on the management of patients with extracranial carotid and vertebral artery disease: executive summary. A report of the American College of Cardiology Foundation/American Heart Association Task Force on Practice Guidelines, and the American Stroke Association, American Association of Neuroscience Nurses, American Association of Neurological Surgeons, American College of Radiology, American Society of Neuroradiology, Congress of Neurological Surgeons, Society of Atherosclerosis Imaging and Prevention, Society for Cardiovascular Angiography and Interventions, Society of Interventional Radiology, Society of NeuroInterventional Surgery, Society for Vascular Medicine, and Society for Vascular Surgery. *Circulation* **124**, 489-532 (2011).
210. Stary, H.C.*, et al.* A Definition of Advanced Types of Atherosclerotic Lesions and a Histological Classification of Atherosclerosis - a Report from the Committee on Vascular-Lesions of the Council on Arteriosclerosis, American-Heart-Association. *Circulation* **92**, 1355-1374 (1995).
211. Lovett, J.K., Gallagher, P.J., Hands, L.J., Walton, J. & Rothwell, P.M. Histological correlates of carotid plaque surface morphology on lumen contrast imaging. *Circulation* **110**, 2190-2197 (2004).
212. Redgrave, J.N., Lovett, J.K., Gallagher, P.J. & Rothwell, P.M. Histological assessment of 526 symptomatic carotid plaques in relation to the nature and timing of ischemic symptoms: the Oxford plaque study. *Circulation* **113**, 2320-2328 (2006).
213. Siegel, R., Desantis, C. & Jemal, A. Colorectal cancer statistics, 2014. *CA: a cancer journal for clinicians* **64**, 104-117 (2014).

214. Kemeny, N. Management of liver metastases from colorectal cancer. *Oncology* **20**, 1161-1176, 1179; discussion 1179-1180, 1185-1166 (2006).
215. Spolverato, G., Ejaz, A., Azad, N. & Pawlik, T.M. Surgery for colorectal liver metastases: The evolution of determining prognosis. *World journal of gastrointestinal oncology* **5**, 207-221 (2013).
216. Adam, R.*, et al.* Rescue surgery for unresectable colorectal liver metastases downstaged by chemotherapy: a model to predict long-term survival. *Annals of surgery* **240**, 644-657; discussion 657-648 (2004).
217. Haraldsdottir, S., Wu, C., Bloomston, M. & Goldberg, R.M. What is the optimal neo-adjuvant treatment for liver metastasis? *Therapeutic advances in medical oncology* **5**, 221-234 (2013).
218. Hamady, Z.Z.*, et al.* Hepatic resection for colorectal metastasis: impact of tumour size. *Annals of surgical oncology* **13**, 1493-1499 (2006).
219. Doci, R.*, et al.* One hundred patients with hepatic metastases from colorectal cancer treated by resection: analysis of prognostic determinants. *The British journal of surgery* **78**, 797-801 (1991).
220. Kokudo, N.*, et al.* Surgery for multiple hepatic colorectal metastases. *Journal of hepato-biliary-pancreatic surgery* **11**, 84-91 (2004).
221. Choti, M.A.*, et al.* Trends in long-term survival following liver resection for hepatic colorectal metastases. *Annals of surgery* **235**, 759-766 (2002).
222. Nathan, H.*, et al.* Conditional survival after surgical resection of colorectal liver metastasis: an international multi-institutional analysis of 949 patients. *Journal of the American College of Surgeons* **210**, 755-764, 764-756 (2010).
223. Ayez, N.*, et al.* Is the clinical risk score for patients with colorectal liver metastases still useable in the era of effective neoadjuvant chemotherapy? *Annals of surgical oncology* **18**, 2757-2763 (2011).
224. Snoeren, N.*, et al.* Exploring gene expression signatures for predicting disease free survival after resection of colorectal cancer liver metastases. *PloS one* **7**, e49442 (2012).
225. Kogita, A.*, et al.* Inter- and intra-tumor profiling of multi-regional colon cancer and metastasis. *Biochemical and biophysical research communications* **458**, 52-56 (2015).
226. Sinicrope, F.A.*, et al.* DNA mismatch repair status and colon cancer recurrence and survival in clinical trials of 5-fluorouracil-based adjuvant therapy. *Journal of the National Cancer Institute* **103**, 863-875 (2011).
227. Lièvre, A.*, et al.* KRAS Mutation Status Is Predictive of Response to Cetuximab Therapy in Colorectal Cancer. *Cancer Research* **66**, 3992-3995 (2006).
228. Aloia, T.*, et al.* Liver histology and surgical outcomes after preoperative chemotherapy with fluorouracil plus oxaliplatin in colorectal cancer liver metastases. *Journal of clinical oncology : official journal of the American Society of Clinical Oncology* **24**, 4983-4990 (2006).
229. Chun, Y.S., Laurent, A., Maru, D. & Vauthey, J.N. Management of chemotherapy-associated hepatotoxicity in colorectal liver metastases. *The Lancet. Oncology* **10**, 278-286 (2009).
230. Adam, R.*, et al.* Complete pathologic response after preoperative chemotherapy for colorectal liver metastases: myth or reality? *Journal of clinical oncology : official journal of the American Society of Clinical Oncology* **26**, 1635-1641 (2008).
231. Tanaka, K.*, et al.* Importance of complete pathologic response to prehepatectomy chemotherapy in treating colorectal cancer metastases. *Annals of surgery* **250**, 935-942 (2009).
232. Rubbia-Brandt, L.*, et al.* Importance of histological tumor response assessment in predicting the outcome in patients with colorectal liver metastases treated with neo-

adjuvant chemotherapy followed by liver surgery. *Annals of oncology : official journal of the European Society for Medical Oncology / ESMO* **18**, 299-304 (2007).
233. Blazer, D.G., 3rd*, et al.* Pathologic response to preoperative chemotherapy: a new outcome end point after resection of hepatic colorectal metastases. *Journal of clinical oncology : official journal of the American Society of Clinical Oncology* **26**, 5344-5351 (2008).
234. Chan, G.*, et al.* Pathological response grade of colorectal liver metastases treated with neoadjuvant chemotherapy. *HPB : the official journal of the International Hepato Pancreato Biliary Association* **12**, 277-284 (2010).
235. Chang, H.H., Leeper, W.R., Chan, G., Quan, D. & Driman, D.K. Infarct-like necrosis: a distinct form of necrosis seen in colorectal carcinoma liver metastases treated with perioperative chemotherapy. *The American journal of surgical pathology* **36**, 570-576 (2012).
236. Netto, G.J., Eisenberger, M., Epstein, J.I. & Investigators, T.A.X.T. Interobserver variability in histologic evaluation of radical prostatectomy between central and local pathologists: findings of TAX 3501 multinational clinical trial. *Urology* **77**, 1155-1160 (2011).
237. Lozanski, G.*, et al.* Inter-reader variability in follicular lymphoma grading: Conventional and digital reading. *Journal of pathology informatics* **4**, 30 (2013).
238. Chughtai, K. & Heeren, R.M. Mass spectrometric imaging for biomedical tissue analysis. *Chemical reviews* **110**, 3237-3277 (2010).
239. Jones, E.E.*, et al.* MALDI imaging mass spectrometry profiling of proteins and lipids in clear cell renal cell carcinoma. *Proteomics* **14**, 924-935 (2014).
240. Amstalden van Hove, E.R.*, et al.* Multimodal mass spectrometric imaging of small molecules reveals distinct spatio-molecular signatures in differentially metastatic breast tumor models. *Cancer Res* **70**, 9012-9021 (2010).
241. Cimino, J.*, et al.* Towards lipidomics of low-abundant species for exploring tumor heterogeneity guided by high-resolution mass spectrometry imaging. *International journal of molecular sciences* **14**, 24560-24580 (2013).
242. Alexandrov, T. MALDI imaging mass spectrometry: statistical data analysis and current computational challenges. *BMC bioinformatics* **13 Suppl 16**, S11 (2012).
243. Veselkov, K.A.*, et al.* Chemo-informatic strategy for imaging mass spectrometry-based hyperspectral profiling of lipid signatures in colorectal cancer. *Proceedings of the National Academy of Sciences of the United States of America* **111**, 1216-1221 (2014).
244. Guo, S.*, et al.* Tissue imaging and serum lipidomic profiling for screening potential biomarkers of thyroid tumors by matrix-assisted laser desorption/ionization-Fourier transform ion cyclotron resonance mass spectrometry. *Anal Bioanal Chem* **406**, 4357-4370 (2014).
245. Arana, L., Gangoiti, P., Ouro, A., Trueba, M. & Gomez-Munoz, A. Ceramide and ceramide 1-phosphate in health and disease. *Lipids in health and disease* **9**, 15 (2010).
246. Gomez-Munoz, A., Kong, J.Y., Salh, B. & Steinbrecher, U.P. Ceramide-1-phosphate blocks apoptosis through inhibition of acid sphingomyelinase in macrophages. *Journal of lipid research* **45**, 99-105 (2004).
247. Magnusson, C.D. & Haraldsson, G.G. Ether lipids. *Chemistry and physics of lipids* **164**, 315-340 (2011).
248. Filipe, M.I. The value of a study of the mucosubstances in rectal biopsies from patients with carcinoma of the rectum and lower sigmoid in the diagnosis of premalignant mucosa. *Journal of clinical pathology* **25**, 123-128 (1972).
249. Kyzer, S. & Gordon, P.H. Determination of proliferative activity in colorectal carcinoma using monoclonal antibody Ki67. *Dis Colon Rectum* **40**, 322-325 (1997).

250. Le Cao, K.A., Gonzalez, I. & Dejean, S. integrOmics: an R package to unravel relationships between two omics datasets. *Bioinformatics* **25**, 2855-2856 (2009).
251. Sing, T., Sander, O., Beerenwinkel, N. & Lengauer, T. ROCR: visualizing classifier performance in R. *Bioinformatics* **21**, 3940-3941 (2005).
252. Morad, S.A. & Cabot, M.C. Ceramide-orchestrated signalling in cancer cells. *Nature reviews. Cancer* **13**, 51-65 (2013).
253. Chaurand, P. Introducing specificity and sensitivity in imaging MS. *Bioanalysis* (2015).
254. Thomas, A., Patterson, N.H., Laveaux Charbonneau, J. & Chaurand, P. Orthogonal organic and aqueous-based washes of tissue sections to enhance protein sensitivity by MALDI imaging mass spectrometry. *J Mass Spectrom* **48**, 42-48 (2013).
255. Martin-Lorenzo, M.*, et al.* 30mum spatial resolution protein MALDI MSI: In-depth comparison of five sample preparation protocols applied to human healthy and atherosclerotic arteries. *J Proteomics* **108**, 465-468 (2014).
256. Sugiyama, E., Masaki, N., Matsushita, S. & Setou, M. Ammonium Sulfate Improves Detection of Hydrophilic Quaternary Ammonium Compounds through Decreased Ion Suppression in Matrix-Assisted Laser Desorption/Ionization Imaging Mass Spectrometry. *Anal Chem* **87**, 11176-11181 (2015).
257. Chacon, A.*, et al.* On-tissue chemical derivatization of 3-methoxysalicylamine for MALDI-imaging mass spectrometry. *J Mass Spectrom* **46**, 840-846 (2011).
258. Manier, M.L., Spraggins, J.M., Reyzer, M.L., Norris, J.L. & Caprioli, R.M. A derivatization and validation strategy for determining the spatial localization of endogenous amine metabolites in tissues using MALDI imaging mass spectrometry. *J Mass Spectrom* **49**, 665-673 (2014).
259. Toue, S.*, et al.* Microscopic imaging mass spectrometry assisted by on-tissue chemical derivatization for visualizing multiple amino acids in human colon cancer xenografts. *Proteomics* **14**, 810-819 (2014).
260. Esteve, C., Tolner, E.A., Shyti, R., van den Maagdenberg, A.M. & McDonnell, L.A. Mass spectrometry imaging of amino neurotransmitters: a comparison of derivatization methods and application in mouse brain tissue. *Metabolomics* **12**, 30 (2016).
261. Fournaise, E. & Chaurand, P. Increasing specificity in imaging mass spectrometry: high spatial fidelity transfer of proteins from tissue sections to functionalized surfaces. *Anal Bioanal Chem* **407**, 2159-2166 (2015).